Acceleration and propagation of cosmic rays in high-metallicity astrophysical environments

For the attainment of the academic degree of

Doctorate in Science

from the
Instituto de Tecnología Sabato de la
Universidad Nacional de San Martín (UNSAM)
and the
Karlsruher Institut für Technologie (KIT)

Dissertation

of

Lic. Ana Laura Müller

from Moreno

Date of the exam: 13.11.2020

Referee: Prof. Dr. Gustavo Esteban Romero

Co-Referee: Prof. Dr. Dr. h.c. Johannes Blümer

Advisor: Dr. Markus Roth

Acceleration and propagation of cosmic rays in high-metallicity astrophysical environments

Para optar por el grado académico de

Doctor en Astrofísica

del

Instituto de Tecnología Sabato de la
Universidad Nacional de San Martín (UNSAM)

Tesis

de

Lic. Ana Laura Müller

nacida en Moreno

Día de la defensa: 13.11.2020

Director: Prof. Dr. Gustavo Esteban Romero

Co-Director: Prof. Dr. Dr. h.c. Johannes Blümer

Colaborador: Dr. Markus Roth

Acceleration and propagation of cosmic rays in high-metallicity astrophysical environments

Zur Erlangung des akademischen Grades eines

Doktors der Naturwissenschaften

an der Fakultät für Physik des
Karlsruher Instituts für Technologie (KIT)

eingereichte

Dissertation

von

Lic. Ana Laura Müller

aus Moreno

Tag der mündlichen Prüfung: 13.11.2020

Referent: Prof. Dr. Gustavo Esteban Romero

Korreferent: Prof. Dr. Dr. h.c. Johannes Blümer

Betreuer: Dr. Markus Roth

Acknowledgments

First of all, I would like to express my deepest gratitude to my supervisor, Prof. Dr. Gustavo E. Romero, for his guidance, extensive knowledge, patience, encouraging support, and for trusting in me over all these years. Thank you for the commitment to my Ph.D. project and career and for giving me the freedom to make my own decisions, but always finding time to discuss and advise me.

Additionally, I am very grateful to Prof. Dr. Johannes Blümer for reviewing this thesis and especially for allowing me to participate in the Double Doctoral degree in Astrophysics program between the Karlsruhe Institute of Technology (KIT) and the Universidad Nacional de San Martín. I would also like to thank Prof. Dr. Alberto Etchegoyen and Dr. Aníbal Gattone for promoting the Argentinian side of the program. I want to extend my gratitude to all the people and funding organizations in both countries who make the DDAp program possible, especially to Marie-Christine Mundt and Prof. Dr. Frank Schröder for helping me with all the organizational situations and formalities.

My sincerest thanks to Dr. Markus Roth for his encouraging support, especially during my stay in Karlsruhe. Thank you for the patience with my German, for giving me the opportunity to learn how the experimental research on cosmic rays works, and for making me part of the working group, even when I was working on different topics. I am also very grateful to all the people at the IAP (IKP at that time) for the Kaffeepausen, cosmic coffees, movie nights, conferences, and all kinds of scientific and social moments we shared. I want to thank my several office mates there for providing a warm atmosphere, daily fun, and cookies. Particularly many thanks to Sabine Bucher for always taking care of the paperwork, even when I was in Argentina.

I also wish to thank the people at ITeDA for always making me feel welcome. Many thanks to my DDAp colleagues from both countries for a good time and for being an extraordinary group of persons always predisposed to help each other. It was a pleasure to share this experience with you.

I would also like to thank the kind people at the IAR for the enjoyable environment in such a remote place, especially the people with an own automobile who provided me a safe and comfortable ride. I am also very grateful to the GARRA members for all the scientific exchange and fruitful discussions. Moreover, thanks to the PuMA people for giving me the chance to take part in a brand new project, operating radio telescopes, and teaching me about teamwork. Special thanks to Paula Kornecki, not only for being my office mate at the IAR and collaborator in various projects but principally for being my friend.

In the same way, I want to extend my gratitude to all my friends and colleagues in La Plata for organizing not one but two farewell parties for me, one before each travel to Germany, and without whom the daily life would be more exhausting. A special mention to Florencia, Keiko, Carolina, Cecilia, Peco, and Manuela for being there for me, no matter our geographic locations. Additionally, I am very thankful to my lifelong friends from Moreno for accompanying me all these years. I would also

like to thank my Mitbewohner in Karlsruhe, especially Fabienne (and her friends), who showed me the simple and wonderful things about living in Germany.

Finally, I would like to thank Alex for proofreading this thesis, but most important for encouraging and supporting me on the bad days, particularly during the last eight months of confinement and pandemic chaos. Last but not least, I wish to acknowledge the unconditional love and support of my family, especially of my parents, Miriam and Carlos. Thank you for permanently encouraging me to do what makes me happy.

Abstract

The origin of the ultra-high energy cosmic rays (10^{18}-10^{20} eV) is one of the most persistent mysteries of the contemporary astrophysics. Although the radiation of the cosmic microwave background confines the accelerators to a distance of a few 100 Mpc, the deflections of the particle trajectories produced by magnetic fields turns the direct identification of individual sources into a very challenging task.

From the observational side, the anisotropy searches performed by the Pierre Auger Collaboration indicate some correlation with starburst galaxies and active galactic nuclei. The latter represent indeed the largest fraction of the GeV gamma-ray emitters detected by the *Fermi* satellite, revealing the existence of relativistic particles in such astrophysical sources. Gamma radiation at TeV energies from various active galaxies has also been observed, and an IceCube neutrino event has been recently suggested to be connected with a GeV flare of a blazar. In the case of starburst galaxies, the number of objects discovered at GeV energies increased from four to eight in the last eight years and more of these galaxies are expected to be detected with future generations of telescopes.

Theoretical studies have also suggested that starburst galaxies and active galactic nuclei are sources of ultra-high energy cosmic rays. Processes taking place in both astrophysical sources are capable of releasing a large amount of energy, which can be converted into relativistic particles in specific situations. Additionally, the high metallicity measured in such objects indicates that indeed intermediate-mass nuclei can be accelerated therein, in agreement with the mass-composition results of the Pierre Auger Collaboration.

In this work, we investigate the production of cosmic rays in three different scenarios: large-scale shocks driven by starburst superwinds, bow shocks around clumps embedded in starburst superwinds, and shocks induced by collisions of broad-line region clouds against accretion disks in active galactic nuclei. All the analyses have been performed through semi-analytical simulations, whose fiducial parameters were chosen according to the compiled information from published bibliography. Studies on specific sources have been conducted applying rigorously the constraints imposed by the multi-wavelength electromagnetic information of the objects. In all these astrophysical situations, we evaluated the feasibility of accelerating particles, calculated the energy distributions of cosmic rays, determined their maximum energies, and computed the foreseen spectral energy distributions of the non-thermal radiation.

The results obtained in this thesis evince the difficulty of generating particles up to ultra-high energies under common conditions and help to constrain the characteristics of the cosmic ray accelerators of such energies. Moreover, we show the importance of disentangling the ambiguous properties of objects simultaneously classified as starbursts and active galactic nuclei, in order to clarify the origin of the cosmic rays at the highest energies. All in all, the theoretical models developed in this work might contribute to the interpretation of the observational information collec-

ted by the next generation of observatories at various wavelengths and astroparticle experiments.

Resumen

El origen de los rayos cósmicos ultra energéticos (10^{18}-10^{20} eV) es uno de los misterios más persistentes de la astrofísica contemporánea. Aunque la radiación del fondo cósmico de microondas permite confinar las posibles fuentes a una distancia de algunos cientos de Mpc, las deflexiones en las trayectorias de las partículas causadas por los campos magnéticos transforman la identificación directa de fuentes individuales en una tarea compleja.

Desde el lado observacional, las búsquedas de anisotropías llevadas a cabo por la Colaboración Pierre Auger indican cierta correlación con galaxias con brotes de formación estelar y núcleos galácticos activos. En efecto, estos últimos representan la mayor fracción de emisores gamma a energías del GeV detectados por el satélite *Fermi*, revelando la existencia de partículas relativistas en tales fuentes astrofísicas. Radiación gamma a energías de TeV también ha sido observada en algunas galaxias activas, así como también una posible conexión entre un evento observado por IceCube y una fulguración gamma de un blazar. En el caso de las galaxias con brotes de formación estelar, el número de estos objetos descubiertos a energías del GeV se ha incrementado de cuatro a ocho en los últimos ocho años y se espera que siga en aumento con las próximas generaciones de telescopios.

Estudios teóricos también han propuesto que las galaxias con brotes de formación estelar y los núcleos galácticos activos son fuentes de rayos cósmicos ultra energéticos. Ciertos procesos ocurriendo en ambas fuentes astrofísicas son capaces de liberar una gran cantidad de energía que, bajo circunstancias específicas, puede ser convertida en partículas relativistas. Asimismo, la alta metalicidad medida en estas fuentes indica que núcleos con masas intermedias como los observados por el Observatorio Pierre Auger pueden acelerarse allí.

En este trabajo investigamos la producción de rayos cósmicos en tres escenarios diferentes: ondas de choques a gran escala generadas por los supervientos de las galaxias con brotes de formación estelar, choques de proa alrededor de inhomogeneidades presentes dentro de los mismos supervientos, y ondas de choque inducidas por las colisiones de nubes de la región de líneas anchas contra los discos de acreción en núcleos galácticos activos. Todos los análisis han sido llevados a cabo mediante simulationes semi-analíticas, cuyos parámetros fiduciales fueron elegidos acorde a la información recopilada de bibliografía publicada. Estudios de fuentes específicas han sido realizados teniendo en cuenta rigurosamente las restricciones impuestas por la información electromagnética de los objetos en múltiples longitudes de onda. En todas las situaciones astrofísicas hemos evaluamos la factibilidad de acelerar partículas, calculado las distribuciones en energía de rayos cósmicos, determinado sus energías máximas, y construido las distribuciones espectrales de energía predichas para la radiación no térmica.

Los resultados obtenidos en esta tesis evidencian la dificultad de generar partículas ultra energéticas en condiciones normales y contribuyen a delimitar las características de los aceleradores de rayos cósmicos de tales energías. Además,

muestran la importancia de desentrañar las propiedades ambiguas de los objetos simultáneamente clasificados como galaxias con brotes de formación estelar y núcleos galácticos activos con el fin de clarificar el origen de los rayos cósmicos más energéticos. En términos generales, los modelos teóricos desarrollados en este trabajo pueden contribuir a la intrepretación de la información observacional recolectada por la siguiente generación de observatorios de diferentes longitudes de onda y astropartículas.

Zusammenfassung

Der Ursprung der ultra-hochenergetischen kosmischen Strahlung (10^{18}-10^{20} eV) ist eines der größten Mysterien in der gegenwärtigen Astrophysik. Obwohl die Strahlung des kosmischen Mikrowellenhintergrunds die Teilchenbeschleuniger auf einen Abstand zu unserem Sonnensystem von wenigen 100 Mpc begrenzt, ist die direkte Identifizierung dieser kosmischen Quellen durch die von Magnetfeldern hervorgerufene Ablenkungen der Teilchenbahnen eine sehr anspruchsvolle Aufgabe.

Betrachtet man die aktuellen Beobachtungen der komischen Strahlung, deuten die von der Pierre-Auger-Kollaboration durchgeführten Anisotropiesuchen auf eine Korrelation der Ankunftsrichtung der Teilchen mit Starburstgalaxien und aktiven Galaxienkernen hin. Letztere stellen dabei den größten Anteil der vom *Fermi*-Satelliten entdeckten GeV-Gammastrahlenemitter dar. Damit besteht eine sehr hohe Wahrscheinlichkeit, dass relativistische Teilchen in diesen astrophysikalischen Quellen existieren. Zudem wurde die Emission von Gammastrahlung mit einer Energie im Bereich von TeV von verschiedenen aktiven Galaxien beobachtet, und des Weiteren kürzlich ein IceCube-Neutrinoereignis vorgeschlagen, das mit einem GeV-Flare eines Blazars in Verbindung gebracht werden könnte. Im Fall der Starburstgalaxien erhöhte sich die Zahl der bei GeV-Energien entdeckten Objekte in den letzten acht Jahren von vier auf acht und es ist zu erwarten, dass mit zukünftigen Generationen von Teleskopen zudem weitere dieser Galaxien entdeckt werden können.

Starburstgalaxien und aktive Galaxienkerne wurden zudem auch als Kandidaten für Quellen der ultra-hochenergetische kosmische Strahlung von theoretischen Arbeiten vorgeschlagen. Prozesse, die in beiden astrophysikalischen Quellen ablaufen, sind in der Lage, eine große Menge an Energie freizusetzen, die unter bestimmten Bedingungen in relativistische Teilchen umgewandelt werden kann. Zusätzlich weist die gemessene hohe Metallizität dieser Objekte darauf hin, dass Teilchenkerne mittlerer Masse in diesen Quellen beschleunigt werden können. Diese Kerne mit einer Masse schwerer als ein Proton, aber leichter als ein Eisenkern wurden von der Pierre-Auger-Kollaboration beobachtet.

In dieser Arbeit untersuchen wir die Erzeugung von kosmischer Strahlung in drei verschiedenen Szenarien: in grossräumige Stoßwellen, die durch Starburstsuperwinde angetrieben werden, in Bugstoßwellen um Zusammenballungen von kaltem Gas, die in Starburstsuperwinden eingebettet sind, und in Stoßwellen, die durch Kollisionen von Plasmawolken der broad-line Region mit Akkretionsscheiben von aktiven Galaxienkernen erzeugt werden. Alle Analysen wurden mittels semianalytischer Simulationen durchgeführt, deren Bezugsparameter entsprechend den gesammelten Informationen aus Veröffentlichungen ausgewählt wurden. Auch die hier durchgeführten Studien einzelner Quellen unterliegen Einschränkungen, die auf den elektromagnetischen Multiwellenlängen-Informationen der jeweiligen Objekte basieren. In all diesen astrophysikalischen Gegebenheiten evaluierten wir die Durchführbarkeit der Teilchenbeschleunigung, berechneten die Energieverteilungen der kosmischen Strahlung, bestimmten ihre maximale Energie und berechneten die erwarteten spektralen Energieverteilungen der nichtthermischen Strahlung.

Die in dieser Arbeit erzielten Ergebnisse zeigen die Komplexität der Erzeugung von Teilchen mit ultrahohen Energien unter gewöhnlichen Bedingungen auf, und helfen dabei die Eigenschaften der Beschleuniger der kosmischen Teilchen einzuschränken. Darüber hinaus zeigen wir die Wichtigkeit, die mehrdeutigen Eigenschaften einzelner Objekte, die gleichzeitig als Starbursts und aktive Galaxienkernen klassifiziert werden können, zu entschlüsseln, um den Ursprung der kosmischen Strahlung bei höchsten Energien zu bestimmen. Alles in allem können die in dieser Arbeit entwickelten theoretischen Modelle zur Interpretation der Beobachtungen beitragen, die die nächsten Generationen von Observatorien für verschiedene Wellenlängen und Astroteilchen liefern werden.

Acronyms

This is a list of acronyms used within this work sorted alphabetically according to the short version.

AGN	active galactic nucleus
ALMA	Atacama Large Millimeter/submillimeter Array
Auger	the Pierre Auger Observatory
BH	black hole
BLR	broad-line region
CMB	Cosmic Microwave Background
CR	cosmic ray
CTA	Cherenkov Telescope Array
DSA	diffusive shock acceleration
FIR	far-infrared
GRB	gamma-ray burst
H.E.S.S.	High Energy Stereoscopic System
IC	inverse Compton
IR	infrared
ISM	interstellar medium
KH	Kelvin-Helmholtz
LHC	Large Hadron Collider
NLR	narrow-line region
RT	Rayleigh-Taylor
SBG	starburst galaxy
SDA	stochastic diffusive acceleration
SED	spectral energy distribution
SFR	star formation rate
SN	supernova
SNR	supernova remnant
SSA	synchrotron self-absorption
TA	the Telescope Array Project
UHECR	ultra-high energy cosmic ray
UV	ultraviolet
VLBA	Very Long Baseline Array

Contents

1

Introduction

Since Viktor Hess demonstrated the existence of "high penetrating radiation coming from above", the scientific community has been triying to understand how and where it is produced (Hess 1912). After more than 100 years of experimental and theoretical work, several questions regarding cosmic rays have been answered. For instance, we have learned that the spectrum of particles with energies below ~30 GeV is modulated by the solar activity, whereas most of the particles with energies ranging from 30 GeV to 10^5–10^6 GeV are likely accelerated by Galactic supernova remnants (Gaisser et al. 2016). Nevertheless, the region of the transition from Galactic to extragalactic, the interpretation of the features of the comic ray spectrum, as well as the origin and characteristics of the ultra high-energy particles are still a matter of debate.

The Pierre Auger Collaboration has reported that the composition of cosmic rays turns into heavier for energies exceeding $10^{18.5}$ eV (Aab et al. 2014; The Pierre Auger Collaboration et al. 2017, 2019). Their reconstructed nuclei are typically consistent with intermediate masses, i.e., oxygen, nitrogen, etcetera. This result differs from the light composition deduced by the Telescope Array Project, but both agrees within the errors (Abbasi et al. 2016). Furthermore, the extragalactic origin of the cosmic ray with energies above 8 EeV has been confirmed (Pierre Auger Collaboration et al. 2017) and a 4.5σ correlation has been established between the arrival directions of particles with $E > 38$ EeV and the positions of starburst galaxies. A correlation with active galactic nuclei with a slightly smaller significance has been also informed (Aab et al. 2017, 2018; The Pierre Auger Collaboration et al. 2019). Particularly, excess at the position of the nearest radio galaxy Centaurus A has been detected with a 3.9σ significance (The Pierre Auger Collaboration et al. 2019).

On the other hand, the improvement of the high-energy telescopes has provided a more accurate and detailed characterization of astrophysical sources. After 10 years of collecting data, the *Fermi* satellite has detected more than 3000 gamma-ray sources, of which more than 2000 are associated with some type of active galactic nucleus[1], and 8 are starburst galaxies (Ballet et al. 2020). Two of the starbursts, M82 and NGC 253, have also been observed in the TeV range using VERITAS[2] and H.E.S.S.[3], respectively (Acero et al. 2009; Abdo et al. 2010). The X-ray studies have also gained time and spatial resolution with satellites such as *Swift*, *XMM-Newton*, and *Chandra*. At lower energies, the development of new and better telescopes has been very useful to understand the non-thermal Universe, especially at radio frequencies where

[1]Most of them are blazars.
[2]Very Energetic Radiation Imaging Telescope Array System.
[3]High Energy Stereoscopic System

synchrotron radiation shows up. The high-quality electromagnetic observatories are currently complemented with the latest cosmic ray, neutrino and gravitational wave detectors.

Coincidences between some or all the different types of radiations have been predicted a long time ago. The link between low energy cosmic rays and solar flares has been observed since 1940, whereas in 1987 optical photons but also neutrinos from a supernova were simultaneously detected (Hirata et al. 1987; Bionta et al. 1987). In 2017, the related detection of gravitational waves and a gamma-ray burst boosted the multi-messenger astronomy, confirming that the understanding of some astrophysical situations is only possible through collective efforts (Abbott et al. 2017). A short time after this kilonova event, the possible association between high-energy neutrino events and blazars has also been established. Recently, the relation between an IceCube detection and a tidal disruption event has been reported as well (IceCube Collaboration et al. 2018a,b; Stein et al. 2020).

Although the big advances, a simultaneous detection of all the messengers have not occurred yet. In particular, despite the evidence pointing to starburst galaxies and active galactic nuclei as ultra-high energy cosmic ray sources, there is no complete successful theoretical explanation for their production. In this thesis, we aim to study scenarios where particles can be accelerated in starburst galaxies or active galactic nuclei. The models presented are applied to specific objects taking into account the observational information available in the bibliography. In the next chapter, we review the current astrophysical context, describing the relevant experiments and discoveries. Chapter 3 summarizes all the physical concepts and formulas necessary for our analyses. Chapter 4, Chapter 5, and Chapter 6 address three different scenarios where relativistic particles can be produced, the first two in starburst galaxies and the last one in active galactic nuclei. In Chapter 7 we discuss the results obtained and their implication in the search of cosmic ray sources. Finally, Chapter 8 presents a summary, our conclusions, and future perspectives.

2

Astrophysical context

Defining when the story of the high-energy astrophysics has exactly begun is very difficult. The first record of a supernova explosion dates back to 185 AD, but at that time the information was limited to what the eyes could see. Many centuries more were necessary to discover phenomenons and processes that allowed the scientists to explain that "guest star" documented by the Chinese astronomers. Nowadays, the advances in high-energy physics as well as the improvements in the detection technologies make our era a prosperous one for investigating and trying to understand the high-energy Universe in depth. This chapter introduces the astrophysical motivations for the work presented in this thesis.

2.1 Radiation

2.1.1 Cosmic rays

In the early 20$^{\text{th}}$ century, the scientists realized that the atmosphere is not neutral, but ionized to some degree. At that time, it was known that the emission from radioactive elements can ionize atoms and consequently, they started to think about radioactive elements contained in the Earth's crust and causing the atmospheric condition. Nevertheless, the carried-out experiments exhibited unexpected results. In 1912, Viktor Hess recorded the atmospheric electric charge at different altitudes with the help of hot air balloons. He found that the ionization rate increases with the distance to the Earth's surface and wrote that this can only be caused by deep penetrating radiation coming from above (Hess 1912). Indeed, the phenomenon pointed out by Hess is the consequence of charged relativistic particles entering the atmosphere. These particles, namely cosmic rays (CRs), are mostly protons or nuclei (98 %); only the remnant 2 % are electrons. Main contribution is approximately formed by 90 % protons, 9 % alpha particles, and 1 % heavier nuclei (Longair 2011).

The CR flux is globally well described with power-law functions. At energies below 10 GeV, the flux of particles is modulated by the solar activity. Above this energy, and up to 1 PeV, the differential spectrum follows a power-law with an index of −2.7. Above 1 PeV, the spectrum becomes softer having a slope of −3.1. The index changes again at 5 EeV, getting a value of −2.6. Finally, the flux seems to be suppressed at energies ~10^{20} eV. The transitions at 1 PeV and 5 EeV are denominated as *knee* and *ankle*, respectively (Gaisser et al. 2016). Two extra slope changes have been reported at 0.1 EeV, namely *second knee*, and at 13 EeV (Aab et al. 2020a,b). The observational

evidence collected by the KASCADE[1] experiment suggests that each knee is related to the suppression of the light or the heavy CR component (Antoni et al. 2005; Apel et al. 2011). The ankle is thought to be caused by the transition between the Galactic and extragalactic contributions. However, there is some discrepancy about how exactly this feature is formed. The mixed composition model suggests that the ankle is simply the smooth transition between Galactic and extragalactic CRs (Allard 2012). Alternately, the dip model places the transition at energies of about 1 PeV. Consequently, if the CR extragalactic flux is proton dominated, the ankle can be understood as the region where particles accumulate after propagating and interacting with the Cosmic Microwave Background (CMB) photons (Berezinsky 2007). A third possible explanation was recently given by Farrar et al. (2015). In their proposal, the ankle is the result of the photodisintegration suffered by the nuclei in the source.

The origin of the CR falling-off at $5{\times}10^{19}$ eV remains also unclear. On one hand, it can be understood in terms of the propagation effects. As mentioned before, the protons interact with the CMB photons along their trajectories to the Earth. In each collision, the particle loses ~20 % of their energy through the following channels

$$\begin{aligned} \gamma_{\mathrm{CMB}} + p \rightarrow & \Delta^+ \rightarrow p + \pi^0, \\ \gamma_{\mathrm{CMB}} + p \rightarrow & \Delta^+ \rightarrow n + \pi^+. \end{aligned} \tag{2.1}$$

This effect is known as the GZK effect, named after Greisen-Zatsepin-Kuz'min (Greisen 1966; Zatsepin & Kuz'min 1966). If the particles are nuclei instead of protons, a similar suppression effect occurs as a consequence of the photodisintegration (Stecker & Salamon 1999). On the other hand, the drop could indicate the acceleration limit of the ultra-high energy cosmic ray (UHECR) sources (see e.g., Alves Batista et al. 2019). Figure 2.1 shows the measured CR spectrum.

Independently whether the GZK is or is not the principal cause of the drop at the highest energies, it yields a maximum distance at which the accelerators can be placed. Sources of protons with energies of about 10^{19} eV should be closer than 1 Gpc, whereas for protons with energies beyond $5{\times}10^{19}$ eV the distance limit reduces to ~100 Mpc (Alves Batista et al. 2019). Nevertheless, the trajectories of CRs are affected and modified by the magnetic fields, which makes the tracking of the particles back to the source a very difficult task. Out of the solar dominated region, the CR flux is observed to be highly isotropic, with anisotropies only expected for the highest energies. Light particles with energies above 10^{19} eV are predicted not to be strongly deflected by the Galactic and extragalactic magnetic fields, and therefore, correlations with their sources could be established. Since the goal of this work is to study possible sources of UHECRs, we focus hereafter in this section only on the results at such energies (see e.g., Gabici et al. 2019, for a review on Galactic CRs).

In the present day, the most prominent observatories for UHECRs are the Pierre Auger Observatory (Auger), located in the southern hemisphere (Argentina), and the Telescope Array Project (TA), placed in the north (US). The entrance of a UHECR in the Earth's atmosphere initiates a cascade of secondary particles (see Fig. 2.2), whose detection allows the reconstruction of the primary CR. The arrival rate of particles at the highest energies is only 1 particle $\mathrm{km}^{-2}\,\mathrm{century}^{-1}$, and consequently, their studies

[1] Karlsruhe Shower Core and Array Detector.

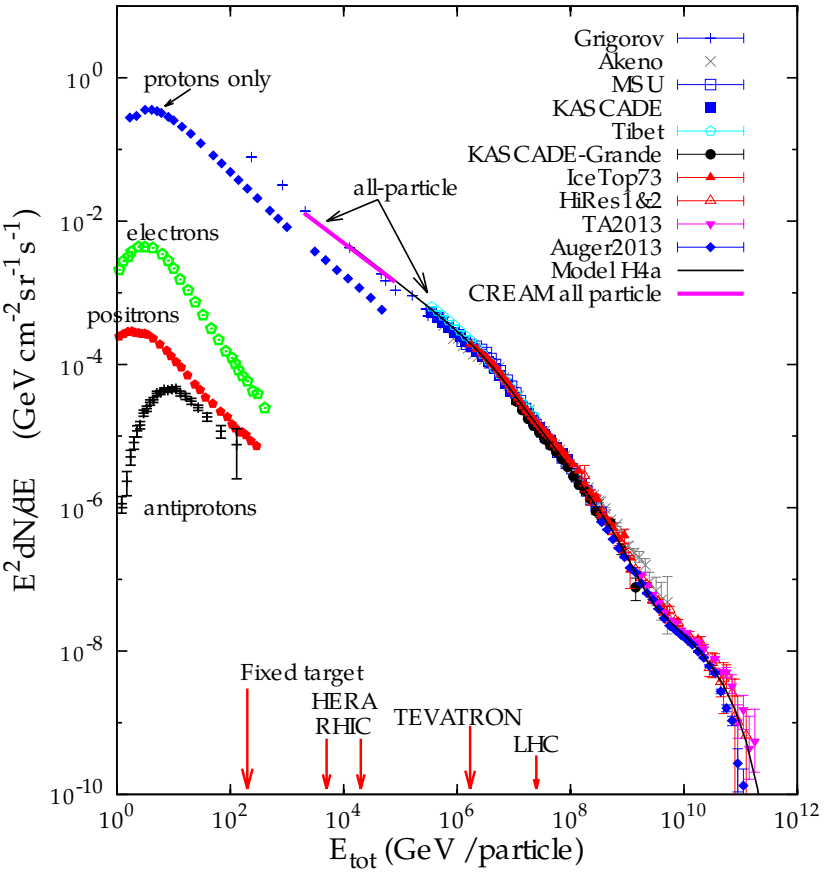

Figure 2.1: Cosmic ray spectrum. Taken from Gaisser (2017).

require detectors covering large areas. The TA Project is composed of scintillator surface detectors and fluorescence telescopes arranged in an area of 700 km^2 (Abu-Zayyad et al. 2012). The Auger Observatory is also hybrid, currently[2] consisting of a Surface Detector with different components[3], as well as fluorescence telescopes and radio antennas. The total area of Auger is of about 3000 km^2, converting it into the largest UHECR observatory in the world (The Pierre Auger Collaboration 2015).

From the beginning, a tight relation between CR and particle physics was established. The information provided by UHECR is still being extremely relevant because none of the built artificial accelerators reaches the measured energies of the natural ultra-high energy particles. From the astrophysical point of view, the three most important topics that the UHECR studies address are the measurement of the flux, the composition of the particles, and the anisotropy studies. The analyses carried out by Auger indicate that the composition of CRs becomes lighter as the energy approaches to the ankle ($10^{18.3}$ eV). Beyond this energy, the composition turns into heavier, with the proton composition replaced by helium and nitrogen (The Pierre Auger Collaboration et al. 2019). On the other hand, the data collected by TA between $10^{18.2}$ eV and 10^{19} eV can be interpreted as a pure proton dominated composition, but also consistent with the composition deduced by Auger (see De Souza et al. 2017, for more details). Above $10^{19.4}$ eV, there is evidence of an iron contribution, but the

[2]The observatory is undergoing a major upgrade.
[3]Water Cherenkov detectors, surface and underground scintillator detectors.

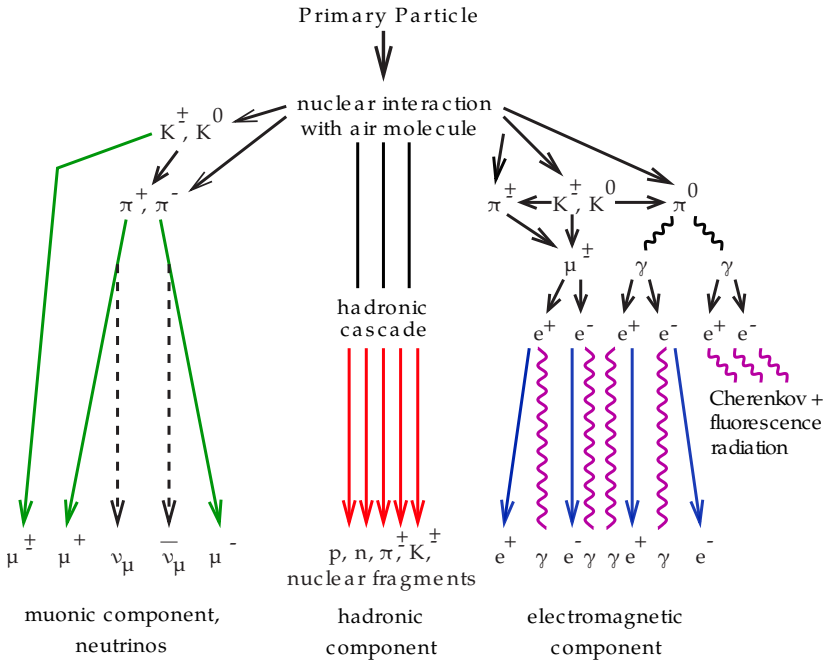

Figure 2.2: Scheme of an extensive air shower. Taken from Haungs et al. (2003) and modified.

insufficient data and the uncertainties in the hadronic interaction models make the results not conclusive (Alves Batista et al. 2019). The dominant light component around 10^{18} eV is expected to have an extragalactic origin, since Galactic particles should produce a large-scale anisotropy at 10^{18} eV towards the Galactic disk, which contradicts the outcomes of TA and Auger.

Auger has reported a clear detection of a dipole structure for the arrival direction of particles with energies above 8 EeV. The dipole points to ~125° away from the Galactic center, indicating that the origin of the anisotropy is extragalactic. The amplitude of the dipole of ~6.5 % suggests it is a consequence of anisotropic distributed sources within ~100 Mpc (Pierre Auger Collaboration et al. 2017; The Pierre Auger Collaboration et al. 2019). Anisotropy studies at smaller scales have been performed as well. The results of Auger show a 5.6 σ local excess for energies above 54 EeV in the direction (α, δ)=(202°, −45°) in a 27° radius window, but with a post-trial p-value of 2.5% (The Pierre Auger Collaboration et al. 2019). The TA search displays excess of particles with energies above 57 EeV in a window of 25° radius with a penalized significance of 2.9 σ in the direction (α, δ)=(144.3°, 40.3°) (Kawata et al. 2019). Inside these regions, nearby sources of different nature are located such as starburst galaxies (SBGs), blazars, radio galaxies, regular star-forming galaxies, and galaxy clusters. Consequently, correlation analyses using different catalogs of sources have been presented by both collaborations and independent groups. Nevertheless, none of the works has shown any statistically significant anisotropy yet ($> 5\,\sigma$) (Alves Batista et al. 2019). The most promising results are those reported by Auger. A 4.5 σ correlation with SBGs has been established, along with a 3.7 σ with active galactic nuclei (AGNs). At the same time, a correlation with the radio galaxy Centaurus A, which is located inside the Auger hot spot, has a significance of 3.9 σ for energies above 37 EeV (The Pierre Auger Collaboration et al. 2019). These correlation searches are also based on

the connection between the CRs and the electromagnetic emission of the sources, especially at high energies. Therefore, we continue with a brief overview of gamma radiation in the next section.

2.1.2 Gamma rays

Relativistic particles can lose energy by producing radiation over the whole electromagnetic spectrum, which provides valuable information about all the processes taking place in the source, including the acceleration. Although at low frequencies the emission requires typically a more detailed examination in order of determining whether it is produced by relativistic or thermal particles, photons with energies above 100 keV are not expected to be thermal. Relativistic electrons commonly produce gamma emission by relativistic Bremsstrahlung and inverse Compton scattering, whereas relativistic protons can generate neutral pions which decay in gamma photons (see Section 3.4). Radiation is not only produced by CRs at the source, but also during their propagation in the interstellar medium. Consequently, the gamma emission results in an unambiguous tracer of CRs.

The detection of gamma rays is done with different techniques depending on their energy. Below 10^{11} eV, the radiation is collected by satellites. Currently, the most sensitive gamma-space telescope is the *Fermi* satellite (Atwood et al. 2009). Its LAT instrument working in the energy range between 20 MeV and 300 GeV has detected more than 3000 sources since it was launched in 2008. Unlike typical space telescopes, *Fermi* operates primarily in all-sky survey mode. Fig. 2.3 displays the gamma-ray sky observed by *Fermi* (Abdollahi et al. 2020). Although the many sources located towards the Galactic plane, 90 % of the sources detected by *Fermi* are extragalactic, most of them are AGNs. Additionally, the sample includes 8 SBGs, and 5 regular star-forming galaxies (Ballet et al. 2020). Ajello et al. (2020) has also reported gamma emission from M33, but this galaxy has not been confirmed by the second release of the Fermi Fourth Source Catalog (Ballet et al. 2020). Therefore, other relevant information provided by *Fermi* is the measurement of the extragalactic gamma-ray background, which is composed of the isotropic diffuse gamma-ray background, but also the contributions of the extragalactic resolved sources. The detected flux is presented in Fig. 2.4. The spectrum observed by *Fermi* between 100 MeV and 820 GeV is well described by a power-law, with a spectral index ~2.3 and a cut-off at ~300 GeV (Ackermann et al. 2015). Since the hadronic processes producing gamma emission create also neutrinos, the observed gamma flux is usually compared with the neutrino flux to characterize better the sources (see e.g., Ahlers & Halzen 2018).

At higher energies, the detection technique for gamma rays is quite similar to the employed with UHECRs. Photons with energies beyond 10^{11} eV are absorbed in the Earth's atmosphere and initiate cascades of particles, but only with an electromagnetic component. The secondary electrons produce Cherenkov radiation, which is detected by arrays of telescopes such as High Energy Stereoscopic System (H.E.S.S.) (De Naurois 2019), MAGIC[4] (Aleksić et al. 2016), or VERITAS[5] (Quinn 2019), and allows to reconstructs the gamma rays entering the atmosphere. Photons with energies above 10^{14} eV develop cascades whose particles reach the Earth's surface being enough

[4]Major Atmospheric Gamma Imaging Cherenkov Telescopes.
[5]Very Energetic Radiation Imaging Telescope Array System.

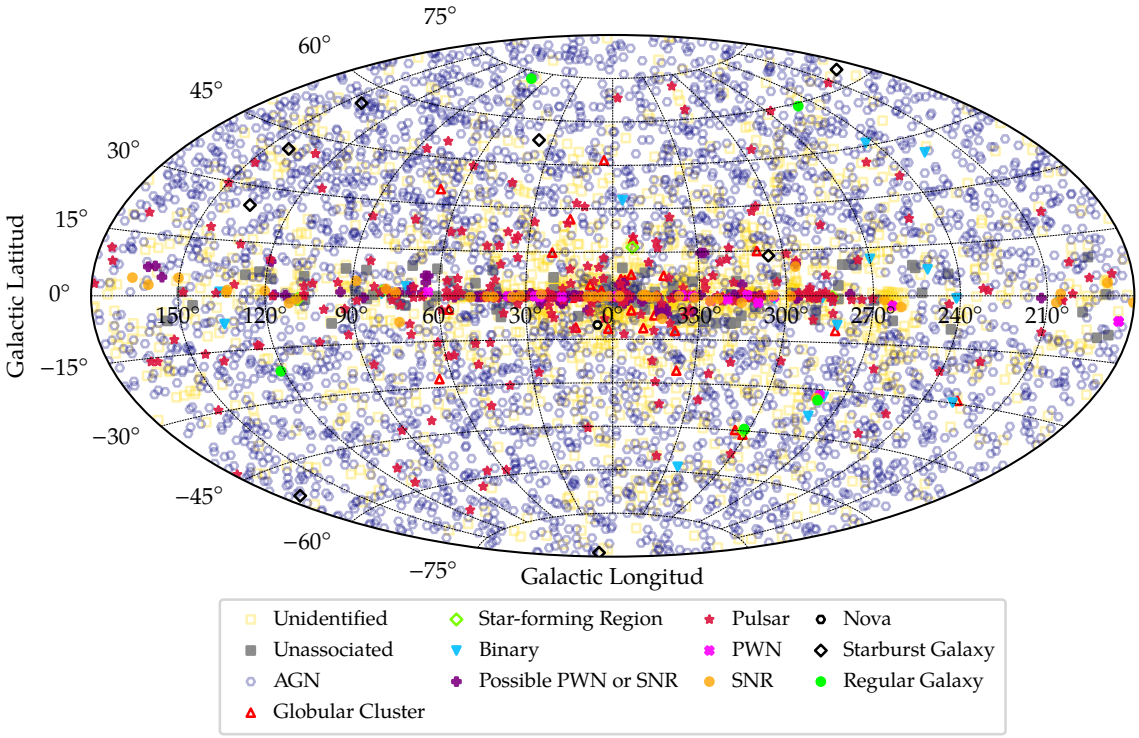

Figure 2.3: All *Fermi* sky-map in Galactic coordinates. Data from the *Fermi* LAT Fourth Source Catalog Data Release 2 (Ballet et al. 2020).

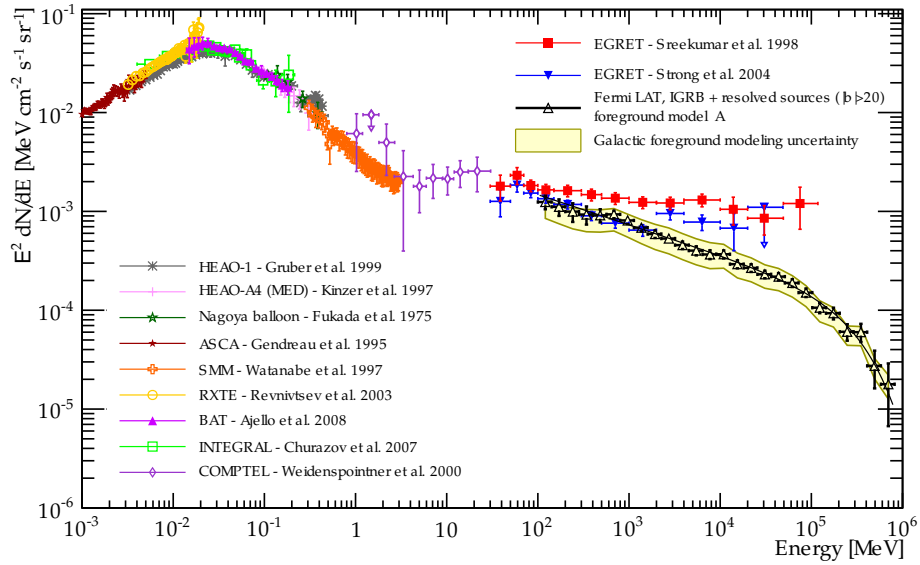

Figure 2.4: Total extragalactic X and gamma-ray background detected by *Fermi* and other experiments. Taken from Ackermann et al. (2015).

energetic to produce Cherenkov radiation in water tanks. The HAWC observatory[6] detects and reconstruct the gamma emission employing this procedure (Marandon et al. 2019). As in the case of the UHECRs, the sources of detectable very-high and ultra-high energy gamma rays can be located within a maximum distance, given

[6]High-Altitude Water Cherenkov Gamma-Ray Observatory.

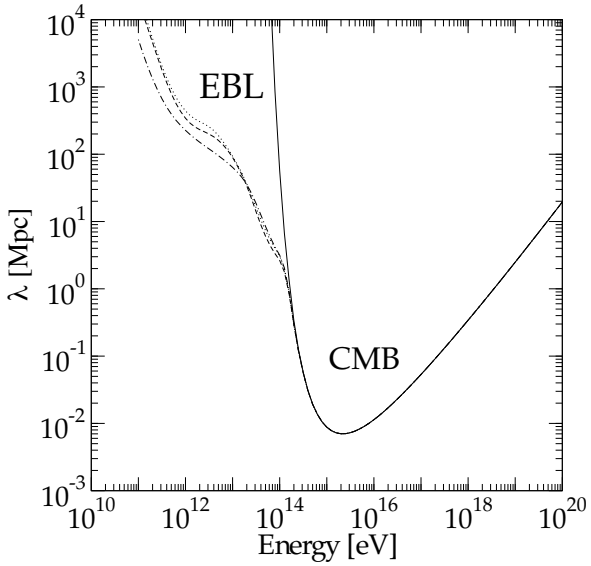

Figure 2.5: Mean free path of very high-energy photons propagating through the interstellar medium at the present time (CMB well represented by a black body with a temperature of 2.7 K). EBL indicates the interaction with the extragalactic background light, each line pattern represents a different model for this radiation field (see the original reference for more details). Taken from Venters (2010).

that the gamma photon can be absorbed as a consequence of the interaction with radiations fields such as the CMB or the extragalactic background light, as shown in Fig. 2.5 (see Section 3.4.3 for more details about absorption).

The most relevant forthcoming experiments are perhaps the space telescopes such as AMEGO (McEnery et al. 2019) or eASTROGAM (de Angelis et al. 2018), which will allow exploring the MeV energy band more precisely, and the ground-based Cherenkov Telescope Array (CTA) observatory, which will cover the whole sky, increasing the sensitivity of its predecessors and extending the observational energy range up to 300 TeV (CTA Consortium & Ong 2019).

2.1.3 Neutrinos

Neutrinos are expected to be produced in many astrophysical situations, such as in the nuclei of the stars as a consequence of nuclear fusion. They are also created by the interaction of CRs with matter or radiation inside the sources, during propagation, and in the Earth's atmosphere.

The main problem around the detection of neutrinos is that these particles are only weakly interacting, and therefore, targets of large volumes are needed to detect them. Some experiments as Kamiokande or IBM employed large artificial underground reservoirs of pure water as detectors, which were capable of detecting, e.g., the ~10 MeV burst of neutrinos produced by the supernova SN1987A (Hirata et al. 1987; Bionta et al. 1987). Nevertheless, the motivation of observing neutrinos with higher energies moves the focus to places where the telescopes could be build taking advantage of the natural environment. Telescopes such as Baikal or ANTARES were built in the lake Baikal and in the Mediterranean Sea, respectively (see e.g., Simkovic 2019; Kouchner 2019, for the most recent status and results). In the early

1990s, Francis Halzen and other scientists suggested using ice as a target for neutrino detection. That is why the Antarctic Muon and Neutrino Detector Array (AMANDA) was deployed at the South Pole between 1993 and 1994 (Karle 2013). In 2005 the construction of the IceCube Neutrino Observatory started, and AMANDA became a sub-array of it until 2009 when it was turned off. In the present, IceCube is the largest neutrino telescope covering a cubic kilometer of ice. The detector consist of vertical strings with optical sensors installed inside the Antarctica ice in a depth between 1450 m and 2450 m (see Halzen & Klein 2010, for more technical details).

One way to understand why large neutrino telescopes are necessary requires to look at TeV gamma-ray sources. If these photons are created by the decay of neutral pions, a similar flux of neutrinos is expected from the decay of the charged pions (see Section 3.4 and Fig. B.1). The flux of bright TeV sources is typically less than the observed from the Crab Nebula $dN_\nu/d\log_{10}(E) \sim 7\times10^{-11}$ cm^{-2} s^{-1} at 1 TeV. The cross section of the neutrinos at this energy is $\sim10^{-35}$ cm^2, whereas the number of nucleons in one kilometer square of water is 6×10^{38}. Consequently, the estimated rate of neutrino interactions is ~10 per year per decade of energy (Gaisser et al. 2016). A more general argument was given by Waxman & Bahcall (1999), whose result shows essentially that the upper limit of the neutrino flux is close to the CR flux, because the former are a result of the interactions of the latter.

The identification of astrophysical neutrino sources can provide significant information about the origin of the CRs, since neutrinos do not suffer the strong effects of the magnetic fields or absorption. The cosmic neutrino flux reported by IceCube can be described by a broken power-law, with an spectral index of about –3.7 for energies between 30 TeV and 100 TeV and –2.3 at higher energies. This issue suggests that either the spectrum of cosmic neutrinos has a second component, or the CR at the accelerators cannot be described by a single power-law (see Fig. 2.6). The lack of strong anisotropies in the measured flux suggests a mainly extragalactic contribution (Ahlers & Halzen 2018). Cosmogenic neutrinos are also expected to be produced by proton UHECRs interacting with the CMB (see Section 2.1.1). However, these neutrinos have been not detected implying that the flux should be smaller than expected and supporting the evidence of a heavier composition for the CRs at the highest energies (Aartsen et al. 2018).

After 10 yr of collecting data, IceCube reported an excess of neutrinos above 1 TeV coincident with the position of the galaxy NGC 1068 with a post-trial significance of 2.9 σ (Aartsen et al. 2020). In 2018, a coincidence of 3 σ significance between a high-energy neutrino event with a flare in the gamma-ray blazar TXS 0506+056 was also reported (IceCube Collaboration et al. 2018a). The analysis of neutrino events in the same direction of TXS 0506+056 but over the 9.5 yr of IceCube data pointed out the existence of a neutrino excess between 2014 and 2015 of 3.5 σ significance, which suggests that blazars are potentially identifiable neutrino sources (IceCube Collaboration et al. 2018b). Recently, a new coincidence has been reported between an IceCube neutrino event and a radio-emitting tidal disruption event, but also without statistical significance (Stein et al. 2020).

The observed similarities between the CR, gamma-ray, and neutrino fluxes suggest a common origin for all these particles. Figure 2.7 displays the three spectra together. The dashed and dotted lines are the predictions of neutrinos according to the flux of the other particles. The particular case of the prediction indicated as "B" in the figure

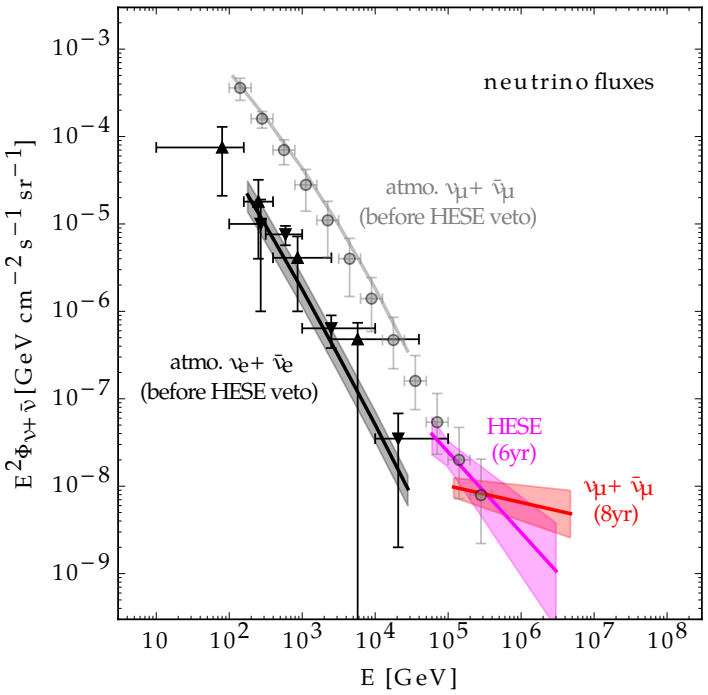

Figure 2.6: Neutrino flux reported by IceCube. The low-energy component corresponds to the atmospheric neutrinos, whereas the high-energy components are the cosmic neutrinos. The magenta component represents the flux of high-energy events started inside the detector (HESE), whereas the red are the events of up-going muon neutrinos. Taken from Ahlers & Halzen (2018).

assumes that CRs with energies below the ankle remain trapped in the sources, and their energy is completely converted into gamma rays and neutrinos; this condition is the so-called calorimetric limit. As can be noted, the neutrino flux explained by this limit is saturated, and therefore, the existence of calorimetric sources of CRs is expected. Nevertheless, the connection with UHECRs requires that particles above the ankle can escape, producing a change in the neutrino flux at 1 PeV. Consequently, studies of the neutrino fluxes above this energy can provide valuable evidence of the environment and conditions where CRs are accelerated (see Ahlers & Halzen 2018, for a more detailed discussion).

2.1.4 Gravitational waves

In this section, we present a short overview of gravitational waves. This is included just for completeness because none of the scenarios studied in this thesis are expected to produce detectable gravitational waves.

Gravitational waves are perturbations in the curvature of the spacetime that propagate at the speed of light. They are predicted by the general theory of relativity, and the first proof of their existence was given by the binary system of pulsars B1913+16, most commonly known as the Hulse-Taylor pulsar. The observations of these pulsars conducted over years showed that the evolution of the orbit parameters of the binary system displays some energy discrepancy in classical terms, but which is completely explainable by general relativity if gravitational energy is radiated (see Weisberg & Taylor 2005, for more details).

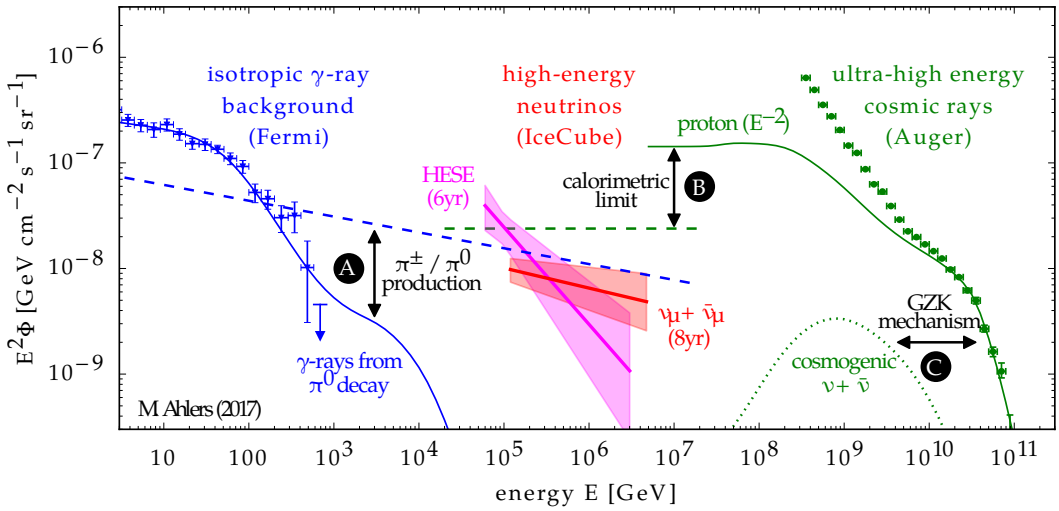

Figure 2.7: Isotropic gamma-ray background, cosmic neutrinos, and CRs spectra. The dashed lines correspond to the neutrino predictions sharing a common origin with the other particles. Taken from Ahlers & Halzen (2018).

The direct detection of gravitational waves is a very challenging task because of their small amplitudes. The technique used in all the current experiments (LIGO, Virgo, GEO 600, and KAGRA) consists of an interferometer with two arms in "L" shape. When a gravitational wave passes by, the length of the arms is modified. The final result is a pattern of interference when the light of both arms is combined, which is compared with templates corresponding to different types of expected signals. The first direct detection of a wave was achieved by LIGO in 2015. The measured change in the 4-km LIGO arms was of the order of $4{\times}10^{-16}$ cm, which is 200 smaller than the radius of a proton (see e.g., Miller & Yunes 2019). Between 2015 and 2017, the LIGO-Virgo Collaboration has completed the first two runs and reported the detection of 10 mergers of stellar black holes and 1 neutron star merger (Abbott et al. 2019).

Precisely, the detection of the coalescent neutron stars was a revolutionary event for the scientific community, given that the electromagnetic counterpart was also observed. On 17 August 2017, the LIGO-Virgo Collaboration reported a gravitational wave consistent with the merger of two neutron stars. Independently, the space telescopes *Fermi* and INTEGRAL detected a short gamma-ray burst after 1.7 s of the gravitational wave signal. The alert started an intense astronomical campaign across the whole electromagnetic spectrum including more than 70 telescopes. Unfortunately, no neutrino or CR coincidences were found (Abbott et al. 2017).

Gamma-ray bursts were first observed in the 1960s. The connection of these events with neutron star binary systems was proposed a long time ago, as well as the production of elements heavier than iron in these scenarios (Eichler et al. 1989). The multi-messenger detection of the signal in 2017 was the final confirmation of theoretical models, remarking the relevance of the multi-messenger studies.

2.2 Sources

Many sources have been proposed as candidates for CR accelerators. For the Galactic CRs, the most promising and studied sources are the supernova remnants (SNRs). The CR energy density observed in the solar neighborhood can be explained if the 10 % of the energy injected in the supernova (SN) explosions are injected in relativistic particles. Nevertheless, CRs with energies beyond 1 PeV cannot be understood in terms of SNRs. Moreover, particles with energies above this limit have Larmor radii larger than the Galactic size, and therefore, they are not expected to remain confined in the Milky Way. As discussed in the last section, where exactly the Galactic to extragalactic transition occurs is not clear.

In this section, we focus only on the extragalactic objects that have been pointed out as the most prominent candidates for the particles with the highest energies: the SBGs and the AGNs.

2.2.1 Starburst galaxies

Starburst galaxies (SBGs) are galaxies with very high star formation rates (SFRs). These days, the fraction of observed galaxies undergoing a starburst phase is small, but in the early Universe, they were more common and played an important role in the re-ionization epoch (see e.g., Sharma et al. 2016). The SBGs were first noted by Searle et al. (1973), when they were making color-color diagrams for galaxies and realized that some of the objects were bluer than the theoretical expectations in the case of steady and continuous star formation. There is not full agreement about how to define a SBG. The criterion mostly used to identify these galaxies is to look for objects with ultraviolet (UV) and far-infrared (FIR) excesses, and strong narrow emission-lines. The problem with this definition is that often, the objects are not simultaneously found in the different catalogs, e.g., galaxies in the FIR catalogs normally do not appear in UV or emission-line surveys because they are dust-rich and the emission is heavily absorbed. Since the luminosity of the starburst region (L_{SB}) is comparable with the luminosity of the entire host galaxy (L_G), an alternative is to define a SBG as a galaxy with a luminosity dominated by the emission of the starburst, i.e., $L_{SB} \gg L_G$ (Terlevich 1997). Previously, SBGs were also classified taking into account the duration of the starburst activity. Given that the SFR is so high, it can not be sustained over a cosmological timescale because the necessary gas exceeds the total amount of gas observed in galaxies. Nonetheless, to apply this classification requires to know how the gas in the galaxy evolves. In other words, it is necessary to know how the gas converted into stars is distributed between the different masses (i.e., the initial mass function), how much of the gas escapes, etcetera. The uncertainties of these quantities are quite large, turning out this identification of SBGs to be imprecise.

Given that the SFR scales with the gas density, starburst regions have high gas densities (see e.g., Schmidt 1959; Kennicutt 1998b). The starburst phenomenon is observed to be related to galaxies in interacting systems (Larson & Tinsley 1978). During the encounter of two galaxies, the gas in the disk loses angular momentum due to the gravitational torque and dissipation. To conserve the angular momentum,

Figure 2.8: Image of the starburst galaxy M82 composed by the observations done with three different filters of the Hubble Telescope. The superwind bubbles are detected emitting H_α lines (in red). Credits: NASA and STScI.

the gas flows towards the center of the galaxy and the nuclear densities grow at least one order of magnitude (Conti et al. 2008).

The heating of the interstellar medium (ISM) is dominated during the first $\sim$ 3 Myr of the starburst episode by the photons of the hot young stars. These stars leave the main-sequence very fast and develop strong winds. After that, the first core-collapse SNe occur. The amount of SNe is so large that the remnants merge before they lose their energy. The collisions between SNRs produce shock waves, which thermalize the matter injected by the explosions. The starburst region becomes then a cavity filled with hot gas ($T \sim 10^8$ K), and the gas expands adiabatically until it reaches the edge of the starburst region. At this moment, its velocity is supersonic and, since its temperature is so large, it is not gravitationally bounded to the galactic disk anymore. The hot gas escapes the system, carrying away gas from the galactic disk. This matter is then injecting into the galactic halo, becoming a multi-phased outflow with cool, warm, hot, and relativistic components. The hot gas expanding in the halo produces a X-ray emitting superbubble surrounded by swept-up matter of lower temperature ($T \sim 10^4$ K) that radiates Hα lines (see Fig. 2.8). This outflow is called superwind and it is observed in edge-on galaxies reaching distances of $\sim$ 10 kpc from the galactic disks (see e.g., Strickland et al. 2002). In the halo of nearby starbursts, synchrotron radiation is also measured (see e.g., Heesen et al. 2009a). These observations are supposed to be associated with the presence of relativistic particles in the superwind. We will discuss this issue further in Chapter 4, where a model to accelerate particles in the large-scale shocks produced by the interaction of the superwind with the halo matter is presented.

2.2.2 Active galactic nuclei

Baade & Minkowski found in 1953 that the radio object Cygnus A is extragalactic and possesses a synchrotron radio luminosity much larger than its optical emis-

sion. Moreover, they reported that the shape of the galaxy in radio was consistent with a pair of colliding galaxies. Nevertheless, Jennison & Das Gupta (1953) using interferometric techniques showed that the radio radiation is produced in two big lobes, almost symmetrically placed with respect to the optical emitting region. The estimation done by Burbidge (1956) pointed out that the minimum energy required to explain such emission is equivalent to the energy injected by 10^7 SNe. This fact suggested that some efficient mechanism is needed in objects like Cygnus A to release such a large amount of energy into the intergalactic space. This discovery was followed by the identification of rare bright "stars", which were found to be very distant objects, namely quasars (Matthews & Sandage 1963; Sandage et al. 1965).

Nowadays, we know that these phenomenons are explained by supermassive black holes (BHs) accreting matter in the center of those galaxies. The accretion consists of matter falling into the gravitational potential well of the BH. The accretion properties of the BHs are usually referred to or compared with *Eddington* quantities. The Eddington limit emerges of taking into account that a photon field can inhibit the accretion process if the gravitational and radiation pressure are equal. If we assume that the symmetry of the problem is spherical[7], the radiation force of a source of luminosity L and the gravitational force on each proton[8] at a radius r result in

$$F_{\rm rad} = \frac{\sigma\, L}{4\,\pi\, r^2\, c} \quad \text{and} \quad F_{\rm grav} = \frac{G\, M\, m_p}{r^2}, \tag{2.2}$$

respectively. Balancing both equations, we obtain $L = L_{\rm Edd} = 4\,\pi\, G\, M\, m_p\, c/\sigma$, where M is the mass of the accreting object and σ is the cross section for the interaction between matter and photons. Considering that the radiation interacts principally via Compton scattering with the electrons of the hydrogen atoms, σ becomes the Thomson cross section[9]. Then, $L_{\rm Edd} \approx 1.3 \times 10^{38} (M/M_\odot)\,{\rm erg\,s^{-1}}$. The Eddington bound is not strict and can be exceeded if the source is non-stationary or the accretion geometry is special. Nevertheless, its value is commonly used to evaluate the accretion properties of a source of mass M. Indeed, the accreting material forms usually a disk as a consequence of its angular momentum. Disks are thin or thick, depending on the ratio between their radius and height at each point. The accretion process releases a large amount of the energy contained in the disk matter, with typical efficiencies between 8 % and 42 % for thin disks around Schwarzschild and co-rotating Kerr BHs, respectively (see e.g., Romero & Vila 2014a, for more details).

The characteristic AGN emission comes from a very compact region and covers a wide range of frequencies, from radio to gamma rays (Padmanabhan 2002). Nevertheless, the observed spectral energy distributions (SEDs) are far from homogeneous, and therefore, many subclasses of these objects are defined. AGNs are first separated into two big groups based on their radio emission: radio-quiet and radio-loud objects. The former have radio luminosities several times larger than the observed in galaxies with radio-quiet nuclei. This fact is attributed to the existence of a relativistic jet emitting synchrotron radiation. Additionally, these groups can be divided according to the intensity of the lines in their spectra, the alignment of the jet with the line

[7] This is known as spherical accretion.

[8] Assuming the accreting matter is mainly neutral hydrogen.

[9] The protons are dragged outwards along with the electrons as a consequence of their Coulombic attraction.

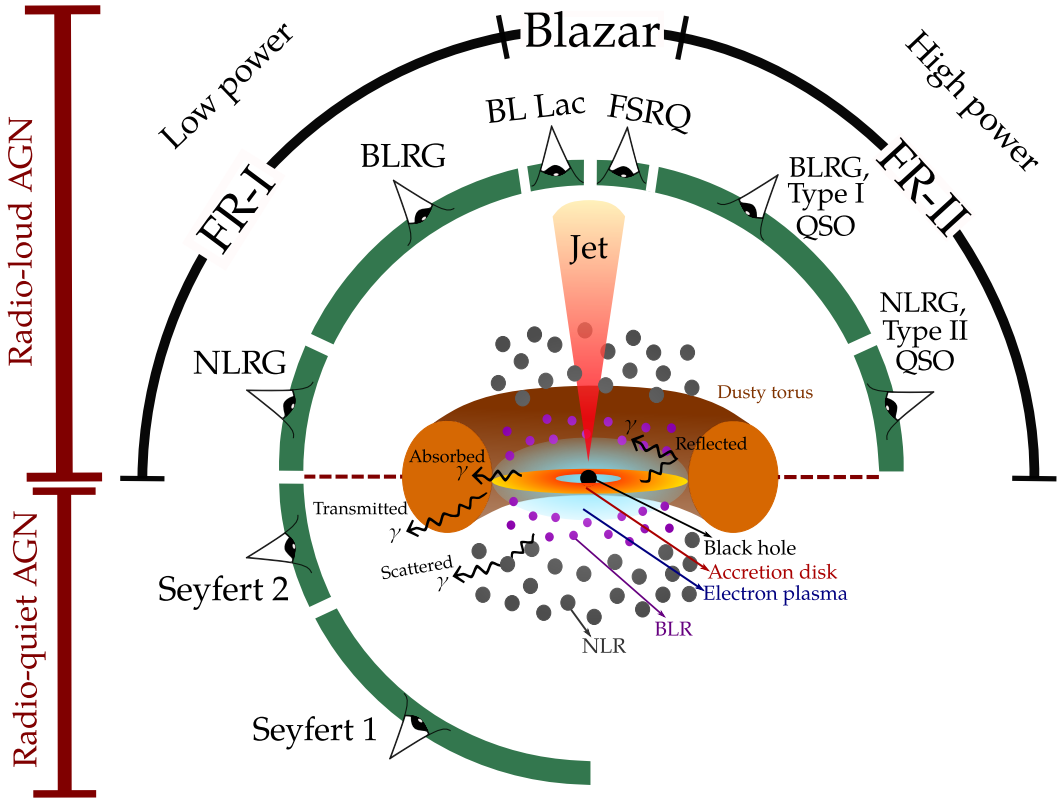

Figure 2.9: Scheme of the AGN unified model. Based on Beckmann & Shrader (2012).

of sight, etcetera (see Dermer & Giebels 2016). All the subclasses of AGNs can be understood in terms of a unified model (Antonucci 1993; Urry & Padovani 1995). This unified explanation suggests that an AGN is a supermassive BH surrounded by a sub-parsec accretion disk and a dusty torus. Inside the region delimited by the torus, the broad-line region (BLR) and the narrow-line region (NLR) clouds move in Keplerian orbits. The different observational behaviors of AGNs are explained by different values of black hole masses, accretion rates, and orientations to the observer as shown in Fig. 2.9. In Chapter 6, we present a model to accelerate particles in shocks led by the collisions of BLR clouds with accretion disks and apply it to the Seyfert 2 galaxy NGC 1068.

3

Physics for high-energy astrophysics

The main goal of this thesis is the analysis of different scenarios of potential particle acceleration in starburst galaxies and active galactic nuclei. To do this, this chapter introduces all the concepts and formulas needed to address the studies presented in the Chapters 4–6.

3.1 The Hillas criterion

Magnetic fields play a key role in the existence of cosmic rays (CRs). The strength of the magnetic field affects not only the acceleration process, but also imposes a limit on the highest energies that particles can obtain in a defined region. The latter was discussed by Hillas (1984). At that moment, the extension of the CR spectrum up to 10^{20} eV was known and models explaining the production of CR up to $\sim 10^{15}$ eV in supernova remnants (SNRs) were already proposed. In his work, Hillas displayed the famous plot indicating candidate sources of ultra-high energy cosmic rays (UHECRs).

The basic idea of the Hillas criterion is that the particle can be accelerated as long as it remains inside the acceleration region. Once the particle escapes, the acceleration stops, and its energy does not increase anymore. As we will discuss in the next section, particles typically gain energy in regions where magnetic fields exist. A relativistic particle[1] of charge $e\,Z$ and energy E, moving perpendicularly to a magnetic field B, describes a circular motion with a radius known as gyroradius or Larmor radius

$$r_{\mathrm{L}} = \frac{R}{B} \approx \frac{E}{e\,Z\,B}, \tag{3.1}$$

where $R \approx E/(e\,Z)$ denominates the rigidity of the particle.

Once the gyroradius of the particle becomes larger than the characteristic length of the acceleration site, the particle is not confined by the magnetic field and leaves the region. Therefore, a first constraint to the maximum energies that particles can reach in a source is given by[2] (see e.g., Longair 2011; Gaisser et al. 2016)

$$E_{\mathrm{max}} = e\,Z\,X\,B = 10^{18}\,Z \left(\frac{X}{\mathrm{kpc}}\right)\left(\frac{B}{\mu\mathrm{G}}\right)\ \mathrm{eV} \tag{3.2}$$

[1] For the following expressions we assume that the energy of the particle is much larger than its rest mass energy. Otherwise, E should be replaced by $p\,c$, where p is the total momentum of the particle and c is the light speed.

[2] Actually, the restriction found by Hillas (1984) in the context of diffusive acceleration mechanisms is $E < 0.5\,e\,Z\,X\,B\,\beta$, which is stronger than the one here presented. He started with the condition of $X > 2\,r_{\mathrm{L}}$, and took also into account the effect of the velocity of the scatter centers $\beta = U/c < 1$.

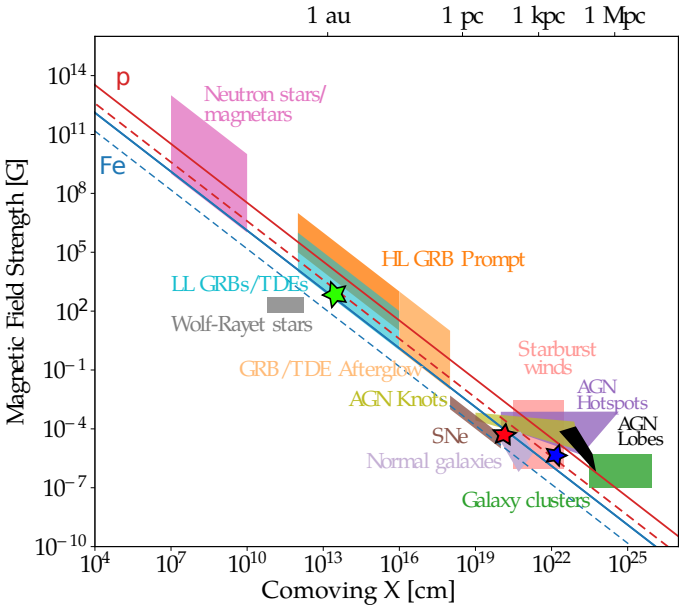

Figure 3.1: Taken from Alves Batista et al. (2019) and modified. The dash lines correspond to particles with energy 10^{19} eV, whereas the solid lines with 10^{20} eV. The stars indicate the position of the sources discussed in Chapter 4 (blue), Chapter 5 (red), and Chapter 6 (green), according to the Hillas criterion.

where X is the size of the acceleration region.

In the original plot of Hillas, some sources like gamma-ray bursts (GRBs) or tidal disruption events are not included because they were unknown at that time. Figure 3.1 shows an updated version of this diagram, including the points corresponding to the sources studied in Chapters 4–6. Nevertheless, the maximum energies that particles can attain in a source are usually much smaller than those yielded by the Hillas criterion. The maximum energy arises from the balance of all the processes taking place at the source. The properties and the conditions in the acceleration environment occasion that the particle gains energy but simultaneously loses it because of the interaction with the local fields. Moreover, the particle can be removed from the acceleration region before it manages to reach the Hillas maximum. Consequently, establishing the maximum particle energies requires, in general, more detailed analyses that characterize the source as good as possible. In this chapter, we present a summary of the most common processes competing with the acceleration.

3.2 Transport Equation

The distribution of particles injected by the acceleration is modified by all the other processes taking place at the source. The preferred acceleration mechanisms are based on the diffusion of the particles, as we will see in the next section. Furthermore, all the changes suffered by the particle distribution are statistical. Therefore, to find the CR spectrum at the source requires to solve the Fokker-Planck equation, whose

terms vary depending on the involved processes. Some general form of this equation is given by (see e.g., Ginzburg & Syrovatskii 1964; Longair 2011)

$$\begin{aligned}\frac{\partial N_i(E,\vec{r},t)}{\partial t} =& Q_i(E,\vec{r},t) + \frac{\partial[b(E)\,N_i(E,\vec{r},t)]}{\partial E} + \frac{1}{2}\frac{\partial^2}{\partial E^2}\left[d_i(E)N_i(E,\vec{r},t)\right] \\ &+\nabla\cdot[D_{\rm i}(E,\vec{r},t)\,\nabla N_i(E,\vec{r},t)] - V\cdot\nabla N_i(E,\vec{r},t) \\ &-p_i N_i(E,\vec{r},t) + \sum_{k>i} p_i^k N_k(E,\vec{r},t),\end{aligned} \tag{3.3}$$

where $N_i(E,\vec{r},t)$ is the density of particles of type i at some energy E, position $\vec{r}$, and instant t. The first term on the right side of the equation is the injection term. In the second term, $b(E) = \sum_j dE_j/dt$ is the sum of all the systematic energy variations suffered by the particle. The third term accounts for fluctuating changes in the energy, where $d_i(E) = d\overline{\Delta E^2}/dt$ is the mean square of the energy fluctuation per unit of time. The fourth and fifth terms describe the spatial diffusion with a diffusion coefficient $D_i(E,\vec{r},t)$ and the convection of particles in a fluid with a velocity V, respectively. The last two terms on the right-hand side of the equation take into account the possibility of particles i disappearing or appearing in the region of interest. In particular, the penultimate term allows that particles of type i disappear (p_i is the associated probability of this to occur), whereas the last one accounts for particles of type k fragmenting into particles of type i. The probability of a particle of type k to spall into particles of type i is p_i^k.

In the context of this thesis, we calculate only the distributions of electrons and protons, considering they are independent of the position inside the acceleration region. Hence, Eq. (3.3) can be simplified as

$$\frac{\partial N_{e,p}(E,t)}{\partial t} = Q_{e,p}(E,t) + \frac{\partial[b_{e,p}(E)\,N_{e,p}(E,t)]}{\partial E} - \frac{N_{e,p}(E,t)}{\tau_{\rm esc}(E)}, \tag{3.4}$$

assuming there are no significant energy fluctuations. The term $N_{e,p}(E,t)/\tau(E)_{\rm esc}$ accounts for the effects of the diffusion and convection terms, representing with $\tau_{\rm esc}$ the characteristic timescale for the escape of the particles. As can be noted, this equation can be further simplified whether the time dependency or energy changes can be neglected.

Equation (3.3) is also employed to study the propagation of the particles from the source to the Earth. In some situations described by this partial differential equation, analytical solutions can be found using methods like Green's function (see e.g., Ginzburg & Syrovatskii 1964). Nevertheless, if the complexity of the equation is high, resorting to numerical solutions can be more convenient. In the next section, we present some particular approaches to find the particle distribution in the specific circumstances of an acceleration mechanism.

3.3 Acceleration mechanisms

Many mechanisms have been proposed over the years to explain the acceleration of CRs in different sources (see e.g., Berezinskii et al. 1990). In general, CRs are thought to be accelerated due to the electromagnetic fields existing in the astrophysical sources

or the interstellar medium[3]. Here, we concentrate principally on two mechanisms derived from the original idea of Fermi (1949) that we invoke in the scenarios studied in this thesis. Some other mechanisms are briefly described at the end of this section.

3.3.1 Fermi's original idea

In 1949, Fermi suggested that CRs are mainly accelerated by the interaction of the particles with magnetized clouds, which move randomly in the interstellar space with velocities of $\sim 15\,\mathrm{km\,s^{-1}}$. These clouds of plasma act like *magnetic mirrors*: the particle enters the cloud, is reflected in the inhomogeneities of the magnetic field inside this, and finally emerges with a different energy. Fermi showed that, even when the change in the energy is very small after each collision, the encounters with clouds rise stochastically the energy of the particle. A process of this kind leads naturally to a power law energy distribution for the particles (see e.g., Protheroe 1999; Longair 2011; Gaisser et al. 2016), as we demostrate in what follows.

Considering that a particle of energy E suffers a change in its energy $\Delta E = \xi\, E$ after a collision with a cloud. After n collisions, the total energy variation can be written as

$$E_n = E_0\,(1+\xi)^n, \tag{3.5}$$

where E_0 is the energy of the particle at the beginning of the acceleration process. In each encounter with a cloud, there is a probability $P_{\rm esc}$ of the particle leaving the acceleration region[4]. Then, $(1-P_{\rm esc})^n$ gives the probability of the particle remaining in the accelerator after n collisions.

From Eq. (3.5) it is simple to show that the number of collisions needed by a particle to achieve some energy E

$$n = \frac{\ln(E/E_0)}{\ln(1+\xi)}. \tag{3.6}$$

The number of particles with energies above E is proportional to the sum of the probabilities of not escaping the region after m collisions[5], where $m \geqslant n$

$$N(\geqslant E) \propto \sum_{m=n}^{\infty} (1-P_{\rm esc})^m = \frac{(1-P_{\rm esc})^n}{P_{\rm esc}} \tag{3.7}$$

Finally, replacing n with the result obtained in Eq. (3.6) we get

$$N(>E) \propto \frac{1}{P_{\rm esc}} \left(\frac{E}{E_0}\right)^{-(\Gamma-1)} \tag{3.8}$$

with $\Gamma = 1 - \frac{\ln(1-P_{\rm esc})}{\ln(1+\xi)}$. The integral form of the last expression is then $N(E) = N_0\, E^{-\Gamma}$.

Let us now calculate the energy growth in Fermi's proposal. A particle of energy E_1 enters a cloud of turbulent magnetized plasma and starts to reflect in the irregularities

[3] We use to speak in terms of the magnetic field, but of course the acceleration is produced by the induced electric field.

[4] In the original case of Fermi, this is the probability of escaping the Galaxy.

[5] We use that $\sum_{k=0}^{\infty} x^k = 1 - x^{-1}$ for $x < 1$.

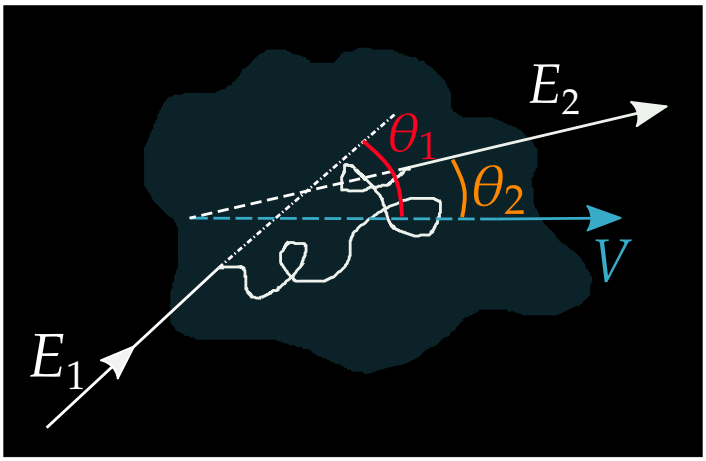

Figure 3.2: Scheme of the mechanism proposed by Fermi (1949). Adapted form Protheroe (1999).

of the magnetic field. After a few reflections, the average motion of the particle is lined up with the motion of the cloud (see Fig. 3.2). Assuming that the particle is already highly relativistic[6], $E \approx p\,c$, and the total energy of the particle in the rest frame of the gas is

$$E'_1 = \gamma\, E_1\,(1 - \beta\, \cos\theta_1), \tag{3.9}$$

where γ is the Lorentz factor of the cloud and $\beta = V/c$, with V the cloud velocity. The particle scatters inside the cloud because of the interactions with the magnetic field. Consequently, these are elastic interactions, and the energies of the particle before and after become $E'_2 = E'_1$ in the rest frame of the cloud. Using the Lorentz transformations, the energy of the particle after the interaction with the cloud in the lab frame is

$$E_2 = \gamma\, E'_2\,(1 - \beta\, \cos\theta'_2). \tag{3.10}$$

Then,

$$\frac{\Delta E}{E_1} = \frac{E_2 - E_1}{E_1} = \frac{1 - \beta\, \cos\theta_1 + \beta\, \cos\theta'_2 - \beta^2\, \cos\theta_1\, \cos\theta'_2}{1 - \beta^2} - 1. \tag{3.11}$$

To obtain the average energy gained by the particle in an encounter with a cloud, we need to calculate the average values of the angles. The CR inside the cloud is reflected many times in the magnetic inhomogeneities and therefore, its direction is randomized, then $< \cos\theta'_2 >= 0$. On the other hand, $< \cos\theta_1 >$ depends on the rate at which particles collide with clouds at different angles. The probability of having a collision at angle θ_1 per solid angle is proportional to the relative velocity between the CR and the cloud $v_{\rm rel} = v - V\, \cos\theta_1 \approx c\,(1 - \beta\, \cos\theta_1)$. Consequently,

$$\frac{dP}{d\Omega_1} \propto (1 - \beta\, \cos\theta_1) \quad \text{with } -1 \leqslant \cos\theta_1 \leqslant 1, \tag{3.12}$$

[6]This means the rest mass energy of the particle is a negligible fraction of the total particle energy and the velocity of the particle $v \approx c$.

and

$$< \cos\theta_1 >= \frac{\int \cos\theta_1 \frac{dP}{d\Omega_1} d\Omega_1}{\int \frac{dP}{d\Omega_1} d\Omega_1} = \frac{\int_{-1}^{1} \cos\theta_1 (\beta\ \cos\theta_1 - 1)\, d\cos\theta_1}{\int_{-1}^{1} (\beta\ \cos\theta_1 - 1)\, d\cos\theta_1} = -\frac{\beta}{3}. \tag{3.13}$$

Finally, replacing in Eq. (3.11) we find

$$\frac{< \Delta E >}{E_1} = \frac{1 + \beta^2/3}{1 - \beta^2} - 1 \approx \frac{4}{3}\beta^2, \tag{3.14}$$

since $\beta \ll 1$.

The last result shows that, even when the particle loses energy in rear-end collisions, the average energy change after many cloud-particle interactions is positive and, therefore, the mechanism accelerates the particle. Nevertheless, this process is very inefficient since the energy rises with the square of β, which is extremely small considering that the clouds have typically velocities of a few tens of km s^{-1}. This kind of acceleration mechanism is denominated second-order Fermi mechanism since the energy increases with the square of β. In the next two sections, we present the two modern variants of Fermi's original proposal employed in the context of this thesis.

3.3.2 Stochastic Diffusive Acceleration

The contemporary version of the second-order Fermi mechanism replaces the interstellar clouds by turbulent astrophysical plasmas. Magnetized turbulence in astrophysical flows has been observed in many different scenarios, e.g., the solar wind or galaxy clusters (see e.g., Beresnyak & Lazarian 2019). Turbulence is a property typically observed in fluids with large-scale motions, but with low friction. Nevertheless, how exactly the perturbations are driven in astrophysical environments is not well understood. The turbulence of a medium is characterized by the dimensionless Reynolds number

$$Re = \frac{X\,V}{D}, \tag{3.15}$$

where X and V are the scale and velocity of the flow, respectively, and D the spatial diffusion coefficient[7] (cm^2 s^{-1}) (Bustard et al. 2017). Flows with $Re \gg 1$ are typically denominated turbulent, increasing the turbulence with increasing Re.

The concept of turbulence is usually associated with the idea of chaos, but this phenomenon can be often described statistically. The magnetic turbulence can be thought of as a superposition of hydromagnetic waves following some power spectrum. Hydromagnetic waves are mostly known as Alfvén waves, whose characteristic velocity is given by

$$v_{\rm A} = \frac{B_0}{\sqrt{4\,\pi\,\rho}}. \tag{3.16}$$

Here B_0 is the strength of the magnetic field and ρ the density of the medium.

[7] In non-astrophysical plasmas is most commonly called kinematic viscosity ν, but since $\nu \sim v\,l$, whereby v is the velocity of the diffusing particle and l its mean free path, it results in a diffusion coefficient (Shu & Hughes 1992).

If the power spectrum of the Alfvén waves is of the form $W(k) \propto k^{-q}$, where $k = 2\pi/\lambda$ with λ the wavelength, the turbulence can be written as (O'Sullivan et al. 2009)

$$\frac{\delta B^2}{8\pi} = \int_{k_{\min}}^{k_{\max}} W(k)\, dk, \tag{3.17}$$

where $k_{\max}$ and $k_{\min}$ correspond to the shortest and longest wavelengths, respectively. Assuming that the spectral index is $q = 1$, the energy diffusion coefficient (erg^2 s^{-1}) gets (Asano & Mészáros 2016; Stawarz & Petrosian 2008; Hardcastle et al. 2009)

$$K(E) \approx \frac{\delta B^2}{B_0^2} \left(\frac{v_A}{c}\right)^2 \left(\frac{c}{r_L}\right) E^2 \tag{3.18}$$

and the associated acceleration timescale

$$t_{\rm acc}^{\rm SDA} = E\left(\frac{dE}{dt}\right)^{-1} = \frac{E^2}{K(E)} \approx \left(\frac{v_{\rm A}}{c}\right)^{-2} \left(\frac{\delta B^2}{B_0^2}\right)^{-1} \left(\frac{r_{\rm L}}{c}\right). \tag{3.19}$$

Equation (3.19) shows that the average energy gain of a particle produced by this mechanism is proportional to $(v_A/c)^2$ (e.g., Stawarz & Petrosian 2008; O'Sullivan et al. 2009; Petrosian 2012). This result is analogous to the one obtained in the previous section, but now the velocity of the magnetic mirrors is the velocity of the hydromagnetic waves rather than of the interstellar clouds. Therefore, this mechanism is denominated stochastic diffusive acceleration (SDA).

The energy distribution of particles being only accelerated by this mechanism is described by the expression (see e.g., Petrosian & Liu 2004; Petrosian 2012)

$$\frac{\partial N_{e,p}(E,t)}{\partial t} = \frac{\partial}{\partial E}\left[K(E)\frac{\partial N_{e,p}(E,t)}{\partial E}\right] - \frac{\partial}{\partial E}\left[\left(\frac{2\,K(E)}{E}\right) N_{e,p}(E,t)\right]. \tag{3.20}$$

The spectral index of the produced particle spectrum is typically hard, with $\Gamma \sim 1$ (see e.g., Stawarz & Petrosian 2008). Numerical methods are very helpful to find the solution to this transport equation, especially in cases where extra terms such as energy losses or particle injection should be also included (Park & Petrosian 1996). For the analysis presented in Chapter 4, we employ the implicit finite difference method proposed by Chang & Cooper (1970), which is easily resolved using a routine of Gaussian elimination with back substitution, as shown in Appendix A.3.

3.3.3 Diffusive Shock Acceleration

Another version of Fermi's mechanism was suggested in the 1970s by several authors (Axford et al. 1977; Krymskii 1977; Bell 1978; Blandford & Ostriker 1978). The benefit of this modification is the rise of the average energy gained by the particle, which goes linear with β instead of quadratic. Because of this, the process received the name of first-order Fermi mechanism and it was first proposed to work in supernovae (SNe).

The conditions for more efficient acceleration of particles are supplied by an adiabatic, strong[8], and super-Alfvénic[9] shock wave. Again, the general situation is

[8]The acceleration requires a Mach number larger than $\sqrt{5}$ (Vink & Yamazaki 2014).

[9]$V_{\rm sh} > v_{\rm A}$.

very similar to the one discussed in Section 3.3.1, but the particles are scattered by the magnetic irregularities at each side of the shock instead of interstellar magnetized clouds. The shock path is expected to leave behind a perturbed medium, where magnetic inhomogeneities should exist. Since the shock is required to be super-Alfvénic, the bulk streaming of relativistic particles coming from the downstream region excites resonantly Alfvén waves ahead of the shock inducing turbulence (see e.g., Bell 2004). Consequently, particles recross the shock multiple times, increasing their energy at each crossing, and therefore, the mechanism is usually called diffusive shock acceleration (DSA) (Bell 1978). Equations (3.9)–(3.11) are also valid in this scenario. Nevertheless, the average values of $< \cos\theta_1 >$ and $< \cos\theta_2' >$ become different given the geometry of the problem. As opposed to the cloud scenario, a planar shock prevents the occurrence of rear-end collisions with the magnetic irregularities (see Fig. 3.3). The particle always encounters the "mirrors" ahead of its trajectory, and therefore, only gain energy interactions happen. The probability of a certain $\cos\theta_2'$ in solid angle corresponds then to the normalized projection of an isotropic flux onto the shock plane (Gaisser et al. 2016)

$$\frac{dP}{d\Omega_2'} = 2\cos\theta_2' \quad \text{with } 0 \leqslant \cos\theta_2' \leqslant 1. \tag{3.21}$$

Repeating the calculation done in Eq. (3.13), $< \cos\theta_2' >= 2/3$. The distribution of $\cos\theta_1$ is again the associated with a isotropic flux being projected onto a plane, but with $-1 \leqslant \cos\theta_1 \leqslant 0$ (see Fig. 3.3). Then, $< \cos\theta_1 >= -2/3$ and Eq. (3.11) becomes

$$\frac{\Delta E}{E} = \frac{1 - \frac{4}{3}\beta + \frac{4}{9}\beta^2}{1-\beta^2} - 1 \approx \frac{4}{3}\beta. \tag{3.22}$$

Here, $\beta = \frac{R-1}{R}\frac{V_{\rm sh}}{c}$, where $V_{\rm sh}$ is the velocity of the shock and R its density ratio[10]. The energy gained by the particle is finally given by (see e.g., Drury 1983; Protheroe 1999)

$$\left.\frac{dE}{dt}\right|_{\rm acc} = \eta\, e\, Z\, c\, B, \tag{3.23}$$

with η the acceleration efficiency. The value of η depends on the diffusion coefficient D at the shock, the velocity $V_{\rm sh}$, and the angle between the magnetic field and the normal to the shock plane. If the shock propagates parallel to the magnetic field

$$\eta \approx \frac{3}{20}\left(\frac{D}{D_{\rm B}}\right)^{-1}\left(\frac{V_{\rm sh}}{c}\right)^2 \tag{3.24}$$

whereas for a perpendicular configuration

$$\eta \approx \frac{3}{8}\left(\frac{D}{D_{\rm B}}\right)\left(\frac{V_{\rm sh}}{c}\right)^2. \tag{3.25}$$

[10]The density ratio is equal to the downstream density divided by the upstream density. In strong shocks, $R \to (\gamma_{\rm ad}+1)/(\gamma_{\rm ad}-1)$, where $\gamma_{\rm ad}$ is the adiabatic index of the gas (see e.g., Landau & Lifshitz 1987; Clarke & Carswell 2007).

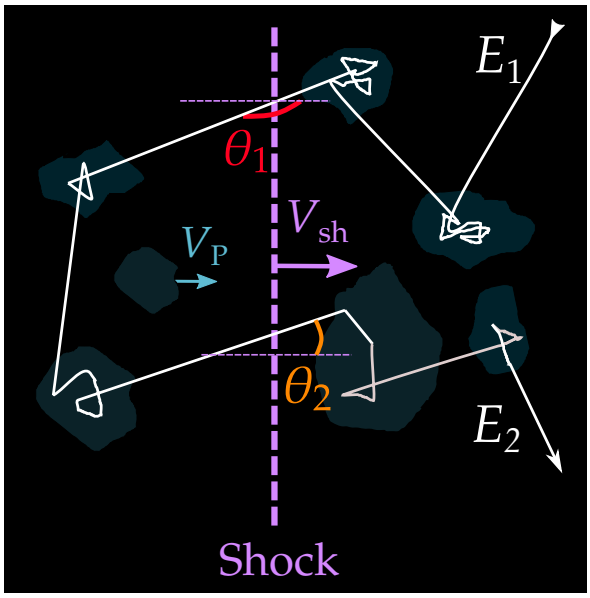

Figure 3.3: Scheme of the shock acceleration mechanism. Adapted form Protheroe (1999).

Here, $D_B = c\, r_L/3$ is the Bohm diffusion coefficient. Oblique configurations are also discussed in the literature, but they need a more complex treatment (see e.g., Schlickeiser 2002). Finally, the acceleration timescale results in

$$t_{acc}^{DSA} = \frac{E}{dE/dt|_{acc}} = \eta^{-1} \frac{E}{e\, Z\, c\, B}. \tag{3.26}$$

As mentioned above, the shock must fulfill some conditions to ensure particle acceleration. Therefore, in Section 3.3.3.1 a summary about shock waves is presented, and the procedure to check the shock properties is indicated.

The reasoning developed in Section 3.3.1 to find the distribution created by the original mechanism proposed by Fermi is also valid in the first-order acceleration case. Then, from Eqs. (3.6)–(3.8) we get that the distribution of particles injected result in $Q(E) = Q_0\, E^{-\Gamma}$, where $\Gamma = 1 - [\ln(1 - P_{esc})/\ln(1 + \Delta E/E)]$. The escape probability in the shock situation is given by r_{loss} divided by r_{cross}, where r_{loss} and r_{cross} are the rate at which CRs are lost downstream and at which they cross from upstream to downstream, respectively. If the shock is non-relativistic and assuming that the particles upstream are distributed isotropically, it can be shown that $P_{esc} \approx 4\, V_{sh}/(R\, v)$, with v the particle velocity (Protheroe 1999). Since the particle is assumed to be highly relativistic, $v \approx c$, and $\Gamma \approx (R + 2)/(R - 1)$ (see e.g., Romero & Paredes 2011). A non-relativistic strong shock in a monatomic gas medium has a density ratio $R = 4$. For this reason, Γ is typically considered to be 2. In more detailed analyses, it is found that the effects of the CR pressure or the diffusion in a finite medium cause the spectral index to be harder or steeper, respectively (Dermer & Giebels 2016).

The characteristic transport equation Eq. (3.3) in a source where particles are being injected by DSA becomes Eq. (3.4). In the particular case where the particle distribution is time-independent and the τ_{esc} can be considered constant, Eq. (3.4) gives

$$\frac{N_{e,p}(E)}{\tau_{esc}} - \frac{\partial[b_{e,p}(E)\, N_{e,p}(E)]}{\partial E} = Q_{e,p}(E), \tag{3.27}$$

whose analytical solution is (Ginzburg & Syrovatskii 1964)

$$N_{e,p}(E) = \left|b_{e,p}(E)\right|^{-1} \int_{E_{\rm min}^{e,p}}^{E_{\rm max}^{e,p}} dE' Q_{e,p}(E') \exp\left(-\frac{\tau_0(E,E')}{\tau_{\rm esc}}\right), \tag{3.28}$$

with

$$\tau_0(E,E') = \int_E^{E'} dE'' \left|b_{e,p}(E'')\right|^{-1}. \tag{3.29}$$

One last remark about this acceleration process is the uncertainties about the seed particles. Despite all the observational evidence in favor of DSA, which particles can take place in the acceleration process remains unclear (Longair 2011). To start the diffusion from one side to the other of the shock, the particles should have already supra-thermal energies. Nowadays, the origin of these particles is known as the injection problem and it is still under debate (see e.g., Marcowith et al. 2020, and references therein).

3.3.3.1 Shock physics

Shock waves are observed to exist in many astrophysical objects such as SNe, runaway stars, galaxy clusters, active galactic nuclei (AGNs), among others. A shock is essentially a perturbation moving through a fluid with a velocity larger than the local speed of the sound $c_{\rm s}$. This velocity $c_{\rm s}$ in an ideal gas can be calculated as

$$c_{\rm s} = \sqrt{\frac{\gamma_{\rm ad}\, k_{\rm B}\, T}{\mu\, m_{\rm H}}}, \tag{3.30}$$

with T is the temperature of the medium, $\gamma_{\rm ad}$ is the adiabatic index, $k_{\rm B}$ the Boltzmann constant, and $\mu\, m_{\rm H}$ the mean mass per particle in the gas. If the medium is mainly composed by hydrogen, $c_{\rm s} \approx 300 \sqrt{T/10^7\,{\rm K}}\,{\rm km\,s^{-1}}$.

Astrophysical shocks are typically produced by fluids moving supersonically through the space. When two flows of gas of densities $n_{\rm a}$ and $n_{\rm b}$ collide supersonically, a pair of shocks is created. In the frame of reference where one of the fluids is at rest ($v_{\rm a} = 0$) and the other one moves with a velocity $v_{\rm b}$, the velocities of the shocks are given by (see, e.g., Tenorio-Tagle 1981; Lee et al. 1996)

$$v_{\rm rev} = -\frac{4}{3}\,\frac{1}{1+\sqrt{n_{\rm a}/n_{\rm b}}}\, v_{\rm b}, \tag{3.31}$$

$$v_{\rm forw} = \frac{4}{3}\,\frac{1}{1+\sqrt{n_{\rm b}/n_{\rm a}}}\, v_{\rm b}. \tag{3.32}$$

The two generated shocks move in opposite directions. The one propagating parallel to $\overrightarrow{v_{\rm b}}$ is called forward shock, whereas the other one reverse shock.

Shocks are a discontinuity in the properties of the gas (see Fig. 3.4). Behind the shock, the medium is strongly disturbed and its physical characteristics are different but related to the properties of the unperturbed region. From the conservation laws[11], it is possible to obtain the Rankine-Hugoniot relations, or jump conditions,

[11] Mass continuity, conservation of momentum, and conservation of energy.

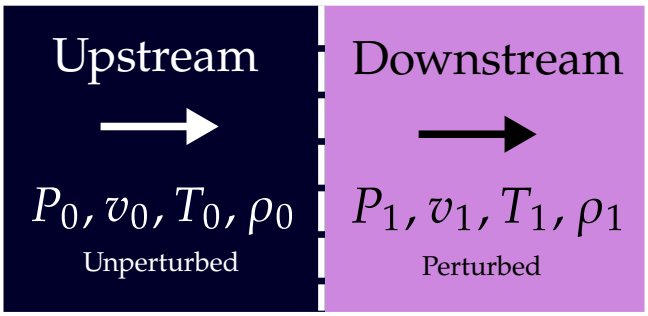

Figure 3.4: Scheme of the flow of the gas in the frame of reference in which the shock front is at rest.

considering an ideal, non-conductor, and steady state gas with a negligible magnetic field (Landau & Lifshitz 1987; Clarke & Carswell 2007)

$$\rho_0 \, \overrightarrow{v_0} = \rho_1 \, \overrightarrow{v_1} \tag{3.33}$$

$$\rho_0 \, {v_0}^2 + P_0 = \rho_1 \, {v_1}^2 + P_1 \tag{3.34}$$

$$\frac{\gamma_{\rm ad} \, P_0}{(\gamma_{\rm ad} - 1) \, \rho_0} + \frac{1}{2} \, {v_0}^2 = \frac{\gamma_{\rm ad} \, P_1}{(\gamma_{\rm ad} - 1) \, \rho_1} + \frac{1}{2} \, {v_1}^2, \tag{3.35}$$

where $\gamma_{\rm ad}$ is the adiabatic index.

Defining the Mach number of the gas as

$$M_0 = \frac{v_0}{c_s}, \tag{3.36}$$

the solution of Eqs. (3.33)–(3.35) for a strong shock ($M_0 \gg 1$) in a monatomic gas ($\gamma_{\rm ad} = 5/3$) becomes

$$\begin{aligned} v_1 &= \frac{v_0}{4} & \rho_1 &= 4 \, \rho_0 \\ P_1 &= \frac{3}{4} \, \rho_0 \, v_0^2 & T_1 &= \frac{3}{16} \frac{\mu \, m_{\rm H}}{k_{\rm B}} \, v_0^2. \end{aligned} \tag{3.37}$$

If we add a magnetic field $\overrightarrow{B_0}$ perpendicular to the shock normal, the following complementary equation is found

$$B_1 = \frac{\rho_1}{\rho_0} \, B_0. \tag{3.38}$$

This result shows that the medium behind the shock is compressed, its temperature, pressure, and magnetic field increased, whereas the fluid velocity is reduced.

In the case of two colliding streams of gas, since a pair of shocks is created, a contact discontinuity appears between the two perturbed media. Unlike a shock, the gas does not flow across this discontinuity. Consequently, the region splits into four areas with different physical properties as shown in Fig. 3.5.

In the previous analysis, we have considered that the shock is non-relativistic ($V_{\rm sh} < 0.1 \, c$), because this kind of shocks is studied in the astrophysical scenarios included in this thesis (see e.g., Dermer & Giebels 2016, for a relativistic analysis).

Figure 3.5: Scheme of four regions created by the supersonic collision of two gas streams. The dashed white lines represent the shock waves. The dashed black line is the contact discontinuity.

We have also assumed that the energy is conserved behind, as well as ahead, of the shock. This type of shocks with negligible radiative losses are denominated as adiabatic shocks. One way to determine the nature of the shock is by comparing its cooling length R_Λ with the characteristic length of the medium traversed by the shock. If the cooling length is longer, the shock is adiabatic, otherwise, it is radiative. An equivalent analysis can be done using the timescale of the thermal cooling t_Λ instead of R_Λ

$$t_\Lambda = \frac{R_\Lambda}{V_{sh}}, \tag{3.39}$$

where R_Λ is (McCray & Snow 1979)

$$R_\Lambda = \frac{1.90 \times 10^{-29}\, \mu\, (V_{sh}/\mathrm{km\,s^{-1}})^3}{(n_0/\mathrm{cm^{-3}})\,(\Lambda(T)/\mathrm{erg\,cm^3\,s^{-1}})}\ \mathrm{pc} \tag{3.40}$$

with

$$T = 18.21\, \mu \left(\frac{V_{sh}}{\mathrm{km\,s^{-1}}}\right)^2\ \mathrm{K}, \tag{3.41}$$

assuming the gas mainly composed of hydrogen, and n_0 the number density of the undisturbed medium. The factor μ is 0.6 if the material is ionized or 1.3 if it is neutral, and $\Lambda(T)$ (in $\mathrm{erg\,cm^3\,s^{-1}}$) is the cooling function (Wolfire et al. 2003; Raymond et al. 1976; Myasnikov et al. 1998)

$$\Lambda(T) = \begin{cases} 4 \times 10^{-29} T^{0.8} & \text{if } 55\,\mathrm{K} \leq T < 10^4\,\mathrm{K} \\ 7 \times 10^{-27} T & \text{if } 10^4\,\mathrm{K} \leq T < 10^5\,\mathrm{K} \\ 7 \times 10^{-19} T^{-0.6} & \text{if } 10^5\,\mathrm{K} \leq T < 4 \times 10^7\,\mathrm{K} \\ 3 \times 10^{-27} T^{0.5} & \text{if } T \geq 4 \times 10^7\,\mathrm{K} \end{cases} \tag{3.42}$$

Then, the shock is classified as adiabatic if t_Λ is larger than the characteristic timescale of the system.

3.3.3.2 Magnetic amplification

As mentioned before, the magnetic turbulence at each side of the shock confines the particles and leads to their acceleration. Ahead of the shock, the turbulence is usually thought to be produced by the excitation of the Alfvénic modes in resonance with the Larmor radius of CRs. Nevertheless, the non-thermal X-emission observed

in some SNRs can be only explained if the magnetic field value is considerably above what is expected in the shocked interstellar medium (e.g. Bamba et al. 2003; Berezhko et al. 2003; Vink & Laming 2003). The amplification mechanism is not well known, but there are several proposals in the literature (see Bykov et al. 2013, for a review on plasma instabilities). Bell (2004) has suggested that the magnetic enhancement is a consequence of the non-resonant hybrid instability, also called the Bell instability. Positive currents of cosmic rays propagate upstream from the shock exciting non-resonant modes, which can grow stably up to values even far beyond the unperturbed magnetic field strength. The saturated magnetic field is usually estimated as (see e.g., Bustard et al. 2017)

$$B \approx \sqrt{4\pi P_{\rm cr}\left(\frac{V_{\rm sh}}{c}\right)} \approx \sqrt{4\pi\,\rho_0\,V_{\rm sh}^2\left(\frac{V_{\rm sh}}{c}\right)}, \tag{3.43}$$

where we assumed that the CR pressure $P_{\rm cr}$ is comparable to $\rho\,V_{\rm sh}^2$. Nevertheless, the numerical simulations show that the amplification can exceed the limit imposed by Eq. (3.43), and therefore it is thought that another type of instability should occur simultaneously. Beresnyak et al. (2009) suggested an alternative process in which the amplification is a pure result of non-linear fluid mechanisms. The basic idea is that the CRs diffusing ahead of the shock generates a pressure gradient in the upstream region, which decelerates and compresses the flow into the shock. Since the astrophysical plasmas have typically intrinsic inhomogeneities, the CR pressure affects the denser and the lighter parts of the flow differently. Consequently, a solenoidal field of velocities is created and the magnetic field becomes amplified because of the turbulent small-scale dynamo (del Valle et al. 2016).

Independent of the amplification mechanism, the saturation of the magnetic field can be approximately constrained by the equipartition between the magnetic energy density $u_{\rm B}$ and the kinetic energy density of the gas $u_{\rm g}$ (Bustard et al. 2017)

$$u_{\rm B} = u_{\rm g} \tag{3.44}$$

$$\frac{B^2}{8\pi} = \frac{9}{8}\,\rho_0\,V_{\rm sh}^2. \tag{3.45}$$

If $u_{\rm B}/u_{\rm g} > 1$, the gas becomes magnetically dominated, i.e., incompressible, and the existence of a shock is prevented (see e.g., Komissarov & Barkov 2007; Vink & Yamazaki 2014).

3.3.4 Other mechanisms

Direct acceleration of particles has been suggested to operate in sources with extremely high magnetic fields. Ruderman & Sutherland (1975) proposed that electrons dragged from the surface of a neutron star are accelerated by the electric fields induced close to the polar caps[12]. This gap acceleration has also been studied in the magnetosphere of rotating black holes (Levinson 2000). However, given the large

[12]The position of the gap is not clear and many models have been published (see e.g., Becker 2009).

magnetic field strength, these particles lose their energy very fast producing synchrotron and curvature radiation.

Another possible acceleration mechanism observed to operate in the solar corona is the magnetic reconnection. The basic idea of this mechanism consists of having converging fluxes of plasma with opposite magnetic polarization in a region with finite conductivity. In this scenario, the magnetic lines can reconnect dissipating energy which is transferred to particles (Sweet 1958; Parker 1957). Nevertheless, it has been pointed out that the rate of this process is too small to explain the solar flares. Consequently, this model was modified and magnetic turbulence was included to increase the rate of reconnection. The addition of the turbulence explains the magnetic reconnection in terms of multiple small scale reconnections (see e.g., Lazarian & Vishniac 1999). As result, the global rate of reconnection rises, and the processes become more efficient.

For UHECR, Caprioli (2015) proposed the re-acceleration of galactic CRs with energies below 10^{17} eV in relativistic jets. Particles that enter a jet with a Lorentz factor γ are boosted in energy $\sim \gamma^2$. In the case of powerful blazars, $\gamma > 30$, the resulting particles might reach energies $\sim 10^{20}$ eV

3.4 Losses

Determining the maximum energies and the particle distributions in a source require not only the acceleration of particles but also to estimate the losses. These processes are included in the terms containing $\tau_{\rm esc}$ and $b_{e,p}(E)$ of the transport equation Eq. (3.3), which limit eventually the acceleration.

3.4.1 Escape processes

Particles are removed from the source principally by diffusion and convection. These processes are related to two different scales of the motion of the particles. The diffusion has its origin at a microscopic scale by the random walk of the particles, which produces mass transport without required a bulk motion. On the other hand, convection is led by the macroscopic fluid movement, which carries the particles away.

The timescales associated with these processes are given by (Romero & Paredes 2011)

$$t_{\rm diff} = \frac{X^2}{D}, \tag{3.46}$$

$$t_{\rm conv} = \frac{X}{V}, \tag{3.47}$$

where X is the characteristic length of the region, D is the diffusion coefficient and V the fluid velocity. In scenarios like bow shocks, the fluid velocity is typical $V = V_{\rm sh}/4$. If both processes are involved in the studied situation, the characteristic escape timescale $\tau_{\rm esc}^{-1} = t_{\rm conv}^{-1} + t_{\rm diff}^{-1}$.

3.4.2 Energy losses

3.4.2.1 Ionization

O'C Drury et al. (1996) showed that the Coulomb/ionization losses suffered by the particles can suppress the DSA in very-high dense environments. For that reason, it is important to estimate the corresponding cooling times to guarantee the acceleration Schlickeiser (2002)

$$t^{e}_{\rm ion} = 1.31\times10^{8}\left(\frac{n_e}{\rm cm^{-3}}\right)^{-1}\left(\frac{E}{\rm eV}\right)\left[\ln\left(\frac{E/{\rm eV}}{n_e/{\rm cm^{-3}}}\right)+61.15\right]^{-1}\ {\rm s} \tag{3.48}$$

$$\begin{aligned} t^{p}_{\rm ion} =& 3.22\times10^{6}\,Z^{-2}\left(\frac{n_e}{\rm cm^{-3}}\right)^{-1}\left(\frac{E}{\rm eV}\right) \\ &\times\left(\frac{\beta^2}{2.34\times10^{-5}\,x_m^3+\beta^3}\right)^{-1}\Theta(\beta-7.4\times10^{-4}\,x_m)\,{\rm s}, \end{aligned} \tag{3.49}$$

where Θ is the Heaviside function, $\beta = \sqrt{1-\gamma^{-2}}$, with γ the Lorentz factor of the particle, and $x_m = (T_e/2\times10^6\,{\rm K})^{1/2}$. If these timescales are shorter than the acceleration timescale, the acceleration of particles does not take place.

3.4.2.2 Adiabatic losses

The adiabatic losses are the energy losses due to the work done by the particles expanding the shocked material. The timescale in a problem with spherical symmetry is (Longair 2011)

$$t_{\rm adi} = \frac{R}{V} = 4.9\times10^{-8}\left(\frac{V}{1000\,{\rm km\,s^{-1}}}\right)^{-1}\left(\frac{R}{\rm cm}\right)\,{\rm s}, \tag{3.50}$$

with R the outer radius of the expanding sphere and V the expansion velocity. If the adiabatic cooling is very efficient, only a small amount of the energy injected in particles can be converted to photons and radiated away.

3.4.2.3 Synchrotron radiation

Synchrotron emission is observed to be produced in many astrophysical sources such as SNRs and accreting black holes (BHs). The radiation is generated by non-thermal[13] charged particles interacting with magnetic fields. The loss rate for an ultra-relativistic particle of mass m, charge q and energy E in a region with a magnetic field B is (Longair 2011)

$$\left.\frac{dE}{dt}\right|_{\rm synch} = 2\,\sigma_{\rm T}\,c\left(\frac{m_e}{m}\right)^2\frac{B^2}{8\,\pi}\left(\frac{E}{m\,c^2}\right)^2\sin^2\alpha \tag{3.51}$$

[13]Non-thermal is used to indicate that the particles do not follow a Maxwellian energy distribution.

where $\sigma_{\rm T} = 8\,\pi\,r_e^2/3$ is the Thomson cross section, r_e the classical radius of the electron, and α the pitch angle[14]. Averaging over the value of α assuming its distribution is isotropic, the cooling timescale can be written as

$$t_{\rm sync}^{-1} = \left.\frac{dE}{dt}\right|_{\rm synch} E^{-1} = \frac{c\,\sigma_{\rm T}}{6\pi}\left(\frac{m_e}{m}\right)^3 \frac{E\,B^2}{(m_e\,c^2)\,(m\,c^2)}. \tag{3.52}$$

From Eq. (3.51), we can note that the emission is more efficient for electrons than for protons, since $(dE/dt)|_{\rm synch} \propto m^{-4}$. Therefore, in most of the cases the synchrotron emission is only significant for electrons.

One electron with energy E, charge e and mass $m_{\rm e}$, which is moving in a region with a magnetic field $\vec{B}$, produces a synchrotron radiation spectrum (Blumenthal & Gould 1970)

$$P_{\rm sync}(E, E_\gamma, \alpha) = \frac{\sqrt{3}\,e^3\,B\,\sin\alpha}{h\,m_e\,c^2}\,\frac{E_\gamma}{E_{\rm c}}\int_{E_\gamma/E_{\rm c}}^{\infty} K_{5/3}(\xi)\,d\xi, \tag{3.53}$$

with the characteristic energy

$$E_{\rm c} = \frac{3}{4\pi}\frac{e\,h\,B\,\sin\alpha}{m_e\,c}\left(\frac{E}{m_e c^2}\right)^2, \tag{3.54}$$

where $K_{5/3}(\xi)$ is the modified Bessel function. The function $x\int_x^\infty K_{5/3}(\xi)d\xi \approx 1.85\,x^{1/3}\,e^{-x}$ (see e.g., Longair 2011). Considering again the average value over the angle α, $<\sin(\alpha)>=\sqrt{2/3}$, and Eq. (3.53) can be written as

$$P_{\rm sync}(E, E_\gamma) = \frac{\sqrt{2}\,e^3\,B}{h\,m_e\,c^2}\,1.85\left(\frac{E_\gamma}{E_{\rm c}}\right)^{1/3} e^{-E_\gamma/E_{\rm c}}. \tag{3.55}$$

Using the last result, the synchrotron luminosity created by a distribution of electrons $N_{\rm e}(E)$ can be calculated as

$$L_{\rm sync}(E_\gamma) = E_\gamma\,V_{\rm X}\int_{E^e_{\rm min}}^{E^e_{\rm max}} N_e(E)\,P_{\rm sync}(E, E_\gamma)\,dE, \tag{3.56}$$

where $V_{\rm X}$ is the emitting volume and $E^e_{\rm min}$ and $E^e_{\rm max}$ are the minimum and maximum energies of the electrons, respectively. In the cases where the synchrotron self-absorption is relevant, a correction factor $\kappa_{\rm SSA}(E_\gamma)$ should be introduced multiplying the last expression. Expressions for its calculation can be found, e.g., in Rybicki & Lightman (1979) or Ghisellini (2013). This correction modifies the spectrum of photons only at short frequencies, being more important for large densities of electrons.

3.4.2.4 Inverse Compton scattering

Inverse Compton (IC) scattering is produced when a high-energy electron transfers part of its kinetic energy to a photon. This process takes place in astrophysical

[14]The angle subtended by the direction of the movement of the particle to the magnetic field vector.

environments because the accelerated particles coexist with local and global radiation fields such as infrared (IR) emission from dust, the Cosmic Microwave Background (CMB), or stellar light.

The calculation of the energy loss by IC scattering is not trivial. The analysis is usually studied in two regimes: Thomson and Klein-Nishina. Defining $x = E\,\epsilon/(m_e\,c^2)$, where E is the energy of the electron and ϵ the energy of the photon before the scattering, the cross section is approximately (Romero & Paredes 2011)

Thomson regime:

$$\sigma_{\rm IC} \approx \sigma_{\rm T}\,(1 - 2\,x) \quad \text{with } x \ll 1 \tag{3.57}$$

Klein-Nishina regime:

$$\sigma_{\rm IC} \approx \frac{3}{8}\,\sigma_{\rm T}\,x^{-1}\,\ln(4x) \quad \text{with } x \gg 1 \tag{3.58}$$

From these expressions, it can be seen that in the Thomson regime the cross section is almost constant, contrary to the Klein-Nishina regime where it decreases quickly as a consequence of quantum effects. In the Thomson regime, the scattering can be considered elastic[15], whereas in the Klein-Nishina regime not (Gaisser et al. 2016).

One important thing to keep in mind to address the study of astrophysical sources is the relation between the synchrotron and IC emission. If the IC scattering happens in the Thomson regime, then (Romero & Paredes 2011)

$$\frac{t_{\rm IC}}{t_{\rm synch}} = \frac{u_{\rm B}}{u_{\rm ph}}, \tag{3.59}$$

where $u_{\rm B}$ and $u_{\rm ph}$ are the magnetic and photon energy density, respectively. Then, comparing the energy density of the magnetic field with the radiation fields can provide information about the dominant process. The same applies if the source has many radiation fields in the Thomson regime, the radiation field with the largest energy density prevails.

If the Lorentz factor of the electron is much larger than 1, the photon is scattered in the direction of motion of the electron. Under this approximation it is possible to write the differential IC cross section in a very convenient form (Aharonian & Atoyan 1981)

$$\frac{d\sigma_{\rm IC}}{dE_\gamma} = \frac{4\,\pi\,r_e^2}{b_\theta\,E}\left[1 + \frac{z^2}{2\,(1-z)} - \frac{2\,z}{b_\theta\,(1-z)} + \frac{2\,z^2}{b_\theta^2\,(1-z)^2}\right], \tag{3.60}$$

with $z = E_\gamma/E < b_\theta/(1+b_\theta)$ and $b_\theta = 2(1-\cos\phi)\epsilon\,E/(m_e\,c^2)^2$, being E_γ the energy of the scattered photon and ϕ the angle of interaction.

Assuming now that the photons are isotropically distributed we can average over the angle ϕ, resulting in the IC timescale (Aharonian & Atoyan 1981)

$$t_{\rm IC}^{-1} = \frac{(dE/dt)|_{\rm IC}}{E} = \frac{c}{E}\int_{\epsilon_{\rm min}}^{\epsilon_{\rm max}} d\epsilon \int_{\epsilon}^{\frac{\Omega E}{1+\Omega}} dE_\gamma\,\left(E_\gamma - \epsilon\right) P_{\rm IC}(E, E_\gamma, \epsilon),\,, \tag{3.61}$$

[15] In the rest frame of reference of the electron.

where

$$P_{\rm IC}(E, E_\gamma, \epsilon) = \frac{3\,\sigma_{\rm T}\,(m_{\rm e}\,c^2)^2}{4\,E^2}\,\frac{n_{\rm ph}(\epsilon)}{\epsilon}\,F(q), \tag{3.62}$$

$$F(q) = 2\,q\,\ln(q) + (1+2\,q)(1-q) + \frac{1}{2}(1-q)\frac{(\Omega\,q)^2}{1+\Omega\,q}, \tag{3.63}$$

with

$$\Omega = \frac{4\epsilon\,E}{(m_e c^2)^2} \quad \text{and} \quad q = \frac{E_\gamma}{\Omega(E-E_\gamma)}. \tag{3.64}$$

Here $n_{\rm ph}(\epsilon)$ is the number of target photons per unit of energy and volume.

Finally, the total luminosity can be calculated as

$$L_{\rm IC}(E_\gamma) = E_\gamma^2\,V_{\rm X}\,c\int_{E^e_{\rm min}}^{E^e_{\rm max}} dE\,N_e(E)\int_{\epsilon_{\rm min}(E,E_\gamma)}^{\epsilon_{\rm max}(E,E_\gamma)} d\epsilon\,P_{\rm IC}(E,E_\gamma,\epsilon). \tag{3.65}$$

3.4.2.5 Relativistic Bremsstrahlung

The relativistic Bremsstrahlung is produced when a charged relativistic particle is decelerated by the Coulomb field of another particle, typically an atomic nucleus. Assuming a photon of energy E_γ created by the dispersion of a relativistic electron of energy E in the field of a nucleus of charge $Z\,e$, the differential cross section of the interaction is given by (e.g. Blumenthal & Gould 1970; Schlickeiser 2002)

$$\frac{d\sigma_{BS}}{dE_\gamma}(E,E_\gamma) = \frac{4\,\alpha\,r_e^2\,Z^2}{E_\gamma}\,\phi(E,E_\gamma), \tag{3.66}$$

where $\alpha \sim 1/137$ is the fine-structure constant. The function $\phi(E,E_\gamma)$ depends on the ionization state of the matter. If the atomic nucleus is completely ionized

$$\phi(E,E_\gamma) = \left[1+\left(1-\frac{E_\gamma}{E}\right)^2 - \frac{2}{3}\left(1-\frac{E_\gamma}{E}\right)\right]\times\left\{\ln\left[\frac{2\,E\,(E-E_\gamma)}{m_e\,c^2\,E_\gamma}\right]-\frac{1}{2}\right\}, \tag{3.67}$$

whereas it becomes

$$\phi(E,E_\gamma) = \left[1+\left(1-\frac{E_\gamma}{E}\right)^2 - \frac{2}{3}\left(1-\frac{E_\gamma}{E}\right)\right]\ln\left(\frac{191}{Z^{1/3}}\right)+\frac{1}{9}\left(1-\frac{E_\gamma}{E}\right). \tag{3.68}$$

if the nucleus is in its neutral form.

The cooling timescale associated with Bremsstrahlung is

$$t_{\rm BS}^{-1} = 4\,n\,Z^2\,r_e^2\,\alpha\,c\Phi(E), \tag{3.69}$$

$\Phi(E) = \ln[E/(m_e\,c^2)] + 0.36$ if the gas is ionized and $\Phi(E) = \ln(183\,Z^{-1/3}) - 1/18$ if neutral. Here, n is the number density of the medium.

The luminosity emitted by a distribution of electrons $N_e(E)$ can be obtained from

$$L_{\rm BS}(E_\gamma) = E_\gamma^2\,V_{\rm X}\int_{E_\gamma}^{E^e_{\rm max}} n\,c\,\frac{d\sigma_{\rm BS}(E,E_\gamma)}{dE_\gamma}\,N_e(E)\,dE. \tag{3.70}$$

3.4.2.6 Proton-proton inelastic collisions

The inelastic collisions of relativistic protons and the ambient gas lead the production of pions, kaons, and hyperons. These particles, in turn, decay producing gamma rays and leptons. The gamma rays are principally created as a consequence of the decay of neutral pions, originated by the following reactions (Vila & Aharonian 2009)

$$p + p \rightarrow p + p + a\,\pi^0 + b\,(\pi^+ + \pi^-) \tag{3.71}$$
$$p + p \rightarrow p + n + \pi^+ + a\,\pi^0 + b\,(\pi^+ + \pi^-) \tag{3.72}$$
$$p + p \rightarrow n + n + 2\pi^+ + a\,\pi^0 + b\,(\pi^+ + \pi^-), \tag{3.73}$$

where a and b are integer numbers. The probability of occurrence of each of these channels depends on the energy available in the interaction. For lower energy protons, the probability of creating neutral pions is higher than charged pions, whereas for high energy protons the three species of pions have almost the same chance to appear.

The main channels of pions decays are given by

$$\pi^0 \rightarrow \gamma + \gamma \tag{3.74}$$
$$\pi^+ \rightarrow \mu^+ + \nu_\mu \quad \text{with} \quad \mu^+ \rightarrow e^+ + \bar{\nu}_\mu + \nu_e \tag{3.75}$$
$$\pi^- \rightarrow \mu^- + \bar{\nu}_\mu \quad \text{with} \quad \mu^- \rightarrow e^- + \nu_\mu + \bar{\nu}_e. \tag{3.76}$$

Consequently, not only photons, but also neutrinos, electrons and positrons are created in proton-proton (pp) inelastic collisions.

The energy threshold for the neutral pion production is $E_{\rm th} \approx 1.22\,\mathrm{GeV}$. The cooling rate for pp interactions can be calculated as (Aharonian & Atoyan 1996)

$$t_{pp}^{-1} = n\,\sigma_{pp}\,f_{pp}\,c \quad , \tag{3.77}$$

where $f_{pp} \sim 0.5$ is the total inelasticity of the process[16]. We approximate the cross section σ_{pp} using the expression presented by Kelner et al. (2006)

$$\sigma_{pp}(E_p) = (34.3 + 1.88L + 0.25L^2)\left[1 - \left(\frac{E_{\rm th}}{E_p}\right)^4\right]^2 \quad \mathrm{mb}, \tag{3.78}$$

which is valid for $E_p \leq 10^5\,\mathrm{TeV}$. Here $L = \ln(E_p/1\,\mathrm{TeV})$.

The gamma luminosity generated by the decay of neutral pions π^0 created by pp collisions of relativistic protons in a distribution $N_p(E_p)$ can be estimated using the following expression (see Kelner et al. 2006; Vila & Aharonian 2009)

$$L_\gamma(E_\gamma) = V_X\,E_\gamma^2\,q_\gamma(E_\gamma), \tag{3.79}$$

with $q_\gamma(E_\gamma)$ the emissivity in units of photons per unit of energy, volume, and time.

For protons with $E_p \gtrsim 100\,\mathrm{GeV}$, the emissivity is given by

$$q_\gamma(E_\gamma) = c\,n\int_{E_\gamma}^{\infty} \sigma_{pp}(E_p)\,N_p(E_p)\,F_\gamma\left(\frac{E_\gamma}{E_p}, E_p\right)\frac{dE_p}{E_p}, \tag{3.80}$$

[16]Only one or two of the created pions carry most the kinetic energy lost by the relativistic proton (Vila & Aharonian 2009).

where $F_\gamma(E_\gamma/E_p, E_p)$ is the number of photons per unit of energy created in one collision (see Appendix B). This function includes not only the gamma-ray contribution from neutral pions, but also from η-mesons. At lower energies (i.e., $E_p < 100\,\mathrm{GeV}$), we use the δ-functional formalism approximation (Aharonian & Atoyan 2000; Kelner et al. 2006)

$$q_\gamma(E_\gamma) = 2 \int_{E_{\min}}^{E^p_{\max}} \frac{Q_{\pi^0}(E_\pi)}{\sqrt{E_\pi^2 - m_{\pi^0}^2\, c^4}} dE_\pi, \tag{3.81}$$

with

$$E_{\min} = E_\gamma + \frac{m_{\pi^0}^2 c^4}{4\,E_\gamma} \tag{3.82}$$

and

$$\begin{aligned} Q_{\pi^0}(E_\pi) &= \tilde{n}\, c\, n \int \delta(E_\pi - K_\pi E_{\mathrm{kin}})\, \sigma_{pp}(E_p)\, N_p(E_p)\, dE_p \\ &= \frac{\tilde{n}}{K_\pi}\, c\, n\, \sigma_{pp} \left(m_p\, c^2 + \frac{E_\pi}{K_\pi}\right) N_p \left(m_p\, c^2 + \frac{E_\pi}{K_\pi}\right). \end{aligned} \tag{3.83}$$

$E_{\mathrm{kin}} = E_p - m_p\, c^2$ is the kinetic energy, n and $\tilde{n}$ are the ambient density and the number of π^0 created in one interaction, respectively. The latter is obtained demanding continuity between Eq. (3.80) and Eq. (3.81) at $E_p = 100\,\mathrm{GeV}$, for $K_\pi \approx 0.17$ (Gaisser 1990; Kelner et al. 2006). In this thesis we do not present the distributions of other particles than photons created in pp interactions, but the necessary expressions can be found in Kelner et al. (2006) (see Appendix B). In astrophysical sources where the photon density is much higher than the matter density, the photohadronic interactions can be also relevant (see e.g., Dermer & Giebels 2016).

3.4.3 Absorption and electron-positron pair production

The gamma rays produced in a source can interact with the matter, magnetic and radiation fields and consequently, they can be absorbed. The attenuated luminosity can be obtained as (Romero et al. 2010)

$$L_\gamma(E_\gamma) = L^0_\gamma(E_\gamma)\, e^{-\tau(E_\gamma, s)}, \tag{3.84}$$

where $L^0_\gamma(E_\gamma)$ is the luminosity without absorption and τ is the optical depth of the medium.

In the context of this thesis, the pair creation by photon-photon interactions is important in Chapter 6. The optical depth in this process can be calculated as

$$\tau(E_\gamma, s) = \int_{E_{\min}}^{\infty} d\epsilon \int_s^\infty dr'\, n_{\mathrm{ph}}(\epsilon, r')\, \sigma_{\gamma\gamma}(\epsilon, E_\gamma), \tag{3.85}$$

where ϵ is the energy of the target photons, n_{ph} is their energy density and $\sigma_{\gamma\gamma}$ the total cross section of the interaction (see e.g., Gould & Schréder 1967)

$$\sigma_{\gamma\gamma} = \frac{\pi\, r_e^2}{2} (1 - s_0^2) \left[(3 - s_0^4)\, \ln\left(\frac{1 + s_0}{1 - s_0}\right) + 2\, s_0\, (s_0^2 - 2)\right], \tag{3.86}$$

where $s_0 = \sqrt{1 - 2\,(m_e\,c^2)^2/[E_\gamma \epsilon\,(1 - \cos\theta)]}$, with θ the angle between the directions of the photons.

The threshold condition for electron-positron pair production is $E_\gamma\,\epsilon > (m_e\,c^2)^2$. If $\epsilon \ll m_e\,c^2 \leq E_\gamma$, the injection of secondary particles $Q_e^{\rm sec}(E_e)$ (in units of erg^{-1} s^{-1} cm^{-3}) can be approximated as (Agaronyan et al. 1983; Boettcher & Schlickeiser 1997)

$$
\begin{aligned}
Q_e^{\rm sec}(E_e) = & \frac{3}{32}\frac{c\,\sigma_{\rm T}}{m_e\,c^2}\int_{\gamma_e}^{\infty} d\epsilon_\gamma\,\frac{n_\gamma(\epsilon_\gamma)}{\epsilon_\gamma^3}\int_{\frac{\epsilon_\gamma}{4\,\gamma_e\,(\epsilon_\gamma-\gamma_e)}}^{\infty} d\omega\,\frac{n_{\rm ph}(\omega)}{\omega^2} \\
& \times\left\{\frac{4\,\epsilon_\gamma^2}{\gamma_e\,(\epsilon_\gamma-\gamma_e)}\ln\left[\frac{4\,\gamma_e\,\omega\,(\epsilon_\gamma-\gamma_e)}{\epsilon_\gamma}\right] - 8\,\epsilon_\gamma\,\omega\right. \\
& \left. + \frac{2\,(2\,\epsilon_\gamma\,\omega - 1)\,\epsilon_\gamma^2}{\gamma_e\,(\epsilon_\gamma-\gamma_e)} - \left(1 - \frac{1}{\epsilon_\gamma\,\omega}\right)\frac{\epsilon_\gamma^4}{\gamma_e^2\,(\epsilon_\gamma-\gamma_e)^2}\right\},
\end{aligned}
\tag{3.87}
$$

where $\gamma_e = E_e/(m_e\,c^2)$, $\epsilon_\gamma = E_\gamma/(m_e\,c^2)$, and $\omega = \epsilon/(m_e\,c^2)$. These CRs interact and emit due to the same processes as the primary electrons do.

4

Particle acceleration in the superwind of starburst galaxies*. Part I: Large-scale processes

4.1 Introduction

As mentioned in Section 2.2.1, starburst galaxies are galaxies with high star formation rates (SFRs). The large number of core-collapse supernovae (SNe) combined with the effect of the stellar winds powered by the abundant massive stars produce a hot thermalized gas with a temperature of $\sim 10^8$ K. This temperature is large enough to allow the gas to be gravitational unbounded and to escape from the starburst region. Consequently, the outflow expands into the galactic halo, sweeping up matter of the disk. The origin of these superwinds was first clarified by Chevalier & Clegg (1985). Their model has been corroborated by observations (e.g., Heckman et al. 1990) and improved with computational simulations over the last three decades (e.g., Strickland et al. 2000; Cooper et al. 2008).

The production of cosmic rays (CRs) in galactic superwinds has been investigated by Jokipii & Morfill (1985) and Bustard et al. (2017) in the Milky Way, and by Anchordoqui et al. (1999) in the nearby starburst NGC 253. Furthermore, Lacki (2014) proposed that the extended gamma-ray bubbles (Su et al. 2010) detected by the *Fermi* satellite are the radiative signature of CRs accelerated in the termination shock of the superwind created by a past starburst episode in the central region of the Galaxy. All these models suggest that particles are accelerated by diffusive shock acceleration (DSA) in the shock produced by the large-scale outflow. Particularly, nearby starburst galaxies were proposed as sources of heavy nuclei up to $\sim 10^{20}$ eV by Anchordoqui et al. (1999). Their idea is based on the synthesis of heavy nuclei by the stars in the starburst region. These heavy elements are carried out by the outflow, turning superwinds into high-metallicity environments. Additionally, the large extension of the superbubbles enables to confine ultra-high energy particles even in the presence of weak magnetic fields, as well as the lack of photons in the galactic halos promotes that the ultra-high energy heavy nuclei do not suffer photo-disintegrations during the acceleration process.

The connection between CRs and starburst galaxies was reinforced in the last years by several experiments. On the one hand, the data collected by the Pierre Auger

[0]Contents of this chapter are already published in Romero et al. (2018) https://www.aanda.org/articles/aa/pdf/2018/08/aa32666-18.pdf.

Observatory (Auger) show that the composition of CRs becomes heavier at high energies. The data analysis done using the most recent hadronic interaction models indicates that at energies above 10 EeV protons and iron are absent or their fraction is very small (Aab et al. 2014; The Pierre Auger Collaboration et al. 2017). Therefore, CRs at such energies might come from high-metallicity astrophysical environments. In contrast, the results found by the Telescope Array Project (TA) using the hadronic interaction models developed before the Large Hadron Collider (LHC) measurements support a proton dominated composition, nonetheless the sensitivity of this experiment is not large enough to distinguish between protons and intermediate-mass nuclei of the same energy. The joint analysis made by Auger and TA actually shows that the composition obtained by both experiments is consistent within the estimated errors (Abbasi et al. 2016). Semikoz et al. (2016) suggested that data seem to point out that the composition of CRs with energies above 40 EeV is dominated by intermediate-mass nuclei (e.g., oxygen, nitrogen, etc.), whose deflections are large enough to prevent the correlation between arrival direction and source position. Nevertheless, the analysis made by Auger for CRs with energies greater than 38 EeV at an angular scale of 15° denotes a 4.5σ significance for starburst galaxies (Aab et al. 2017, 2018; The Pierre Auger Collaboration et al. 2019).

On the other hand, the *Fermi* satellite has detected eight starburst galaxies (Ballet et al. 2020). In particular, the nearby starbursts M82 and NGC 253 are gamma-ray emitters also measured by ground-based Cherenkov observatories (Acciari et al. 2009; Abdo et al. 2010). The observed radiation can be explained invoking a density of CRs hundreds of times higher than in the Milky Way. A large amount of CRs is expected to be produced because of the very high supernova rate in starbursts. The gamma emission is presumed to originate in the interaction of relativistic hadrons with the ambient gas (e.g, Paglione et al. 1996; Domingo-Santamaría & Torres 2005; Ohm 2016). A possible correlation between gamma rays and neutrino candidate events in the energy range from 30 to 2000 TeV has been reported by IceCube (Aartsen et al. 2014). In spite of the discussions conducted by Chang & Wang (2014); Chang et al. (2015), and Anchordoqui et al. (2014), the relation between starbursts and cosmic neutrinos is still being debated (Bechtol et al. 2017).

In this chapter, we revisit the model proposed by Anchordoqui et al. (1999) using the observational information of NGC 253 obtained by different experiments over the last twenty years. We perform a detailed analysis of the effects of the cooling and escape of the relativistic particles. Furthermore, we evaluate the efficiency of stochastic diffusive acceleration (SDA) in the turbulent superbubble for the first time.

4.2 Basic model

4.2.1 Superwind

The basic superwind model was developed by Chevalier & Clegg (1985) and improved over the years by several other authors (e.g., Heckman et al. 1990; Strickland et al. 2002). Superwinds are created as a consequence of the supernova ejecta and stellar winds in the nuclear region of the starburst. When the gas in this region is efficiently thermalized, it reaches a temperature $T \sim 10^8$ K and a high pressure. Consequently, the hot gas bubble expands removing the interstellar matter in its path until it reaches the

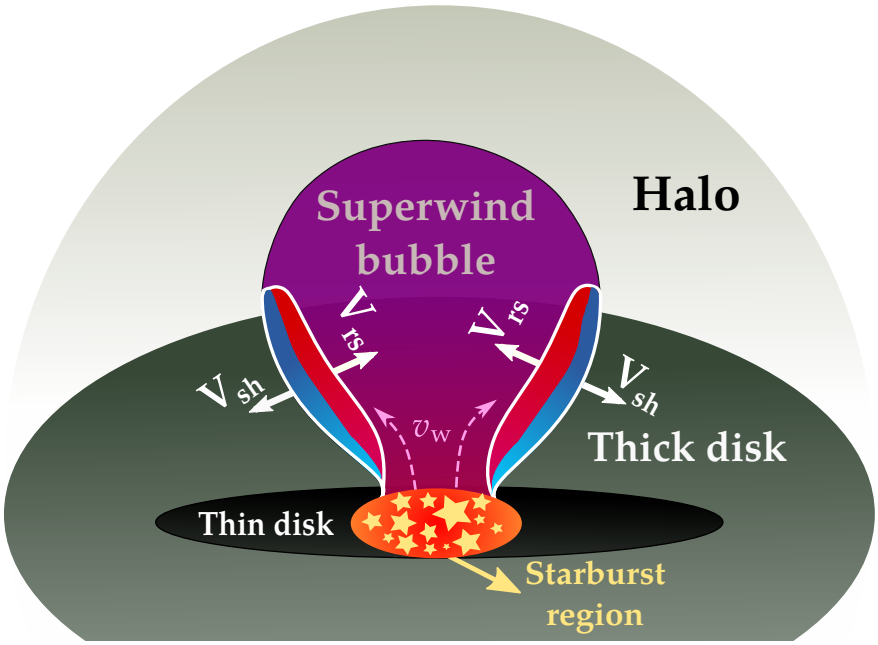

Figure 4.1: Scheme of the physical scenario considered in this chapter (not to scale), adapted from Strickland et al. (2002).

galactic disk edge. The disk is then disrupted by the bubble and the hot gas escapes into the galactic halo sweeping up cooler denser matter from the disk. The result is a multi-phased superbubble expanding adiabatically, whose velocity becomes rapidly

$$v_\infty \sim \sqrt{2\dot{E}/\dot{M}} \sim 10^3 \,\mathrm{km\,s^{-1}}, \tag{4.1}$$

where $\dot{E}$ is the total energy injected and $\dot{M}$ is the mass input.

The wind is typically bipolar. The swept-up matter from the galactic disk accumulates around the bubble cavity. The interaction of this cold, dense matter with the supersonic wind produces shock waves (see e.g., Strickland et al. 2000), as mentioned in Section 3.3.3.1. Since the surrounding matter is much denser than the wind gas, the forward shock is slow and reaches velocities of only several hundreds of $\mathrm{km\,s^{-1}}$. This shocked gas becomes radiative and forms walls of $T \sim 10^4$ K at the sides of the superbubble. Figure 4.1 shows a sketch of the situation here described.

4.2.2 Scaling relations

The total energy released by the superwind $\dot{E}$ and the mass injected $\dot{M}$ are directly related with the number of SN explosions and the input of the stellar winds in the starburst region. The constants of proportionality between the values of these quantities in the starburst and the superwind are the thermalization efficiency ϵ and the mass loading factor β. In terms of these parameters, the total energy injected by the superwind and its mass input can be written as (see e.g., Veilleux et al. 2005; Tanner et al. 2017)

$$\dot{E} = \epsilon \, \dot{E}_\star \tag{4.2}$$

$$\dot{M} = \dot{M}_\star + \dot{M}_{\rm ISM} = \beta\ \dot{M}_\star \tag{4.3}$$

where the $\star$ denotes the values in the starburst region. As described by Eq. (4.3), the superwind carries not only the mass contribution of the SNe and the stellar winds, but also swept-up interstellar matter. Therefore, β is typically a value larger than one (Tanner et al. 2017). On the contrary, since ϵ represents the fraction of energy transfered from the starburst to the outflow, its value is equal to one at most.

The SFR sets the properties of the starburst region. All the processes occurring there depend on it and consequently, the starburst parameters scale with the SFR as follows (Veilleux et al. 2005)

$$\dot{E}_\star = 7 \times 10^{41}\ ({\rm SFR}/{\rm M_\odot\,yr^{-1}})\ \ {\rm erg\,s^{-1}}, \tag{4.4}$$

$$\dot{M}_\star = 0.26\ ({\rm SFR}/{\rm M_\odot\,yr^{-1}})\ \ {\rm M_\odot\,yr^{-1}}. \tag{4.5}$$

The supernova rate and the SFR are also related:

$$\dot{\tau}_{\rm SN} = 0.02\ ({\rm SFR}/{\rm M_\odot\,yr^{-1}})\ \ {\rm yr^{-1}}. \tag{4.6}$$

Assuming that the dust is primarily heated by the young stars present in the starburst region, the SFR can be inferred from the total infrared (IR) luminosity observed from 8 to 1000 µm (Kennicutt 1998a)

$${\rm SFR} \approx 17\ \frac{L_{\rm IR}}{10^{11}\,{\rm L_\odot}}\ \ {\rm M_\odot\,yr^{-1}}. \tag{4.7}$$

Finally, the terminal velocity of the superwind becomes independent of the SFR and can be written only in terms of ϵ and β

$$v_\infty = \sqrt{\frac{2\epsilon\dot{E}_\star}{\beta\dot{M}_\star}} \approx 3000\sqrt{\frac{\epsilon}{\beta}}\ {\rm km\,s^{-1}}. \tag{4.8}$$

The gas temperature in the starburst region is given by

$$T = 0.4\mu m_H\ \frac{\dot{E}}{k_B\ \dot{M}}\ {\rm K}, \tag{4.9}$$

where k_B is the Boltzmann constant, m_H is the mass of a hydrogen atom, and $\mu = 1.4$. Replacing $\dot{E}$ and $\dot{M}$ for Eq. (4.4) and Eq. (4.5), the latter expression results in

$$T = 0.4\ \mu\ m_H\ \frac{\dot{E}}{k_B\ \dot{M}}\ {\rm K} \approx 3 \times 10^8\ \frac{\epsilon}{\beta}\ \ {\rm K}. \tag{4.10}$$

4.2.3 Dynamical conditions

As consequence of the dense medium around the superbubble, the outer shell moves with a speed $v_{\rm shell}$ smaller than v_∞. Taking convenient units (e.g., Veilleux et al. 2005)

$$v_{\rm shell} \approx 670\ \left[\frac{\epsilon\ (\dot{E}_\star/{\rm erg\,s^{-1}})}{(n_{\rm s}/{\rm cm^{-3}})\ 10^{44}\,{\rm erg\,s^{-1}}}\right]^{1/3} R_{\rm kpc}^{-2/3}\ {\rm km\,s^{-1}}. \tag{4.11}$$

In this expression $R_{\rm kpc}$ represents the radius of the superwind buble in units of kpc and $n_{\rm s}$ the ambient particle density in front of the shock.

The dynamical age of the wind can be deduced easily from the bubble size and the terminal velocity if we assume that the expansion velocity is almost constant in time

$$t_{\rm dyn} \sim 6 \left(\frac{v_\infty}{1000\,{\rm km\,s^{-1}}} \right)^{-1} {\rm Myr}. \tag{4.12}$$

Using 10^3 km s^{-1} as typically value for v_∞ (see Eq. (5.1)), the dynamical age turns out to be $t_{\rm dyn} \sim 6$ Myr.

Superwinds are commonly detected emitting thermal X-rays (see e.g., Zhang 2018). The derived outflow temperature is $\sim 10^6$ K and the associated cooling time $t_X \sim 77 \eta_X^{1/2} \mathcal{R}^{1/2}$ Myr, where η_X is the filling factor, and $\mathcal{R}$= $0.03/Z_{O,\,\rm true}$ the metallicity. The value of $\eta_X \sim 1$, whereas Strickland et al. (2002) estimate that $Z_{O,\,\rm true} \sim 0.5$ in NGC 253. The cooling time becomes then $t_X \sim 19$ Myr, which is much longer than the deduced $t_{\rm dyn}$, i.e., the radiative cooling is negligible and the outflow expands adiabatically. For example, the time needed to cool down from the typically wind temperature $3{\times}10^6$ K to the temperature of the H_α emitting gas 10^4 K is given by $t \sim 3{\times}10^5\,(n/{\rm cm^{-3}})^{-1}$ yr, which means for $n \sim 10^{-3}$ cm^{-3} that $t \sim 100$ Myr (Strickland et al. 2002).

The interaction of the superwind with the ambient gas produces not only the slow radiative forward shock, but also a fast adiabatic reverse shock propagating through the wind. For the characteristic temperatures derived from the X-ray observations, $c_{\rm s}{\sim}100$ km s^{-1} and the related Mach number ~ 10 (see Eq. (3.36)). The reverse shock satisfies then all the conditions to accelerate particles efficiently. Between the shocked wind matter and the shocked swept-up disk medium a contact discontinuity is established (see Section 3.3.3.1). As can be seen in Fig. 4.1, the superwind layers, from the inner to the outer, are: i) the low density hot gas, ii) the shocked wind, iii) the shocked swept-up disk material, and iv) the cool dense unperturbed medium. In the outer shell, the dense gas cools down to temperatures of 10^4 K, producing the H_α emission observed around superwind bubbles. Radiative shocks are not efficient particle accelerators, as we have discussed in Section 3.3.3.1, and hence we will not focus on the forward shock anymore.

In the next section, we will characterize the observed outflow in NGC 253 and investigate the acceleration of particles there.

4.3 NGC 253

NGC 253 is the brightest spiral galaxy in the Sculptor Group, which is located in the southern celestial hemisphere. This object, discovered by Caroline Herschel in 1783, is seen edge-on and has an estimated distance between 2.6 and 3.9 Mpc (Turner & Ho 1985; Puche & Carignan 1988; Karachentsev et al. 2003; Rekola et al. 2005). For the following analysis, we adopt the most widely distance of 2.6 Mpc (see e.g., Strickland et al. 2002; Abramowski et al. 2012). Nevertheless, to consider another value in that range do not change significantly the conclusions here presented.

Together with M82, NGC 253 is the best studied starburst galaxy. Actually, both galaxies are extremely similar and the results for one of them can easily be extrapo-

lated to the other one. Over many years, the origin of the starburst activity in NGC 253 was not clear, because no evidence of a tidal interaction with another galaxy was detected (Davidge 2010). In 2016, Romanowsky et al. found finally a disrupting dwarf galaxy, denominated NGC 253-dw2, which has probably triggered the intense star-forming episode. NGC 253 has been studied over the whole electromagnetic spectrum. Its emission covers from radio to high-energy gamma rays. In the context of this thesis, NGC 253 becomes particularly interesting because it is included in the sample considered by Auger for CR anisotropy studies (The Pierre Auger Collaboration et al. 2019). The observational evidence leaves not doubts about the presence of a superwind in this galaxy. Observations taken with *ROSAT* and the *Chandra* satellite show diffuse X-ray emission from the galactic halo, corresponding to a gas temperature of $3{\times}10^6$ K (Strickland et al. 2002). In particular, the emission in the northern halo is detected in a region surrounded by a shell emitting in H_α. The outflow extension from the galactic disk is found to be ~10 kpc.

Radovich et al. (2001) measured an integrated IR luminosity of $L_{\rm IR}$ =$1.7{\times}10^{10}$ $L_\odot$ for NGC 253. Consequently, the SFR obtained using Eq. (4.7) is $\mathrm{SFR}_{\rm NGC\,253}{\sim}3\,M_\odot\,\mathrm{yr}^{-1}$. As discussed in the previous section, the SFR allows to fix all the other relevant parameters, then from Eq. (4.4)-Eq. (4.6)

$$\dot{E} = 2\times10^{42}\ \epsilon\ \ \mathrm{erg\,s^{-1}} \tag{4.13}$$

$$\dot{M} = 0.75\ \beta\ M_\odot\,\mathrm{yr}^{-1} \tag{4.14}$$

$$\dot{\tau}_{\rm SN} = 0.058\ \ \mathrm{yr}^{-1}. \tag{4.15}$$

Recently, observations of ^{12}CO $j = 1-0$ transition lines performed with the Atacama Large Millimeter Array (ALMA) enabled to determine the mass load of the NGC 253 superwind (Bolatto et al. 2013). The total molecular mass outflow rate derived is $\dot{M}_{\rm NGC\,253} \approx 9\,M_\odot\,\mathrm{yr}^{-1}$, which implies that the wind removes such a large amount of gas from the starburst region that the star-forming activity is suppressed. From Eq. (4.14), the mass loading factor becomes $\beta \approx 12$. For M82, the thermalization efficiency ϵ is estimated to be $0.3-1$ (Strickland & Heckman 2009). Assuming $\epsilon = 0.75$, $\dot{E}_{\rm NGC\,253} = 1.5{\times}10^{42}\,\mathrm{erg\,s^{-1}}$ (see Eq. (4.13)). In the same way, the temperature in the central starburst can be calculated from Eq. (4.10), obtaining a value of ~$2{\times}10^7$ K.

The physical parameters of the superbubble can be inferred from the X-ray observations (Strickland et al. 2002). The integrated luminosity in this energy range is ~$5{\times}10^{38}\,\mathrm{erg\,s^{-1}}$ and the plasma temperature $3{\times}10^6$ K, the latter indicates a sound speed $c_{\rm s} \approx 164\,\mathrm{km\,s^{-1}}$. The outflow geometry in the halo is approximately a sphere of radius $R_{\rm b} = 5$ kpc. The average plasma density in the inflated bubble is $n \sim 2{\times}10^{-3}\,\mathrm{cm^{-3}}$, whereas ahead of the shock is $n_{\rm s} \sim 6.8{\times}10^{-3}\,\mathrm{cm^{-3}}$ (Strickland et al. 2002). The velocities of the shocks are $v_{\rm rev} \approx 750\,\mathrm{km\,s^{-1}}$ and $v_{\rm shell} \approx 298\,\mathrm{km\,s^{-1}}$ for the reverse and forward shock, respectively. If the thermalization is roughly one, these velocities become $v_{\rm rev} \approx 866\,\mathrm{km\,s^{-1}}$ and $v_{\rm shell} \approx 328\,\mathrm{km\,s^{-1}}$. Hereafter we will produce the results corresponding to these two thermalization values: $\epsilon = 0.75$ and $\epsilon = 1$.

Radio observations of the halo of NGC 253 at different frequencies reveal the presence of polarized non-thermal emission (Heesen et al. 2009b). This emission is attributed to relativistic electrons moving in the magnetic field of the galactic halo, which produce synchrotron radiation. The magnetic field estimated by Heesen et al. (2009b) from the observational data is ~5 μG, which means that the magnetic energy density in the superwind region is ~1 eV cm^{-3}. Considering that the medium is mainly composed by hydrogen, the Alfvén velocity is $v_A = B/\sqrt{4\,\pi\,\rho} \sim 240\,\mathrm{km\,s^{-1}}$. Furthermore, the transport of accelerated particles from the disk to the northern halo is observed to be led by convection, whereas in the south seems to be diffusion dominated. The velocity of the outflow derived in the northern halo is ~300 km s^{-1}, while the southern wind diffusion coefficient is $D \sim 2{\times}10^{29}$ cm s^{-1}.

NGC 253 is one of the several star-forming galaxies detected by the *Fermi* satellite, and one of the two also reported by the High Energy Stereoscopic System (H.E.S.S.) emitting at TeV energies (Acero et al. 2009; Abdo et al. 2010). For a distance of 2.6 Mpc, the integrated luminosity between 0.1 GeV and 3 TeV inferred from the combined *Fermi*-H.E.S.S. analysis is $6.6{\times}10^{39}$ erg s^{-1} (H. E. S. S. Collaboration et al. 2018). Most of the models proposed in previous works suggest that this radiation comes from the CRs accelerated by the supernova remnants (SNRs) in the starburst region (Domingo-Santamaría & Torres 2005; Rephaeli et al. 2010; Abramowski et al. 2012; Peretti et al. 2019), but since the gamma-ray region is not spatially resolved, other sources, e.g., the superwind, cannot be excluded. All the parameters previously mentioned are summarized in Table 4.1

4.4 Particle acceleration and losses

For all of the above mentioned, superwinds are potential CR sources. In this section, we will discuss this possibility and the maximum energies that the particles can reach in a galactic outflow characterized by the parameters of the northern bubble of NGC 253.

4.4.1 Acceleration conditions

The first theoretical constraint to the maximum energy of the accelerated particles is given by the Hillas criterion (Section 3.1). In the context here studied, the maximum Larmor radius that particles can have before they escape from the acceleration region is the superbubble radius $R_b = 5$ kpc. Using the magnetic field of 5 μG deduced from the observations (see Table 4.1), the maximum energies are given by

$$E_{max} = 10^{18}\,Z\,\frac{R_b}{\mathrm{kpc}}\left(\frac{B}{\mu\mathrm{G}}\right)\ \mathrm{eV} \sim 2.5\times10^{19}\,Z\ \ \mathrm{eV}, \tag{4.16}$$

which sets

$$E^{p}_{max} = 2.5\times10^{19}\ \mathrm{eV} \quad \text{protons}, \tag{4.17}$$

$$E^{Fe}_{max} = 6.5\times10^{20}\ \mathrm{eV} \quad \text{iron nuclei}. \tag{4.18}$$

Nevertheless, as we discussed in Chapter 3, the greater energies are actually limited by many other factors and the Hillas value is commonly not reached. In the following

Table 4.1: Physical properties of NGC 253 and its superwind.

Starburst parameters	Value	
d: Distance [Mpc]	$2.6^{\dagger}$– 3.9	
$L_{\rm IR}$: Infrared luminosity [$L_\odot$]	1.7×10^{10}	
SFR: Star-forming rate [$M_\odot$ yr^{-1}]	3	
β: Mass loading factor	12	
$\dot{M}$: Mass outflow [$M_\odot$ yr^{-1}]	9	
$L_\gamma(0.1\,\mathrm{GeV} - 3\,\mathrm{TeV})$: gamma-ray luminosity [erg s^{-1}]	6.6×10^{39}	
$T_{\rm c}$: Temperature of the central region [K]‡	2×10^7	
SW region parameters	**Value**	
$R_{\rm b}$: Radius of the SW bubble [kpc]	5	
$L_{\rm x}$: X-ray luminosity [erg s^{-1}]	5×10^{38}	
$T_{\rm bubble}$: Temperature of the gas in the bubble [K]	3×10^6	
n: Particle density [cm^{-3}]	2×10^{-3}	
B: Magnetic field [μG]	5	
$v_{\rm A}$: Alfvén velocity [km s^{-1}]	240	
$v_{\rm s}$: Sound speed [km s^{-1}]	164	
Parameter	Thermalization	
	$\epsilon = 1$	$\epsilon = 0.75$
$\dot{E}$: Mechanical luminosity of the superwind [erg s^{-1}]	1.5×10^{42}	1.1×10^{42}
$v_{\rm rev}$: Velocity of the reverse shock [km s^{-1}]	866	750
$v_{\rm shell}$: Velocity of the expanding shell [km s^{-1}]	328	298
$c_{\rm s}$: Sound speed in the hot central cavity [km s^{-1}]	474	425

† The value adopted in this analysis.
‡ Temperature estimated with Eq. (4.10) adopting $\beta = 12$ and $\epsilon = 0.75$.

sections we will evaluate two acceleration mechanisms that can operate in superwind bubbles.

4.4.2 Stochastic Diffusive Acceleration

As presented in Section 3.3.2, SDA can take place in turbulent media. The polarimetry radio data shows that the magnetic field in the superbubble cavity seems to be highly chaotic, presenting fluctuations of the order of $\delta B \sim B_0$ (Heesen et al. 2009b). From a theoretical point of view, it is possible to estimate the degree of turbulence calculating the Reynolds number Re. Assuming the diffusion coefficient to be $D \sim 10^{29}$ cm^2 s^{-1} (Heesen et al. 2009a) we get $Re \sim 12$ using Eq. (3.15), which indicates that fluctuations are expected and SDA can operate in the bubble plasma.

Using the value for the Alfvén velocity $v_{\rm A} = 240\,\mathrm{km\,s^{-1}}$ presented in Table 4.1, $\delta B^2 \sim B_0^2$, and assuming that the Larmor radius is $R_{\rm b} = 5\,\mathrm{kpc}$, the corresponding acceleration timescale results in $t_{\rm acc}^{\rm SDA} \sim 2.5{\times}10^{10}\,\mathrm{yr}$ (see Eq. (3.19)). This value is

almost twice the Hubble time[1], and consequently, particles with the highest energies allowed by the Hillas criterion cannot be produced by SDA.

The lifetime of the starburst activity is typically short compared with the age of the galaxy. The star formation is so intense and consumes too much gas that it cannot be sustained during long periods of time. The age of the superwind can be then estimated with Eq. (4.12). Using the expansion velocities in Table 4.1, we get that for both thermalization values, $\epsilon = 0.75$ and $\epsilon = 1$, the age is $\tau \sim 10^7$ yr. If there are no other losses involved, the source age limits the maximum energy of the particles. Equaling both timescales $t_{\rm acc} = \tau$, the maximum Larmor radius reached by the particles can be deduced, and from it, the associated maximum energies. Following this procedure, we get

$$E^{p}_{\rm max} = 1.5 \times 10^{16} \ \ {\rm eV} \quad \text{protons}, \tag{4.19}$$

$$E^{\rm Fe}_{\rm max} = 4.0 \times 10^{17} \ \ {\rm eV} \quad \text{iron nuclei}. \tag{4.20}$$

As we can see, these energies are much smaller than the values yielded by the Hillas criterion. In particular, we will see in Section 3.4 that these results can be even more constrained.

The energy in the turbulent inflated bubble is given by

$$L_{\rm turb} \sim \frac{B^2}{8\pi} v_{\rm A} (4\pi R_{\rm b}^2) \sim 6.7{\times}10^{40}\,{\rm erg\,s^{-1}}. \tag{4.21}$$

Of this luminosity, only a fraction ζ will actually go to CRs: $L_{\rm CR} = \zeta\, L_{\rm turb}$. We will set the value of $\zeta = 0.1$, resulting $L_{\rm CR} \sim 6.7{\times}10^{39}\,{\rm erg\,s^{-1}}$.

4.4.3 Diffusive Shock Acceleration

The importance of the thermal cooling in the shocks created by the interaction of the galactic outflow in NGC 253 can be quantify using Eqs. (3.40)–(3.39). The results obtained evaluating these expressions with the parameters of NGC 253 (Table 4.1) are shown in Table 4.2. Remembering that the age of the superwind is $\sim 10^7$ yr, it can be seen that, in effect, the forward shock is radiative, whereas the reverse shock is adiabatic. Additionally, the Mach numbers in both thermalization cases are larger than $\sqrt{5}$ for the reverse shock, i.e., the reverse shock is strong. Under these conditions of a adiabatic, strong and super-Alfvénic shock, the DSA can operate.

Assuming that the diffusion proceeds in the Bohm regime and adopting B =5 µG, the DSA timescale (Eq. (3.26)) becomes

$$t_{\rm acc} \approx 5.6 \times 10^{-1} \left(\frac{E}{\rm GeV}\right) \ \ {\rm yr} \ \ \text{for } \epsilon = 1 \tag{4.22}$$

$$t_{\rm acc} \approx 7.5 \times 10^{-1} \left(\frac{E}{\rm GeV}\right) \ \ {\rm yr} \ \ \text{for } \epsilon = 0.75. \tag{4.23}$$

In this cases, if we equal the lifetime of the source to Eq. (4.22) and Eq. (4.23), the maximum energies obtained are

[1]The Hubble time is defined as the inverse of the Hubble constant $H_0^{-1} \sim 1.44{\times}10^{10}$ yr.

Table 4.2: Parameters for the forward and reverse shocks.

Parameters	$\epsilon = 1$	
	Forward shock	Reverse shock
v [km s^{-1}]	328	866
μ	0.60	0.60
$T_{\rm ps}$ [K]	1.2×10^6	8.20×10^6
n [cm^{-3}]	6.83×10^{-3}	2×10^{-3}
$t_{\rm th}$ [yr]	3×10^6	2.24×10^8
M	2.0	5.3
Parameters	$\epsilon = 0.75$	
	Forward shock	Reverse shock
v [km s^{-1}]	298	750
μ	0.60	0.60
$T_{\rm ps}$ [K]	10^6	6.10×10^6
n [cm^{-3}]	6.83×10^{-3}	2×10^{-3}
$t_{\rm th}$ [yr]	2.16×10^6	1.40×10^8
M	1.8	4.6

With $\epsilon = 1$:

$$E^p_{\rm max} = 1.7 \times 10^{16} \ \text{eV} \ \text{ for protons}, \quad E^{\rm Fe}_{\rm max} = 4.4 \times 10^{17} \ \text{eV} \ \text{ for iron nuclei} \tag{4.24}$$

With $\epsilon = 0.75$:

$$E^p_{\rm max} = 1.2 \times 10^{16} \ \text{eV} \ \text{ for protons}, \quad E^{\rm Fe}_{\rm max} = 3.1 \times 10^{17} \ \text{eV} \ \text{ for iron nuclei}. \tag{4.25}$$

The power available to accelerate particles by DSA is given by

$$L_{\rm CR} = 4\pi\xi R_{\rm b}^2 \rho v_{\rm shock}^3 \sim \xi \dot{M} v_{\rm shock}^2. \tag{4.26}$$

In this expression, ξ indicates the fraction of the energy actually goes to CR (equivalent to ζ in Eq. (4.21)). Taking $\xi = 0.1$ and $v_{\rm shock} = 750\,{\rm km\,s^{-1}}$, $L_{\rm CR} \sim 3.2{\times}10^{41}\,{\rm erg\,s^{-1}}$. Nevertheless, since the accelerated particles produce, in turn, non-thermal radiation, whose luminosity cannot be larger than the luminosity injected in particles, the value of ξ should be restricted by the astronomical observations (see Section 4.5.1).

4.4.4 Losses and maximum energies

The particles being accelerated suffer, at the same time, radiative and spatial losses. More accurate values for the maximum energies can be then calculated accounting for all the processes and searching for the balance point. All the necessary expressions for the following analysis can be found in Section 3.4.

The non-radiative losses considered for both electrons and protons are ionization and adiabatic cooling, as well as the escape due to diffusion. In the particular case of the electrons, we examine the losses produced by synchrotron radiation,

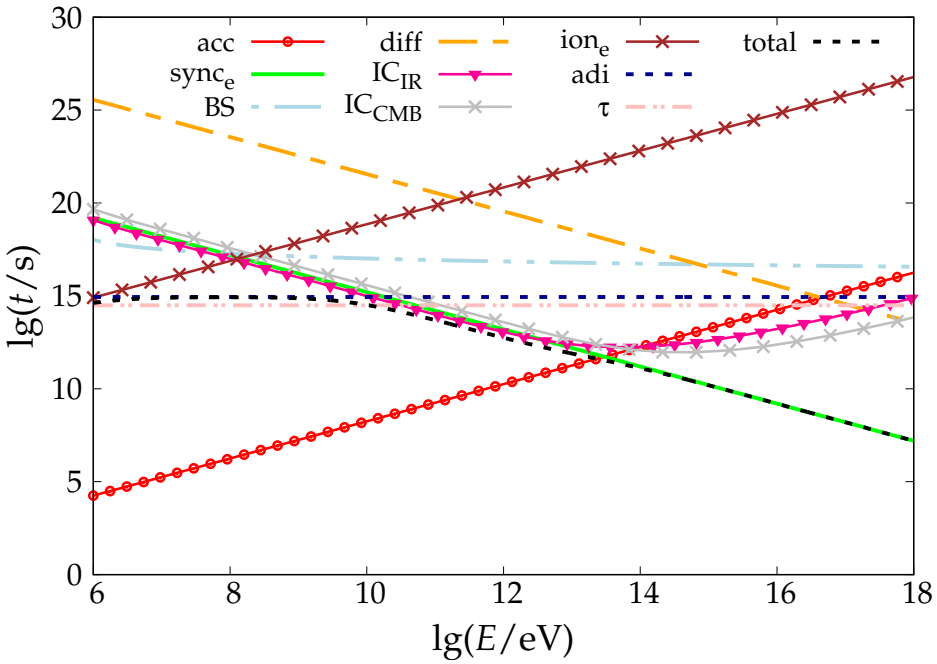

Figure 4.2: Acceleration and cooling timescales for the electrons in a 5 μG magnetic field with a thermalization $\epsilon = 1$. The result for $\epsilon = 0.75$ is the same, being only the acceleration and convection slightly slower because of the smaller shock velocity.

relativistic Bremsstrahlung, and the inverse Compton (IC) up-scattering of the IR photons coming from the central starburst region as well as the Cosmic Microwave Background (CMB) photons. The energy densities of the IC target photon fields are $u_{\rm IR} \approx 1\,{\rm eV\,cm^{-3}}$ for the IR radiation field, and $u_{\rm CMB} = 0.25\,{\rm eV\,cm^{-3}}$ for the CMB. Consequently, the IR radiation dominates the IC up-scatterings. Moreover, the magnetic energy density is also $u_{\rm mag} = B^2/(8\,\pi) \sim 1\,{\rm eV\,cm^{-3}}$. Therefore, $t_{\rm syn} \sim t_{\rm IC}$ in the Thomson regime and the maximum energy can be obtained equaling $t_{\rm acc}^{-1} = t_{\rm syn}^{-1} + t_{\rm IC}^{-1} \sim 2/t_{\rm syn}$ (see Fig. 4.2). For DSA, the maximum electron energies are $E^e_{\rm max} \approx 35\,{\rm TeV}$ ($\epsilon = 1$) and 30 TeV ($\epsilon = 0.75$). For SDA, the maximum energy reached by the electrons is much smaller $E^e_{\rm max} \approx 17\,{\rm TeV}$, because the acceleration process is slower.

For protons, in a wind with the characteristics of NGC 253, the radiative losses due to photon-pion production becomes negligible, whereas the timescale of the pp inelastic collisions is also much longer than the age of the source (see Fig. 4.3). Therefore, the maximum energy for protons remains the value estimated in the previous sections (see Eqs. (4.19)–(4.20) and Eqs. (4.24)–(4.25)).

4.4.5 Particle distributions

The distribution of the particles accelerated in the superwind can be obtained solving the transport equation (see Eq. (3.3)). The losses taken into account are the same discussed in the previous section. In the case of SDA the diffusion coefficient is the corresponding to the turbulent bubble. The origin of the turbulence is unknown,

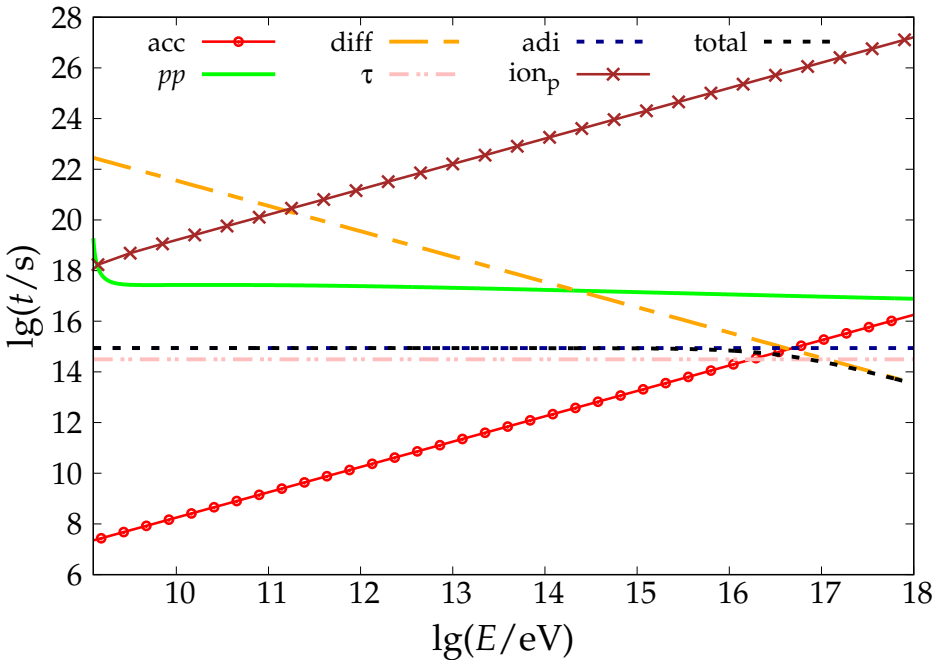

Figure 4.3: Acceleration and cooling timescales for the protons in a 5 μG magnetic field with a thermalization $\epsilon = 1$. The result for $\epsilon = 0.75$ is the same, being only the acceleration and convection slightly slower because of the smaller shock velocity.

therefore we adopt a general energy coefficient given by (see e.g., Asano & Mészáros 2016)

$$K(E) = K_0 E^q, \tag{4.27}$$

with $q = 1$. This value sets the most optimistic acceleration case, where the diffusion coefficient is directly proportional to the particle energy[2]. In situations where the Alfvén waves are the scatter centers, the magnetohydrodynamical simulations find that the index q is actually very close to the unit (see e.g., Kowal & Lazarian 2010). The constant K_0 can be calculated requiring that $K_0 \sim E\, t_{\rm acc}^{-1}$, where $t_{\rm acc}$ corresponds to SDA. Hence, $K(E)$ becomes

$$K(E) = 7.4 \times 10^{-14} \left(\frac{E}{\rm GeV}\right) \ {\rm erg^2\ s^{-1}}. \tag{4.28}$$

The equation Eq. (3.20) can be solved numerically as mentioned in Section 3.3.3 with the methods proposed by Park & Petrosian (1996). Particularly, we use the Chang-Cooper method (see Appendix A.3; Chang & Cooper 1970). As initial particle distribution we adopt the thermal distribution from the gas, i.e., a Maxwell-Boltzmann energy distribution with $T = 3{\times}10^6$ K, whose normalization is given by Eq. (4.21).

How the energy injected into particles is distributed between electrons and protons is unknown. Therefore, we study two cases: i) power equally distributed between protons and electrons ($L_p/L_e = 1$), and ii) hundred times the luminosity in electrons to protons ($L_p/L_e = 100$), as it is measured in the solar neighborhood.

[2]This is the SDA analogous to DSA in the Bohm regime.

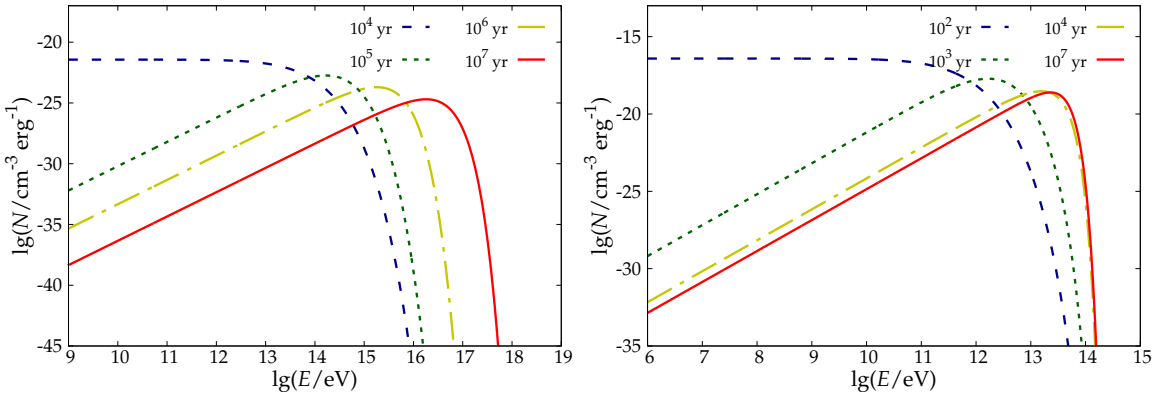

Figure 4.4: Distributions for $L_p/L_e = 1$ in the case of SDA for different times. *Left panel:* Protons. *Right panel:* Electrons.

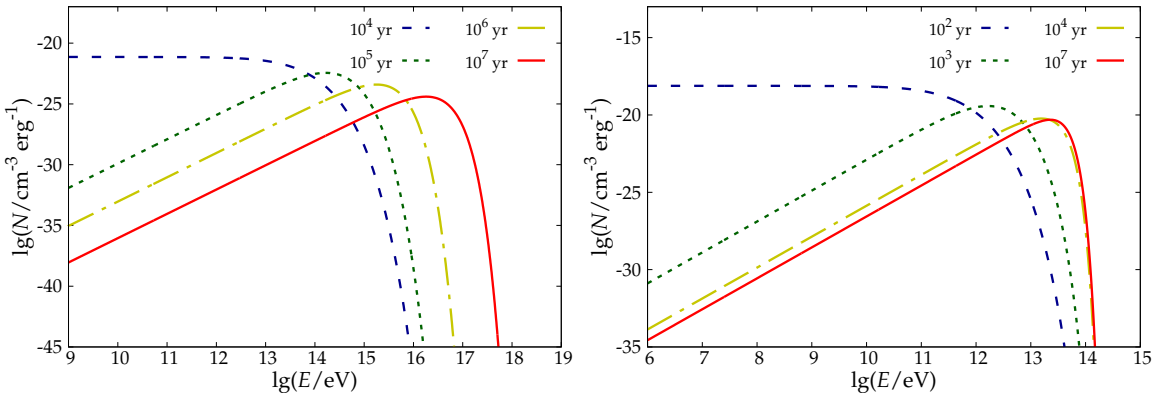

Figure 4.5: Distributions for $L_p/L_e = 100$ in the case of SDA for different times. *Left panel:* Protons. *Right panel:* Electrons.

Figure 4.4 and Fig. 4.5 show the distribution of protons and electrons at different times for $L_p/L_e = 1$ and $L_p/L_e = 100$, respectively. It can be seen that after 10^4 yr the electron distribution becomes steady. This arises from the fast equating between the cooling and the acceleration rates, produced by IC and synchrotron processes. On the contrary, since the hadronic losses are not significant, the protons do not reach the steady state and the cut-off of the distribution is yielded only by the age of the accelerator.

In the case of DSA, we adopt a constant injection given by a power-law with an exponential cut-off $Q_{e,p}(E) = Q_0^{e,p} E^{-\Gamma} \exp(-E/E_{\rm max}^{e,p})$ with $\Gamma = 2.2$, as typically deduced from the gamma emission of starburst galaxies (Ackermann et al. 2012b; Ajello et al. 2020). The transport equation takes the form provided in Eq. (3.4). Since the spatial escape of particles is only possible due to diffusion, $t_{\rm esc} = t_{\rm diff} = R^2/D(E)$. The diffusion at the shock is assumed to occur in the Bohm regime, thus $D(E) = D_{\rm B}(E) = 6.6 \times 10^{21} (E/{\rm GeV}) Z^{-1}$ cm^2 s^{-1} for $B = 5\,\mu$G. The solutions obtained are shown in Fig. 4.6.

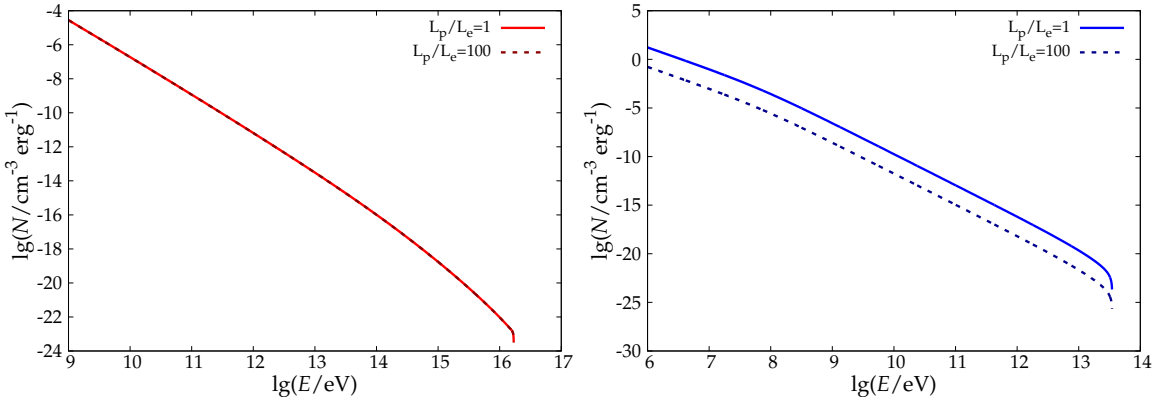

Figure 4.6: Distributions for $L_p/L_e = 1$ and $L_p/L_e = 100$ in the case of DSA in the reverse shock, assuming thermalization $\epsilon = 1$. The result for $\epsilon = 0.75$ does not significantly differ. *Left panel:* Protons. *Right panel:* Electrons.

4.5 Results

4.5.1 Spectral energy distributions

With the particle distributions calculated in the previous section, we compute the corresponding spectral energy distributions (SEDs) using the expressions presented in Section 3.4. The conversion efficiency ξ of kinetic energy into CRs has been fixed in order to match the observational gamma constraint imposed by *Fermi* and H.E.S.S. (see Abramowski et al. 2012; H. E. S. S. Collaboration et al. 2018; Abdollahi et al. 2020). In Fig. 4.7, we present the SEDs obtained in the case of DSA for $L_p/L_e = 1$ and $L_p/L_e = 100$, respectively. We find that at most 1% of the shock luminosity can be transfered to the accelerated particles. If a larger distance of 3.9 Mpc is considered for NGC 253, this efficiency increases up to ~2 %. Figure 4.8 show the results for SDA, for the same two values of L_p/L_e. Since the highest electron energies reached by the respective acceleration mechanisms are different, the cut-off position for their radiation is different as well. Therefore, the energy at which the suppression of the leptonic emission is observed can be used as a discriminant between SDA and DSA. In the SDA scenario, non-thermal X-ray emission is not generated, and hence, detection of this emission can allow to distinguish both models.

As indicated previously, M82 shares many similitudes with NGC 253, but these two sources are not the only starburst galaxies, that the *Fermi* satellite has detected. GeV gamma rays from NGC 4945, NGC 1068, Arp220, NGC 2146, Arp 299, and NGC 3424 have been also observed (Ballet et al. 2020), but most of these galaxies display slightly different characteristics. Table 4.3 and Table 4.4 show a summary of the gamma emission of these objects.

From the samples shown in Table 4.3 and Table 4.4, M82 and NGC 253 are the only galaxies that have been also detected in the TeV range (Karlsson 2009; H. E. S. S. Collaboration et al. 2018). Their spectral indices are both ~2.2. This value supports DSA as acceleration mechanism over SDA, because the latter produces typically harder spectra (see Figs. 4.4 and 4.6). Nevertheless, since these gamma sources are

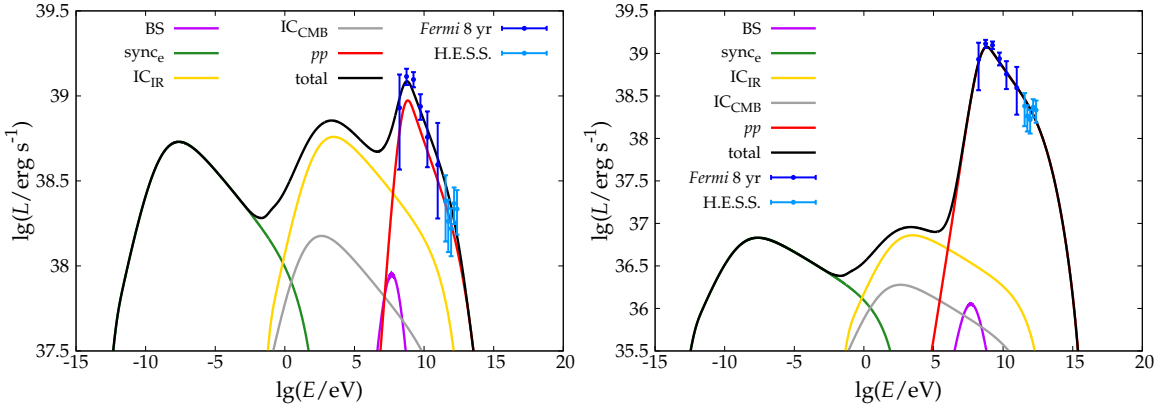

Figure 4.7: Spectral energy distribution in the case of DSA, magnetic field $B = 5\,\mu$G, and thermalization $\epsilon = 1$. The observational points were obtained from Abdollahi et al. 2020 (*Fermi* 8 yr) and H. E. S. S. Collaboration et al. 2018 (H.E.S.S.). *Left panel:* $L_p/L_e = 1$ and shock efficiency $\xi = 0.012$. *Right panel:* $L_p/L_e = 100$ and shock efficiency $\xi = 6 \times 10^{-3}$.

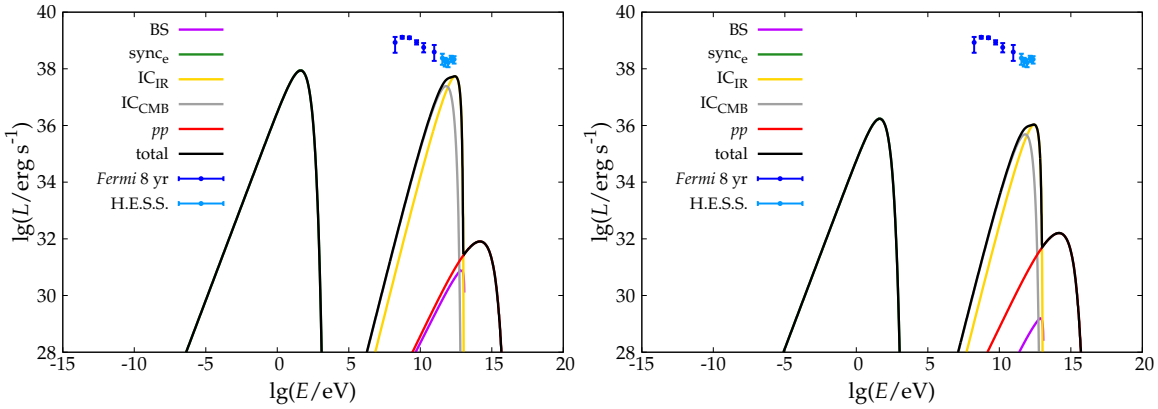

Figure 4.8: Spectral energy distribution in the case of SDA and magnetic field $B = 5\,\mu$G. The observational points were obtained from Abdollahi et al. 2020 (*Fermi* 8 yr) and H. E. S. S. Collaboration et al. 2018 (H.E.S.S.). *Left panel:* $L_p/L_e = 1$. *Right panel:* $L_p/L_e = 100$.

not resolved, it is not possible to rule out contributions from sources in the disk (see e.g., Bykov 2014).

Although NGC 4945 has a gamma luminosity of the same order as NGC 253 and M82, the X-ray evidence points out that actually this galaxy seems to be emitting because of its active galactic nucleus (AGN) nature and not starburst activity (Wojaczyński & Niedźwiecki 2017). Multi-wavelength studies show that, indeed, the behavior of NGC 4945 is more similar to NGC 1068 and the Seyfert galaxy Circinus than our standard starbursts. The same discussion is extended to NGC 1068, whose gamma luminosity is about one order of magnitude greater than in M82 or NCG 253. Lamastra et al. (2016) show that the typical models of emission coming from the starburst region do not manage to explain successfully the emission from NGC 1068 and propose that this can be originated by an AGN-driven galactic outflow. In

Chapter 6 we suggest another possible mechanism to explain the gamma emission from NGC 1068 based on the AGN scenario.

NGC 2146, NGC 3424, and Arp 220 have been reported for the first time in the *Fermi* 8-year Point Source Catalog (Abdollahi et al. 2020), whereas Arp 299 was recently detected by Ajello et al. (2020) using 10-year *Fermi* data. Arp 220 and Arp 299 are the two most distant star-forming galaxies detected at GeV energies. Both of them are actually a pair of merging galaxies with SFRs almost two orders of magnitude larger than the observed in NGC 253 or M82, as well as their high-energy luminosities. Nonetheless, despite the existence of starburst regions in these objects, there are some clues of AGN activity (see e.g., Yoast-Hull et al. 2017; Alonso-Herrero et al. 2013). On the other hand, the gamma emission measured for NGC 3424 is unusual and much larger than expected. The SFR of this galaxy is estimated to be similar to NGC 253, however its gamma luminosity is about one order of magnitude higher. Once again, this condition has been suggested to be related with an AGN (see e.g., Gavazzi et al. 2011; Peng et al. 2019). Finally, NGC 2146 does not show AGN activity. Its SFR is almost twice the deduced for NGC 253 or M82, but the galaxy is located six times farther away (Bernard-Salas et al. 2009). Nonetheless, a starburst-driven outflow has been discovered by Kreckel et al. (2014).

In virtue of the aforesaid, we conclude high-resolution observations of the non-thermal emission are necessary to understand which acceleration mechanism is operating in starburst galaxies. This could be possible in the future with observations of NGC 253 and M82 performed with the Cherenkov Telescope Array (CTA). Along with the resolution of the gamma component originated in the disk, well determined photon spectra might provide information to find out which of the proposed models is more accurate.

Table 4.3: Parameters of gamma-ray emitting starbursts taken from Ballet et al. (2020) (Catalog v24).

Parameter	Value			
	NGC 253	M82	NGC 4945	NGC 1068
Distance d [Mpc]	2.6[a]	3.7[b]	3.8[c]	14.4[d]
Spectral index Γ	2.14 ± 0.05	2.22 ± 0.04	2.27 ± 0.05	2.33 ± 0.06
$L_{100-300\mathrm{MeV}}$ [erg s^{-1}]	6.37×10^{38}	3.28×10^{39}	3.34×10^{39}	3.78×10^{40}
$L_{0.3-1\mathrm{GeV}}$ [erg s^{-1}]	1.14×10^{39}	3.06×10^{39}	4.20×10^{39}	3.98×10^{40}
$L_{1-3\mathrm{GeV}}$ [erg s^{-1}]	1.21×10^{39}	3.09×10^{39}	2.86×10^{39}	2.20×10^{40}
$L_{3-10\mathrm{GeV}}$ [erg s^{-1}]	7.97×10^{38}	1.85×10^{39}	2.33×10^{39}	1.12×10^{40}
$L_{10-30\mathrm{GeV}}$ [erg s^{-1}]	4.75×10^{38}	1.55×10^{39}	1.27×10^{39}	2.20×10^{40}
$L_{30-300\mathrm{GeV}}$ [erg s^{-1}]	2.86×10^{38}	4.85×10^{38}	8.58×10^{38}	$< 5.50 \times 10^{39}$
$L_{0.1-100\mathrm{GeV}}$ [erg s^{-1}]	$5.46 \pm 0.5 \times 10^{39}$	$1.74 \pm 0.8 \times 10^{40}$	$1.94 \pm 0.1 \times 10^{40}$	$1.62 \pm 0.1 \times 10^{41}$

[a] Davidge & Pritchet (1990). [b] Vacca et al. (2015). [c] Mould & Sakai (2008). [d] Tully (1988).

Table 4.4: Parameters of most recently detected gamma-ray emitting starbursts taken from Ballet et al. (2020) (Catalog v24).

Parameter	Value			
	NGC 2146	NGC 3424	Arp 220	Arp 299
Distance d [Mpc]	18.0[e]	27.2[f]	79.9[g]	47.7[h]
Spectral index Γ	2.14 ± 0.15	2.05 ± 0.2	2.41 ± 0.11	2.21 ± 0.18
$L_{100-300\mathrm{MeV}}$ [erg s^{-1}]	$< 1.70 \times 10^{40}$	5.66×10^{40}	8.47×10^{41}	1.59×10^{41}
$L_{0.3-1\mathrm{GeV}}$ [erg s^{-1}]	1.01×10^{40}	$< 8.66 \times 10^{39}$	4.78×10^{41}	5.15×10^{40}
$L_{1-3\mathrm{GeV}}$ [erg s^{-1}]	7.10×10^{39}	1.19×10^{40}	3.74×10^{41}	6.10×10^{40}
$L_{3-10\mathrm{GeV}}$ [erg s^{-1}]	1.1×10^{40}	1.59×10^{40}	1.8×10^{41}	4.67×10^{40}
$L_{10-30\mathrm{GeV}}$ [erg s^{-1}]	$< 6.64 \times 10^{39}$	2.86×10^{40}	8.12×10^{40}	$< 4.57 \times 10^{40}$
$L_{30-300\mathrm{GeV}}$ [erg s^{-1}]	9.36×10^{40}	1.98×10^{40}	1.34×10^{41}	3.86×10^{40}
$L_{0.1-100\mathrm{GeV}}$ [erg s^{-1}]	$6.35 \pm 0.1 \times 10^{40}$	$9.44 \pm 2.44 \times 10^{40}$	$2.5 \pm 0.3 \times 10^{42}$	$3.49 \pm 0.8 \times 10^{41}$

[e] Adamo et al. (2012). [f] Theureau et al. (2007). [g,h] Ajello et al. (2020).

4.6 Discussions

4.6.1 Higher energies?

Starburst galaxies were pointed out as ultra-high energy cosmic ray (UHECR) (10^{19}-10^{20} eV) sources, but our results show that the particles reach energies around 10^{17} eV at most. As we discussed in Section 3.4, the maximum energies for the hadrons are given by the age of the source. For our analysis, we adopt a value $\tau \sim 10$ Myr derived from the observed size of the superbubble and the velocity of the expanding shell. Consequently, to increase the maximum energy by two orders of magnitude, a starburst age of ~1 Gyr is needed. This value is very unfavorable taking into the account the observed mass loading factor (Bolatto et al. 2013), and even then, the acceleration of the particles will be suppress at energies ~10^{17} eV by diffusion.

Another alternative to achieve higher energies is to invoke stronger magnetic fields because of magnetic amplification, as discussed in Section 3.3.3.2. The maximum particle energies in the scenario here studied, neglecting any kind of losses, are given by

$$E_{\mathrm{max}} \sim 3.6 \times 10^{6} \left(\frac{B}{\mu \mathrm{G}} \right) \ \mathrm{GeV}. \tag{4.29}$$

Assuming a magnetic field value of $B = 1$ mG, which corresponds to a magnetic amplification of 200, the maximum energies become

$$E^{p}_{\mathrm{max}} = 3.6 \times 10^{18} \ \mathrm{eV} \quad \text{protons} \tag{4.30}$$

$$E^{\mathrm{Fe}}_{\mathrm{max}} = 9.4 \times 10^{19} \ \mathrm{eV} \quad \text{iron nuclei.} \tag{4.31}$$

These values are more similar to those found by Anchordoqui et al. (1999) and Anchordoqui (2018). Nevertheless, to generate a magnetic amplification with shock velocities of ~800 km s^{-1}, as in our case (see Table 4.1), is impossible. The ram pressure energy density of a medium whose density is 10^{-2} cm^{-3} becomes $n_{\mathrm{w}}\, m_p\, v_{\mathrm{w}}^2 \sim 10^{-10}$ erg cm^{-3}, whereas the magnetic energy density is $B^2/(8\,\pi) \approx 4{\times}10^{-8}$ erg cm^{-3}. In this situation, the medium turns out to be incompressible and the large-scale

shock cannot exist. Then, magnetic amplification could only coexist with the shock if the superwind shock is faster ($\sim 10^4$ km s^{-1}) or the average gas density inside the inflated bubble is higher. For NGC 253, both possibilities are ruled out by the observational evidence. Based on simulation studies, larger wind densities of 1.5×10^2 cm^{-3}, 6.75×10^2 cm^{-3}, and 10^3 cm^{-3} were suggested by Anchordoqui & Torres (2020). However, that work do not take any energy or escape loss into account. Since the timescale of *pp* inelastic collisions is inversely proportional to the medium density, particles accelerated in such dense environments should lose energy more efficiently because of this process. Consequently, the maximum energies achieved by protons should be at most $\sim 10^{17}$ eV. Finally, the only remaining alternative in which magnetic amplification can operate is in shocks around clumps or dense inhomogeneities inside the wind. This small-scale acceleration scenario is discussed in Chapter 5.

4.6.2 A starving black hole?

Another possible accelerator briefly discussed in Romero et al. (2018) is the supermassive black hole. The position and properties of the expected central black hole of NGC 253 have not been well determined. Because of the presence of gas and dust related with the starburst region, the central part of the galaxy is hidden and, for that reason, its observation becomes very complicated. None of the compact sources observed in some energy range have been detected emitting at other energies, except for the bright radio source TH2 found by Turner & Ho (1985) and reported afterwards as hard X-ray emitter by Weaver et al. (2002). This source could actually be a young SNR, but assuming it is similar to the Crab remnant, detectable IR/optical emission is expected. The absence of counterparts at those wavelengths suggests that its nature might be different. Fernández-Ontiveros et al. (2009) propose that TH2 is an inactive black hole similar to SgrA*. Current observations taken with the *Chandra* satellite reveal that the position of the hard X-ray source does not coincide with TH2 and therefore, they are not related to each other. Nowadays, this X-ray source is still being considered as a possible weak low-luminosity AGN (see Müller-Sánchez et al. 2010), however, a new candidate has been proposed. The IR source found by Günthardt et al. (2015) has a radio counterpart and it is associated with a large star cluster, where a massive black hole of $\sim 10^6$ M$_\odot$ can be hidden.

For black holes rotating in an external poloidal magnetic field B, a descent of the magnetic potential can occur. In such a gap, particles can be accelerated. If h is the height of the gap, and a is the black hole spin, the resulting electromotive force is given by (e.g., Znajek 1978; Levinson 2000)

$$\Delta V \sim 4.5\times10^{17}\left(\frac{a}{M}\right)\left(\frac{h}{R_g}\right)^2\left(\frac{B}{10^4\mathrm{G}}\right)\left(\frac{M}{10^6\ M_\odot}\right)\quad \mathrm{V}, \tag{4.32}$$

where R_g is the gravitational radius of the black hole.

Under the assumption of equipartition between the magnetic energy density and the accretion energy density (Boldt & Ghosh 1999; Levinson & Boldt 2002), the magnetic field becomes

$$\left(\frac{B}{10^4\mathrm{G}}\right) = 61\ \left(\frac{\dot{M}}{\dot{M}_{\mathrm{Edd}}}\right)^{1/2}\left(\frac{M}{10^6\ M_\odot}\right)^{-1}, \tag{4.33}$$

where $\dot{M}$ is the accretion rate, $\dot{M}_{\rm Edd} = L_{\rm Edd}\, c^2$, and $L_{\rm Edd} \approx 1.3{\times}10^{44}(M/10^6\,{\rm M}_\odot)$ erg s^{-1} (see Section 2.2.2).

Considering that the supermassive black hole in NGC 253 has a mass of $10^6\,{\rm M}_\odot$, its accretion rate is constrained by the X-ray luminosity $L_{\rm X}{\sim}10^{40}$ erg s^{-1} measured by Müller-Sánchez et al. (2010). If the Eddington efficiency is 10% (see e.g., Romero & Vila 2014b), the accretion efficiency $\dot{M}/\dot{M}_{\rm Edd}$ is at most 10^{-3}. From Eq. (4.33), the magnetic field is ~$2{\times}10^4$ G. Then, adopting $a \sim M$ and $h \sim R_{\rm g}$, Eq. (4.32) gives

$$\Delta V \sim 9 \times 10^{17}\ {\rm V}. \tag{4.34}$$

This potential drop can accelerate charged particles up to

$$E^{p}_{\rm max} = e\Delta {\rm V} \approx 9 \times 10^{17}\ {\rm eV} \quad \text{protons} \tag{4.35}$$

$$E^{\rm Fe}_{\rm max} = eZ\Delta {\rm V} \approx 2.3 \times 10^{19}\ {\rm eV} \quad \text{iron nuclei.} \tag{4.36}$$

This scenario was recently explored by Gutiérrez et al. (2020). In a more carefully analysis, they investigate the acceleration of particles by this mechanism in each of the three nuclear candidates of NGC 253. The authors find that none of the sources attain to accelerate protons above 10^{13} eV or iron above 10^{15} eV. Additionally, the relativistic particles generated close to the black hole could be responsible at most of 10 % of the observed gamma emission. In consequence, the black hole at the center of NGC 253 is ruled out as source of UHECRs.

4.6.3 Other potential sources of CR in the disk

Alternative potential sources of UHECRs can be found in the starburst region. The stellar evolution and the high SFR generate a large number of magnetars and core-collapse SN type Ibc, where CRs up to ultra-high energies might be produced (e.g., Fang et al. 2012a; Chakraborti et al. 2011). Nonetheless, the electromagnetic radiation produced by such sources is extremely complicated to observe because of the strong absorption of the star-forming region and therefore, these models cannot be easily verified.

On the other hand, the interaction of the detected superwind with the SNe can accelerate particles above 100 PeV (Bykov 2001, 2014; Bykov et al. 2018). The CRs are then transported by the outflow into the galactic halo, and there, might be re-accelerated in the wind terminal shock. However, the adiabatic losses suffered by these particles might be important, and therefore, the final maximum energies can be smaller. In addition, it is not well understood if the escaping particle flux produced above 10^{18} eV is considerable.

4.6.4 Propagation and effects upon arrival

Resolving NGC 253 as individual source of UHECRs is a very complicated task, even if the particles could reach energies of the order of 10^{19}-10^{20} eV. The Galactic magnetic field models have been improved in the last years with the data provided by measurements of the Faraday rotation and the polarization of synchrotron radiation (Pshirkov et al. 2011; Jansson & Farrar 2012a,b). Notwithstanding, the uncertainties

are still quite large, especially the total deflection suffered by extragalactic CRs (Unger & Farrar 2017).

Since NGC 253 is a very nearby source, it is possible to consider that the accelerated nuclei, that attain to escape, reach the Earth without suffering photo-disintegration (Kampert et al. 2013; Batista et al. 2016). Nevertheless, from the magnetic field models already mentioned, Erdmann et al. (2016) derived a minimal rigidity for ballistic deflections of the order of E/Z =6 EV. This value is two orders of magnitude larger than the rigidity of the particles accelerated even invoking magnetic amplification as discussed above (see Section 4.6.1-Section 4.6.1). The region at latitudes below –19.5°, where NGC 253 is located, presents deflections up to 50° for a rigidity of 6 EV.

The only promising chance to discern NGC 253 resides in the search for multiple events of individual mass groups but in the same rigidity range (P. Abreu *et al.* (Pierre Auger Collab.) 2012). This analysis is motivated by the intermediate-mass dominated composition observed for UHECRs at energies $10^{19.65}$ eV (Aab et al. 2017, 2014). The feasibility of this method is still being evaluated and the Auger Collaboration expects to give more details in a forthcoming paper.

4.7 Summary and conclusions

In this chapter, we investigated starburst galaxies as UHECRs sources motivated by the exposed in Section 2.2.1. In particular, we computed results for the nearby starburst galaxy NGC 253.

The observational data suggest that starburst galaxies are indeed CR accelerators. Non-thermal radio and gamma emission from these sources are detectable, revealing the existence of relativistic particles therein. Starburst galaxies are metal-rich environments, because of the intense star-forming activity. Therefore, a large amount of heavy nuclei is expected to be available there for acceleration. We focused particularly on the production of CR in the large-scale outflow driven by starburst regions. The superwind is a propitious place for UHECRs because of its large extension, which allows to retain easily particles even with the highest energies. The acceleration can occur in the large-scale shock created by the interaction of the wind with the ambient matter due to DSA, or in the turbulent bubble plasma by SDA.

Using all the information provided by the multi-wavelength observational data available, we found that particles can be accelerated up to 10^{18} eV in the superwind region of starburst galaxies, particularly in NGC 253. This energy value can be achieved by both acceleration mechanisms proposed. To reach energies of the order of 100 EeV under normal circumstances seems to be impossible. A more efficient acceleration is hampered by the moderate velocity of the shock (less than 1000 km s^{-1}), as result of the large mass carried by the wind. At the same time, SDA is limited by the slow Alfvén velocities in the turbulent bubble plasma.

Stronger magnetic fields (~300 μG), as suggested in other works (see Anchordoqui 2018), can be produced by magnetic amplification, as occurs in SNRs. Nevertheless, the parameters derived from the observational data do not allow the existence of the large-scale shock in the superwind medium in presence of such a high magnetic field. To avoid the incompressibility of the medium, higher matter densities are required. This condition can be however satisfied in small parts of the superwind gas, from

where radio and X-ray emission are expected. This situation is investigated and discussed in the next chapter.

Summarizing, we conclude that in starburst galaxies particles can be accelerated up to relativist energies. The CRs generated in these astrophysical environments are capable of emitting an amount of non-thermal radiation much larger than the observed in the Milky Way. However, if UHECRs can be produced is unknown.

5

Particle acceleration in the superwind of starburst galaxies[†]. Part II: Small-scale processes

5.1 Introduction

In the previous chapter, we analyzed the cosmic ray (CR) production at the terminal shocks of starburst superwinds. We found that the maximum energies are $\sim 10^{17}$ eV, limited mainly by the mass loading factor of the wind and the magnetic field strength.

The large amount of energy injected by the powerful star formation, along with their metal-rich environments, make starburst galaxies favorable places for the production of ultra-high energy cosmic ray (UHECR). This idea is particularly motivated by the increasing mass composition for CRs at the highest energies observed by the Pierre Auger Observatory (Auger), along with the correlation between arrival directions and the positions of these galaxies (Aab et al. 2014; The Pierre Auger Collaboration et al. 2017, 2019). The superwind is an excellent region in starbursts where particles with large Larmor radii and heavy composition can be confined and accelerated without suffering photo-disintegration (Anchordoqui et al. 1999). Observationally, the presence of relativistic particles in starburst galaxies has been proved by the gamma emission detected from nearby objects (Acero et al. 2009; Abdo et al. 2010; Ackermann et al. 2012b; Ohm 2016; Abdollahi et al. 2020).

In this chapter, we focus on a small-scale scenario where magnetic amplification can occur. We have already discussed in Chapter 4 the possibility of magnetic amplification in the terminal shock of the galactic outflow and we have found that the parameters inferred from the observations in NGC 253 do not allow stronger magnetic fields coexisting with the large-scale shock. As mentioned before, the expansion velocity of the superwind in the galactic halo is typically

$$v_{w\infty} = \sqrt{2\dot{E}/\dot{M}} \sim 10^3 \,\mathrm{km\,s^{-1}}, \tag{5.1}$$

where $\dot{E}$ and $\dot{M}$ are the total energy and mass injected per unit of time by the superwind, respectively (see Eq. (4.4) and Eq. (4.5)). Heesen et al. (2009b) derived from radio observations a magnetic field of the order of 5 µG in the galactic halo of NGC 253. At the same time, the average particle density inferred by Strickland

[0]Contents of this chapter are already published in Müller et al. (2020) https://doi.org/10.1093/mnras/staa1720

et al. (2002) from X-ray observations is $n_w \sim 2{\times}10^{-3}\,\mathrm{cm}^{-3}$, and the size of the superbubble $R_{kpc} \sim 5$. Invoking diffusive shock acceleration (DSA) and stochastic diffusive acceleration (SDA) under such conditions, we have seen in the previous chapter that the maximum energies obtained are $\sim 10^{16}$ eV and $\sim 5{\times}10^{17}$ eV for protons and iron nuclei, respectively (see Section 4.6.1 and Section 4.6.1). On the other hand, Anchordoqui (2018) found energies of around 10^{20} eV using a magnetic field of 300 μG. Consequently, the magnetic energy density becomes $u_B = B^2/8\pi \sim 4{\times}10^{-9}\,\mathrm{erg\,cm}^{-3}$, whereas the gas ram pressure is only $u_g \approx n_w\, m_p\, v_w^2 \sim 10^{-11}\,\mathrm{erg\,cm}^{-3}$. Then, the magnetization parameter is

$$\beta = \frac{u_B}{u_g} >> 1, \tag{5.2}$$

which means the medium is mechanically incompressible and the large-scale shock cannot exist.

The incompressibility problem would be solve, if the medium density is higher. The average large-scale density is too low to allow magnetic amplification and a coexisting terminal shock. Nevertheless, denser small-scale inhomogeneities inside of the superwind should exist. Around these clumps, the interaction of the wind fluid can develop bowshocks wherein magnetic amplification might occur.

The magnetic field has been detected strengthened in galactic supernova remnants, where the density contrast of the interacting media is high (Bamba et al. 2003; Vink & Laming 2003). Nevertheless, how this mechanism specifically works is unknown. Bell (2004) has suggested that the process is lead by the non-resonant hybrid instability, also called the Bell instability. In this way, the weak magnetic fields can be amplified up to two orders of magnitude (see Section 3.3.3.2).

The basics of the origin of superwinds were first given by Chevalier & Clegg (1985). Over the years, many authors contributed to improve the model through analytical analyses and numerical simulations (see e.g., Strickland et al. 2000; Cooper et al. 2008). As mentioned previously, the outflow is powered by a large number of hot bubbles created by the intense star formation in the starburst region. The bubbles merge and expand inducing the thermalization of the gas and creating a hot cavity. After ~0.15 Mpc, the gas breaks the galactic disk and escapes into the halo. During this process, cold denser fragments of the disk are swept-up by the hot fluid. The velocity of the wind becomes rapidly $\sim 10^3\,\mathrm{km\,s}^{-1}$. The pressure of the wind fluid applied on the clouds accelerate the fragments along the flow lines. Given that the superwind moves supersonically, the interaction with the clumps develop bockshows around them. An scheme of the physical situation is shown in Fig. 5.1.

Cooper et al. (2008) show through 3D hydrodynamical simulations that the clouds are ablated by the wind after 2 Myr. The gas of the clouds becomes then part of a cold stream of material, which forms a filamentary-like structure (see Fig. 13 in Cooper et al. 2008). The acceleration of a cloud by the wind can be expressed as

$$a_{acc} \approx \xi \left(\frac{n_w}{n_c}\right) \frac{v_w^2}{R_c}, \tag{5.3}$$

where $\xi \sim 1$ is the dragging coefficient, and R_c and n_c are the radius and density of the cloud, respectively. For instance, a cloud with $R_c = 5\,\mathrm{pc}$ and $n_c = 100\,\mathrm{cm}^{-3}$, interacting with a wind of velocity $v_w = 2000\,\mathrm{km\,s}^{-1}$ and average density $n_w = 10^{-3}\,\mathrm{cm}^{-3}$ would

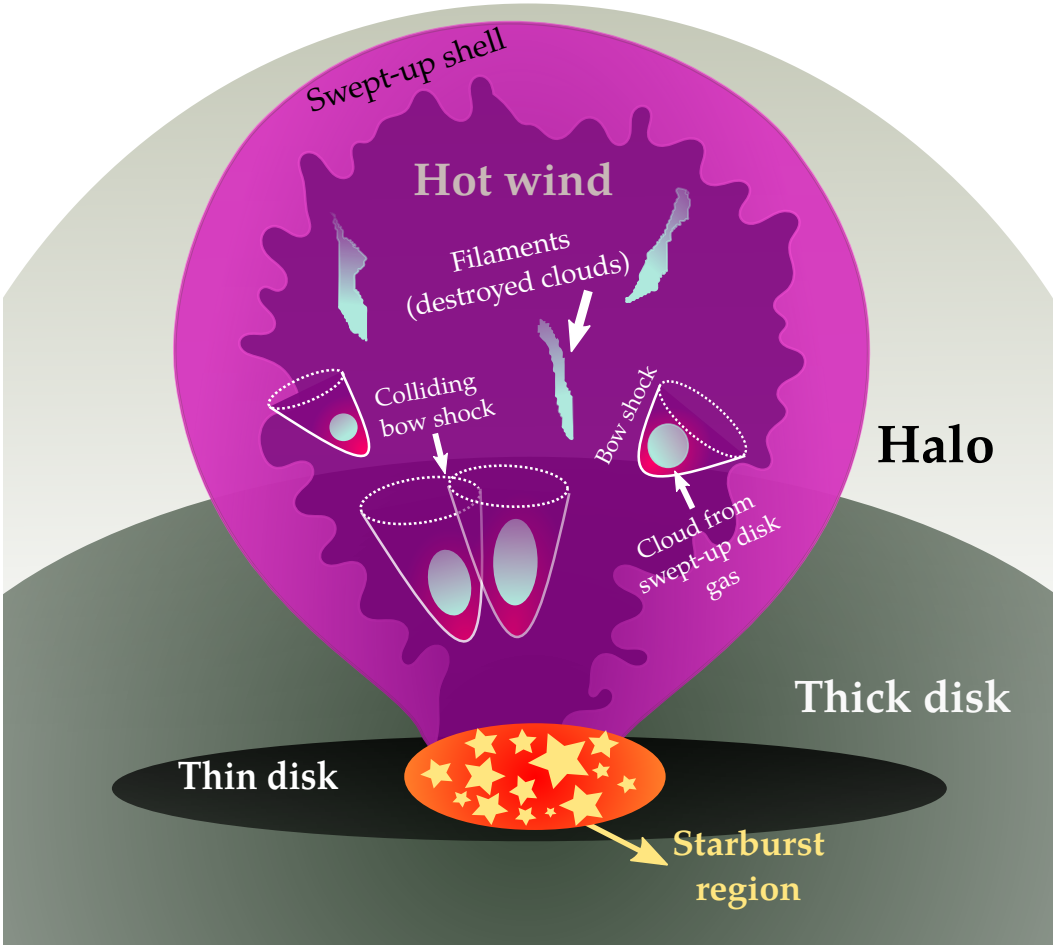

Figure 5.1: Scheme of starburst hot superwind interacting with several clouds in the halo (not to scale). Based on Cooper et al. (2008).

suffer an acceleration $a_{\rm acc} \sim 10^{-13}\,{\rm km\,s^{-2}}$. Since the clouds are initially almost at rest, and the acceleration value is too small, clouds cannot achieve large velocities on the lifetime of a starburst episode. The approximation used to estimate the acceleration does not consider hydrodynamic details, like deformation of the clouds or the effects caused by shocks. However, the result shows that the wind is generally supersonic with respect to the cloud and consequently, the interaction will lead to the formation of bowshocks around the clouds.

5.2 Model

Interactions between clouds and hot winds have been studied by several authors over the years. Klein et al. (1994) determined four phases in the evolution of one of these interactions. At the beginning, when the wind encounters the cloud, two shocks are formed (see Section 3.3.3.1). The forward shock propagates through the cloud, whereas the reverse shock moves backwards through the wind. The apex of the bowshock is located at a distance of $x \sim 0.2R_{\rm c}$ (van Dyke & Gordon 1959), where a contact discontinuity is established. The shocked gas of the wind streams

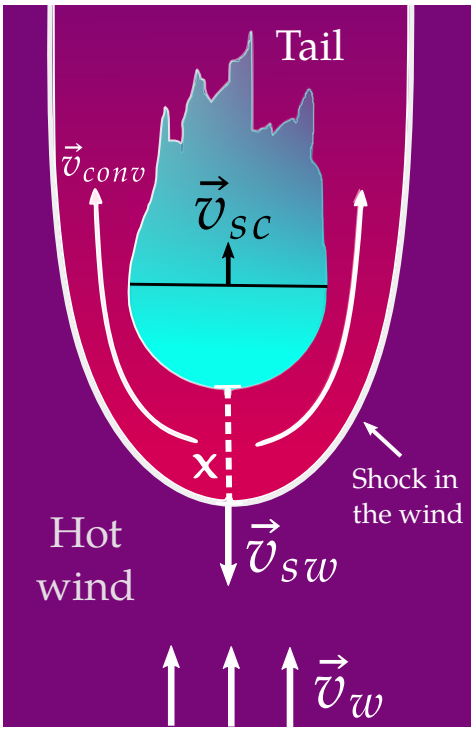

Figure 5.2: Schematic diagram of the bowshock around a cloud immersed in the starburst hot superwind (not to scale).

with a velocity $v_{\rm conv}$ inside this region of height x, triggering Kelvin-Helmholtz (KH) instabilities. On the front part of the cloud, Rayleigh-Taylor (RT) instabilities can be also created by the pressure exerted by the wind fluid. When the shock reaches the rear part of cloud, it produces a turbulent rarefaction of the matter and the cloud develops a tail of gas. In the end, the cloud is destroyed by the instabilities and turns into many small fragments. A representation of clouds in all their interacting phases is shown in Fig. 5.1. Expressions for the calculation of the timescales corresponding to the instabilities are given by Klein et al. (1994)

$$t_{\rm KH} = \frac{R_{\rm c}(n_{\rm c} + n_{\rm w})}{(v_{\rm w} - v_{\rm c})(n_{\rm c} n_{\rm w})^{1/2}}, \tag{5.4}$$

$$t_{\rm RT} = \sqrt{\frac{R_{\rm c}}{a_{\rm c}}} \approx \frac{R_{\rm c}}{v_{\rm w}} \sqrt{\frac{n_{\rm c}}{n_{\rm w}}}. \tag{5.5}$$

We adopt the radius of the cloud as characteristic length of the instability.

The timescale associated with the cloud-wind interaction is given by the length of the cloud and the velocity of the shock propagating through it (Klein et al. 1994)

$$t_{\rm crush} \approx \frac{R_{\rm c}}{v_{\rm sc}} \approx \frac{R_{\rm c}}{v_{\rm w}} \sqrt{\frac{n_{\rm c}}{n_{\rm w}}}, \tag{5.6}$$

where $v_{\rm sc}$ is the velocity of the shock-into-the-cloud. The evolution of the crushing cloud depends on many factors. Hydrodynamic simulations in 2D and 3D show that the morphology of the cloud, its density, the efficiency of radiative cooling, and the existence of magnetic fields determine how the ablation proceeds (Xu & Stone 1995;

Gregori et al. 2000; Shin et al. 2008; Cooper et al. 2009; McCourt et al. 2015; Sparre et al. 2019). For instance, clouds with fractal shapes are disrupted much faster than spherical clouds (Cooper et al. 2009). If significant magnetic fields exist, the cloud becomes more resistant and cohesive (McCourt et al. 2015). Moreover, the possibility of radiative cooling has a big impact on the lifetime of the cloud. The energy injected by the shock into the cloud cannot be radiated away if the cloud is adiabatic. As result, the gas expands, increasing the cloud radius. The effect of the instabilities is magnified and the ablation of the cloud begins practically instantaneously. On the other hand, the injected heat is successfully radiated away in radiative clouds. Then, the destruction of the cloud is delayed and the cloud remains cold ($T \sim 10^4$ K), in contrast to adiabatic clouds whose temperatures are $\sim 10^6$ K.

The velocities of the forward and reverse shock can be computed using Eq. (3.32) and Eq. (3.31), respectively. The adiabaticity of the shocks can be studied as in the previous chapter, with the expressions in Section 3.3.3.1.

The large difference of densities between the cloud and the wind creates a strong adiabatic shock propagating through the wind, and a slow radiative shock in the cloud. Whereas in the adiabatic shock DSA can operate and inject relativistic particles, the radiative cooling in the cloud shock can destroy the magnetic inhomogeneities, block the scattering of particles, and prevent the acceleration.

The space of possible parameters is quite extensive. Nevertheless, the phenomenology of this scenario is basically determined by the ratio of the densities and the velocity of the wind. Therefore, we run our simulations for two parameter sets. In both models the velocity and density of the wind are assumed $v_{\rm w} = 10^3\,{\rm km\,s^{-1}}$ and $n_{\rm w} = 10^{-2}\,{\rm cm^{-3}}$, respectively. Model M1 is composed by a small spherical cloud with radius $R_{\rm c} = 5\,{\rm pc}$ and density $n_{\rm c} = 10^2\,{\rm cm^{-3}}$, whereas model M2 consist of a larger cloud, also spherical, with $R_{\rm c} = 100\,{\rm pc}$ and density $n_{\rm c} = 10\,{\rm cm^{-3}}$. These densities correspond to typical values of the disk matter of a starburst galaxy. All the parameters have been chosen to match those adopted by Cooper et al. (2009) (M1) and Sparre et al. (2019) (M2)[1]. The magnetic field is fixed in the wind, as well as in the cloud, requiring that the magnetization parameter is $\beta = 0.90$. This condition permits the amplification of the magnetic field up to hundreds of μG, preventing the mechanically incompressibility of the medium. Consequently, the magnetic field in the acceleration region becomes

$$u_{\rm B} = 0.9\, u_{\rm g}$$

$$\frac{B_{\rm sw}^2}{8\,\pi} = 0.9\,\frac{3}{2} P_{\rm ram} = 0.9\,\frac{9}{8}\, n_w\, m_p\, v_{\rm sw}^2$$

$$B_{\rm sw} = \sqrt{\frac{81}{10}\,\pi\, n_w\, m_p\, v_{\rm sw}}. \tag{5.7}$$

This gives a magnetic field of $B_{\rm sw}\sim 86\,\mu$G for M1 and $B_{\rm sw}\sim 84\,\mu$G for M2.

Table 5.1 show all the parameters of the models, along with obtained magnetic fields, and the shock velocities. The small velocities of the shocks propagating in

[1]The newer work confirmed the results of the older, and therefore, it is appropiate to combine parameters sets of both publications.

Table 5.1: Parameters of the models. The magnetization $\beta = 0.9$ and the wind velocity $v_w = 1000$ km s^{-1} are the same in both cases.

Model	R_c [pc]	n_w [cm^{-3}]	n_c [cm^{-3}]	v_{sw} [km s^{-1}]	v_{sc} [km s^{-1}]	B_{sw} [μG]
M1	5	0.01	100	1320	4.2	86
M2	100	0.01	10	1292	13.2	84

Table 5.2: Dynamical timescales.

Model	t_{crush} [Myr]	t_{KH} [Myr]	t_{RT} [Myr]	$t_{\Lambda_{sc}}$ [Myr]	$t_{\Lambda_{sw}}$ [Myr]
M1	0.37	0.49	0.37	1.15×10^{-3}	64.78
M2	2.39	3.09	2.39	1.46×10^{-5}	60.53

the cloud suggest that, in effect, these shocks are radiative and the acceleration of particles is inefficient. Table 5.2 shows the corresponding values of the dynamical timescales. The thermal cooling of both clouds proceeds so fast that they are fully radiative, whereas the shocks in the wind are adiabatic. For the two models, the crushing time of the cloud yields the dynamical lifetime of the bowshock.

5.3 Particle acceleration and losses

5.3.1 Acceleration conditions

In the previous section, we showed that the reverse shock moving in the wind is adiabatic. For typical observed wind temperatures of the order of $\sim 10^6$ K, the speed of the sound in that medium results in $c_s \approx 100\,\mathrm{km\,s^{-1}}$ (see Eq. (3.30)). The Mach number of the reverse shock becomes then $v_{sw}/c_s > \sqrt{5}$, indicating that the shock is strong. In consequence, DSA can operate in the backward shock in the wind, accelerating charged particles up to relativistic energies. Analogous bowshock scenarios have been investigated by several authors, but never in this context (see, e.g., Araudo et al. 2009, 2010; del Valle & Romero 2012; del Valle et al. 2018; del Valle & Pohl 2018; del Palacio et al. 2018).

5.3.2 Losses and maximum energies

The size of the acceleration region is given by the distance to the bowshock apex, i.e., x (see Fig. 5.2). Then, the maximum energies that particles can reach before they leave the acceleration region are given by the Hillas criterion (Eq. (3.2)). The results obtained for our models are

Model M1:

$$E^{p}_{\max} = 8.6{\times}10^{16}\,\mathrm{eV} \quad \text{protons} \tag{5.8}$$
$$E^{\mathrm{Fe}}_{\max} = 2.2{\times}10^{18}\,\mathrm{eV} \quad \text{iron nuclei} \tag{5.9}$$

Model M2:

$$E^{p}_{\max} = 1.7{\times}10^{18}\,\mathrm{eV} \quad \text{protons} \tag{5.10}$$
$$E^{\mathrm{Fe}}_{\max} = 4.4{\times}10^{19}\,\mathrm{eV} \quad \text{iron nuclei} \tag{5.11}$$

These upper limits are actually more constrained by the spatial and radiative losses suffered by the particles. Particles can escape from the acceleration region because of diffusion or convection. Particularly, we assume the diffusion proceeds in the Bohm regime. Considering that the particle will leave the acceleration site after diffusing a distance x, the associated timescale (Eq. (3.46)) becomes

$$t_{\mathrm{diff,\,Bohm}} \sim 10^{13} \left(\frac{R_{\mathrm{c}}}{\mathrm{pc}}\right)^{2} \left(\frac{B}{\mu\mathrm{G}}\right) \left(\frac{E}{\mathrm{GeV}}\right)^{-1} \mathrm{s}. \tag{5.12}$$

Then,

$$t^{\mathrm{M1}}_{\mathrm{diff,\,Bohm}} \sim 6.8 \times 10^{2} \left(\frac{E}{\mathrm{GeV}}\right)^{-1} \mathrm{Myr}, \tag{5.13}$$

$$t^{\mathrm{M2}}_{\mathrm{diff,\,Bohm}} \sim 2.7 \times 10^{5} \left(\frac{E}{\mathrm{GeV}}\right)^{-1} \mathrm{Myr}. \tag{5.14}$$

On the other hand, the convection time is $t_{\mathrm{conv}} \approx 4R_{\mathrm{c}}/v_{\mathrm{w}}$, which means

$$t^{\mathrm{M1}}_{\mathrm{conv}} {\sim} 4.7{\times}10^{11}\,\mathrm{s} \sim 1.5{\times}10^{-2}\,\mathrm{Myr}, \tag{5.15}$$
$$t^{\mathrm{M2}}_{\mathrm{conv}} {\sim} 9.5{\times}10^{12}\,\mathrm{s} \sim 3{\times}10^{-1}\,\mathrm{Myr}. \tag{5.16}$$

The acceleration timescale by DSA is given in Eq. (3.26). Adopting the Bohm coefficient as the diffusion coefficient, it can be found that

$$t_{\mathrm{acc}} \approx 2.1\, Z^{-1} \left(\frac{D}{D_{\mathrm{B}}}\right) \left(\frac{v_{\mathrm{sw}}}{1000\,\mathrm{km\,s^{-1}}}\right)^{-2} \left(\frac{B}{\mu\mathrm{G}}\right)^{-1} \left(\frac{E}{\mathrm{GeV}}\right) \mathrm{yr}. \tag{5.17}$$

Replacing the magnetic fields of 86 µG and 84 µG previously found for M1 and M2, respectively

$$t^{\mathrm{M1}}_{\mathrm{acc}} \approx 2.46 \times 10^{-8}\, Z^{-1} \left(\frac{E}{\mathrm{GeV}}\right) \mathrm{Myr}, \tag{5.18}$$

$$t^{\mathrm{M2}}_{\mathrm{acc}} \approx 2.52 \times 10^{-8}\, Z^{-1} \left(\frac{E}{\mathrm{GeV}}\right) \mathrm{Myr}. \tag{5.19}$$

For the protons, the principal radiative losses are caused by the proton-proton (pp) inelastic collisions (cooling time given by Eq. (3.77)). However, since the timescale for pp collisions is much longer than the lifetime of the source, such losses become negligible and the maximum energies for protons are limited by the diffusion of

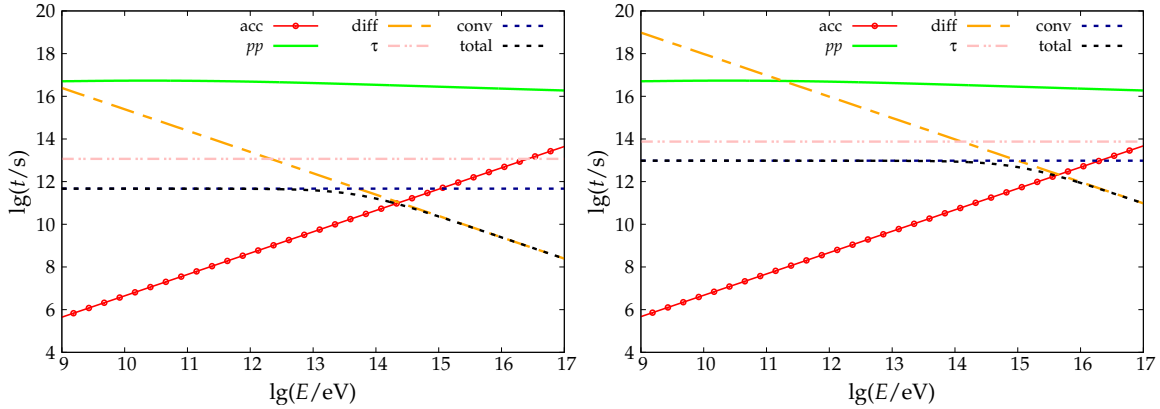

Figure 5.3: *Left panel:* Acceleration and cooling timescales for the protons in M1 model. *Right panel:* Acceleration and cooling timescales for the protons in M2 model.

particles (see Fig. 5.3). Consequently, the highest energies can be found matching Eq. (5.18) and Eq. (5.19) with Eq. (5.13) and Eq. (5.14)

Model M1:

$$E^{p}_{\rm max} = 1.7{\times}10^{14}\,{\rm eV} \quad \text{protons} \tag{5.20}$$

$$E^{\rm Fe}_{\rm max} = 4.3{\times}10^{15}\,{\rm eV} \quad \text{iron nuclei} \tag{5.21}$$

Model M2:

$$E^{p}_{\rm max} = 3.3{\times}10^{15}\,{\rm eV} \quad \text{protons} \tag{5.22}$$

$$E^{\rm Fe}_{\rm max} = 8.6{\times}10^{16}\,{\rm eV} \quad \text{iron nuclei.} \tag{5.23}$$

These values are much smaller than the estimated with the Hillas criterion (see Eqs. (5.8)–(5.11)) and therefore, UHECRs cannot be originated in the current scenario.

In the case of the electrons, the radiative losses correspond to synchrotron radiation, relativistic Bremsstrahlung, and inverse Compton up-scattering of Cosmic Microwave Background (CMB) and infrared (IR) photons. The latter radiation comes from the central region of the starburst and its energy density drops with the square of the distance to the plane of the galaxy. We adopt for the IR luminosity a typical value of $10^{10.5}\,{\rm L}_{\odot}$, which is emitted by a blackbody of the temperature of 40 K (Lacki & Thompson 2013).

Larger fragments of dense matter are expected to be located close to their birthplace, i.e., the galactic disk. Therefore, we assume a distance of 500 pc for M2. Since smaller clouds can be carried farther away from the disk, we place our M1 cloud at 1 kpc. The cooling times corresponding to the losses mentioned here are defined in Section 3.4.

Synchrotron radiation dominates the losses for the electrons in M1 (see Fig. 5.4), whereas in M2 the cooling timescale for synchrotron and the IC up-scattering of IR photons become similar. The maximum energies in the latter case can be calculated from $t^{-1}_{\rm acc} \approx t^{-1}_{\rm synchr} + t^{-1}_{\rm IC} \approx 2\,t^{-1}_{\rm synchr}$. The resulting maximum values are $E^{e}_{\rm max} = 6.7{\times}10^{12}$ eV for M1 and $E^{e}_{\rm max} = 4.9{\times}10^{12}$ eV for M2.

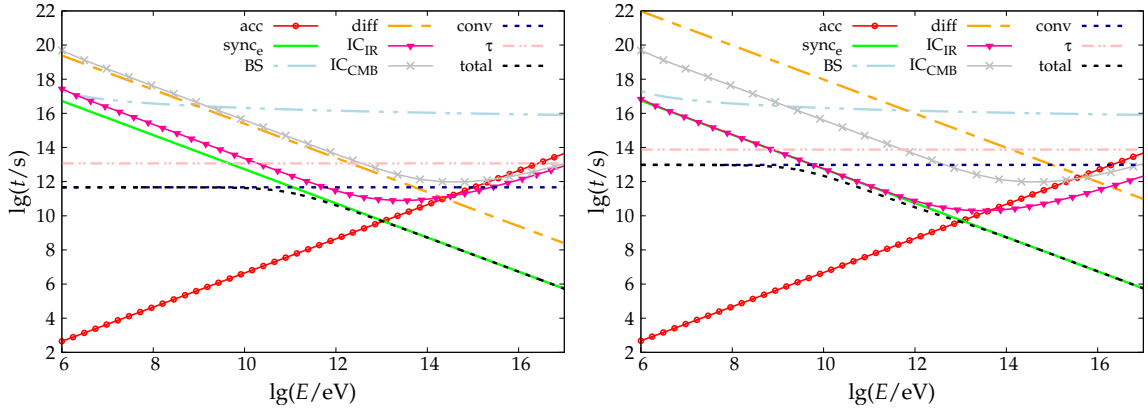

Figure 5.4: *Left panel:* Acceleration and cooling timescales for the electrons in M1. *Right panel:* Acceleration and cooling timescales for the electrons in M2.

5.3.3 Particle distributions

In order to obtain the energy particle distributions, we solve the transport equation (Section 3.2). For DSA acceleration, it takes the form

$$\frac{\partial N_{e,p}(E,t)}{\partial t} + \frac{\partial [b_{e,p}(E) N_{e,p}(E,t)]}{\partial E} + \frac{N_{e,p}(E,t)}{t_{\rm esc}} = Q_{e,p}(E). \tag{5.24}$$

Since the proton and electron distributions reach the steady state, the solution of this equation is just the given in Eq. (3.28). We model the particle injection as a power law with index $\Gamma = 2$, which is the characteristic value for DSA in strong adiabatic shocks, and an exponential cut-off given by the maximum energy: $Q_{e,p}(E) = Q_0^{e,p} E^{-2} \exp(-E/E_{\rm max}^{e,p})$. The term $b_{e,p}(E)$ is the sum of all the different radiative losses, whereas $t_{\rm esc}^{-1} = t_{\rm conv}^{-1} + t_{\rm diff}^{-1}$.

The adiabatic shock luminosity is defined as $L_{\rm kin} \approx (1/2)\, n_{\rm w}\, m_p\, v_{\rm sw}^3\, A_{\rm shock}$, where $A_{\rm shock}$ is the surface area of the shock (Lehnert et al. 1999). We consider that the curvature of the bowshock can be neglected along a quarter of the surface area of the sphere of radius $R_{\rm c} + x$ centered in the cloud. Consequently, $A_{\rm shock} = 2\,\pi\,(R_{\rm c} + x)^2$. The shock powers obtained for M1 and M2 are $L_{\rm kin}^{\rm M1} \sim 4.83{\times}10^{37}$ erg s^{-1} and $L_{\rm kin}^{\rm M2} \sim 1.55{\times}10^{40}$ erg s^{-1}, respectively. Assuming that 10% of this power is actually available to accelerate particles, we distribute the luminosity that goes to protons and electrons in two ways: i) equally distributed among both particle types ($L_p/L_e = 1$), and ii) a ratio of proton to electron of power of hundred ($L_p/L_e = 100$). The resulting particle distributions are shown in Fig. 5.5 and Fig. 5.6.

5.4 Results

5.4.1 Spectral energy distributions

In order to calculate the spectral energy distributions (SEDs), we use the particle distributions obtained in the preceding section together with the formulas presented in Section 3.4. The results are shown in Fig. 5.7 and Fig. 5.8. In these plots, we

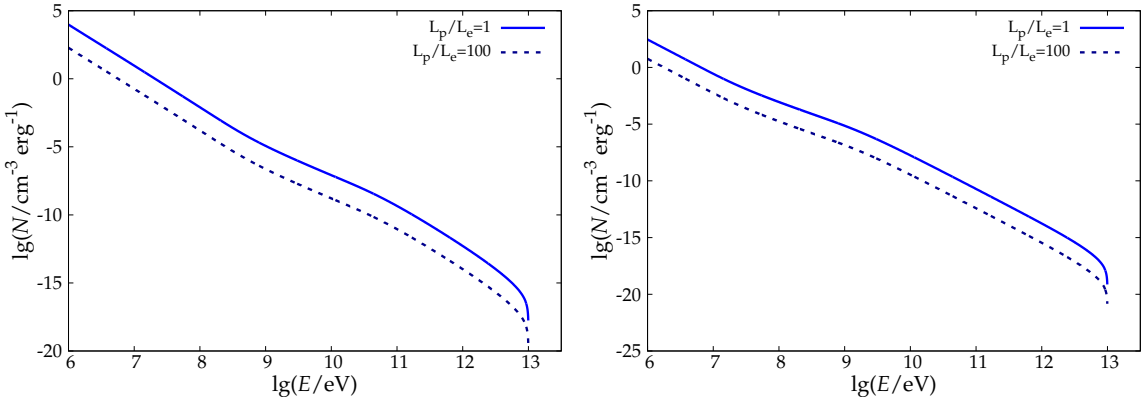

Figure 5.5: *Left panel:* Distribution of electrons for M1. *Right panel:* Distribution of electrons for M2.

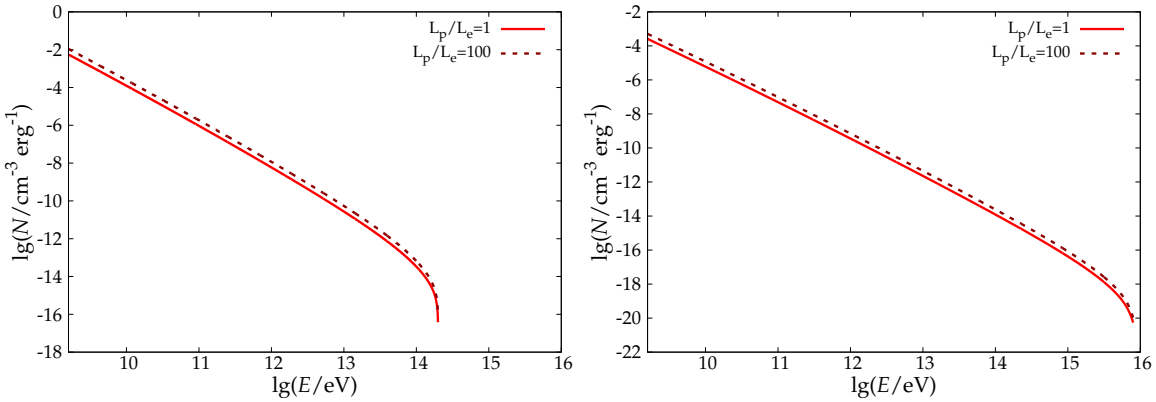

Figure 5.6: *Left panel:* Distribution of protons for M1. *Right panel:* Distribution of protons for M2.

also include the thermal Bremsstrahlung from the shocked wind material at the bowshock. For its estimation we use the expressions from Rybicki & Lightman (1979) (see Appendix B.1). This emission is not used as target for IC scatterings because its energy density is much smaller than the energy density of the CMB or the IR radiation field. The thermal radiation produced by the shocked gas of the cloud is neglected since the initial temperature is $\sim 10^4$ K (Marcolini et al. 2005), and the heating produced by the slow shock is not enough to exceed that value.

The resulting SEDs show that in the case of similar energy injected between electrons and protons, inverse Compton (IC) produces the bulk of emission at high energies. If the acceleration of hadrons is favored, such energies are dominated by the gamma rays produced in pp interactions. For small clouds (model M1), the emission spectrum has a maximum value of $\sim 7\times10^{34}$ erg s^{-1} at optical wavelengths. In the gamma-ray energy band, the luminosity reaches as maximum $\sim 10^{34}$ erg s^{-1}. On the contrary, big clouds (model M2) produce higher emission. The absolute maximum is $\sim 10^{37}$ erg s^{-1}. This value is achieved at the same time between radio and optical wavelengths, in addition to hard X-rays and soft gamma rays. The possibilities of detecting this radiation are discussed in the following section.

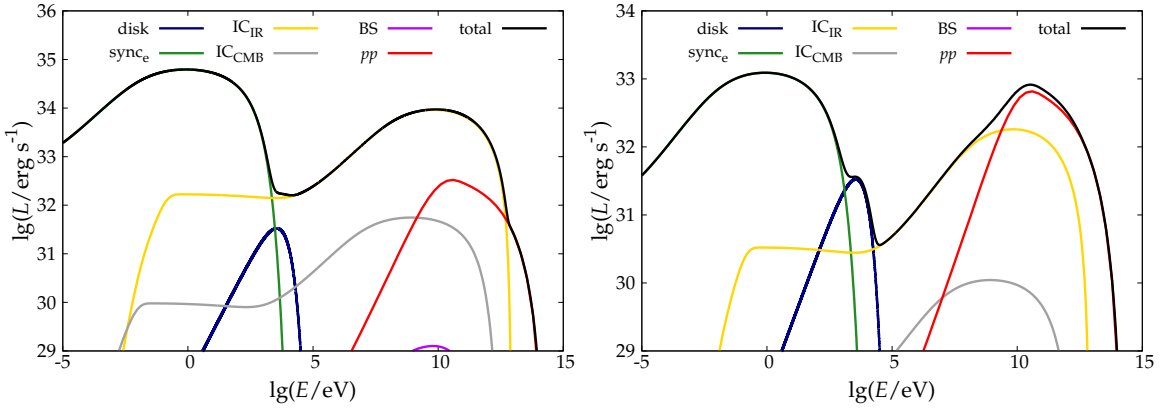

Figure 5.7: Spectral energy distribution for the model M1. *Left panel:* SED obtained with equipartition of the energy injected in electrons and protons. *Right panel:* SED assuming the power that goes into protons is 100 times the power injected in electrons.

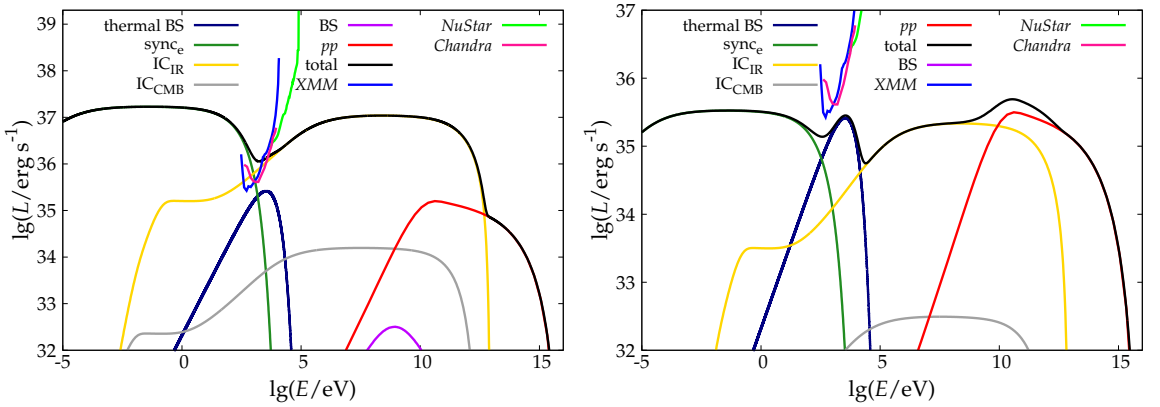

Figure 5.8: Spectral energy distribution for the model M2. *Left panel:* SED obtained with equipartition of the energy injected in electrons and protons. *Right panel:* SED assuming the power that goes into protons is 100 times the power injected in electrons. The solid lines represent the sensitivity curves of *Chandra*, *XMM-Newton* and *NuStar* for an object at the distance of NGC 253 or M82.

5.5 Discussion

Individual M1-like events produce radiation that is not large enough to be detected by current observatories even in the nearest starburst galaxies NGC 253 and M82. The evidence of clumps inside the superwinds is vast. The cloud-wind interaction models describe successfully the observed soft X-rays, as well as the optical emission and absorption lines. Nevertheless, the total number of clouds inside the superwind remains not well estimated. The velocities inferred from optical and ultraviolet (UV) lines reveal the existence of multiple clumps because they cannot be explained by the presence of a single object. Additionally, numerical simulations show that many small embedded clouds are expected. However, to obtain reliable estimates of the total number from the simulations is not possible because of the cell resolution problems (Suchkov et al. 1994; Strickland et al. 2000; Cooper et al. 2009). One way

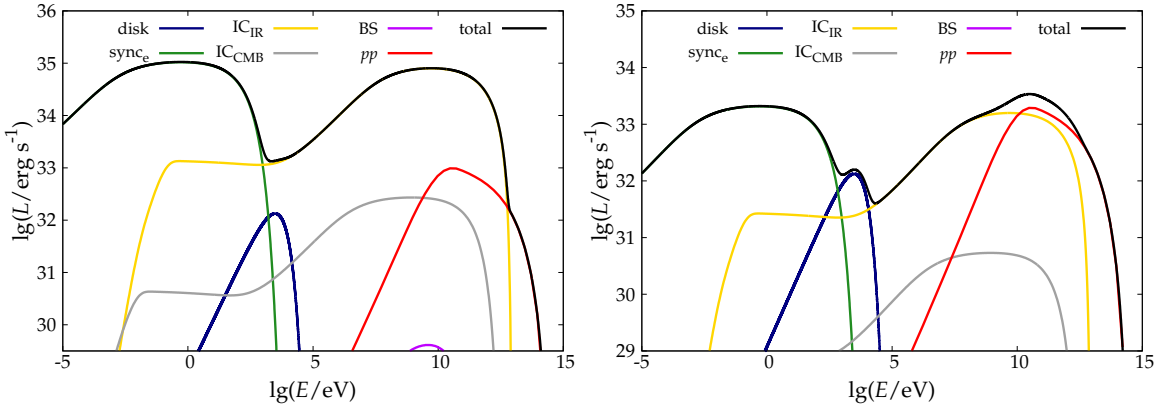

Figure 5.9: Spectral energy distribution for the model T1HP. *Left panel:* SED obtained with equipartition of the energy injected in electrons and protons. *Right panel:* SED assuming the power that goes into protons is 100 times the power injected in electrons.

to trace the embedded clouds in the diffuse hot superwind is then through the study of the O IV lines observed in the far UV spectra. In order to reproduce the O IV absorption reported by the observations, Marcolini et al. (2005) found that the required number of clouds in the line of sight ranges from 10 to 30 if the clouds have radii between 15-45 pc. Assuming a typical radius of 5 kpc for the superwind bubble and homogeneity in the distribution of clouds, we get approximately a clump density of 9 clouds kpc^{-3}. Using this cloud density, the total number of clouds becomes $\sim$ 5000. Consequently, the integrated soft X-ray luminosity produced by a cluster made up by $\sim$ 100 clouds of 5 pc radius might be detected. We also compute the SED for a cloud with R_c = 15 pc, n_c = 6×10^{-1} cm^{-3} embedded in a wind moving at 1000 km s^{-1} but with n_w = 6×10^{-3} cm^{-3}. These values correspond to the T1HP model studied by Marcolini et al. (2005). Figure 5.9 shows that, in this case, a bunch of around 10 clouds is enough to produce detectable X-ray emission. The fragmentation of larger clouds can lead to the formation of many smaller clouds, therefore, the existence of cloud clusters is reasonable.

On the contrary, a high number of large clouds is not expected inside the superwind. Consequently, the detectability of this kind of event should be discussed for individual objects and not clusters. The gamma luminosity for nearby starbursts ranges from 5 × 10^{39} to 2×10^{42} erg s^{-1} (Ballet et al. 2020). Although the SED obtained for M2 reaches its maximum in the gamma-energy band, the emission is not high enough to be resolved by the current gamma instruments. Nevertheless, a single large cloud event contributes up to $\sim$ 1% to the total gamma rays. In the same way, the contribution of 5000 M1 events result in less than $\sim$ 1% to the total gamma luminosity, whereas 5000 clouds of radius 15 pc could be the origin of up to 10% of the gamma emission of a starburst galaxy. Single M2-like events might be resolved in the future by the forthcoming Cherenkov Telescope Array (CTA) observatory, observing nearby starburst galaxies for more than 50 h.

As can be seen in Fig. 5.8, the soft X-ray radiation from large cloud events can be actually detected in a galaxy at the distance of NGC 253 or M82 (~3 Mpc; Dalcanton et al. see 2009) by the *XMM-Newton* and *Chandra* satellites if the energy injected into electrons and protons is similar. On the assumption that the energy that goes to

protons is much larger, these instruments could detect the thermal Bremsstrahlung of the bowshock instead. Point-like X-ray sources have been already observed in NGC 253 (Strickland et al. 2002; Bauer et al. 2008; Wik et al. 2014). According to our results, some of these sources could actually be bowshocks around large fragments or groups of multiple smaller clouds. Finally, the diffuse X-ray emission from the halo of NGC 253 is well fitted by a model of two thermal plasmas or a power law added to a thermal plasma. Several authors have addressed this ambiguity (see for e.g, Strickland et al. 2002; Bauer et al. 2008, and references therein), but it is still far from clear. The results obtained from our analysis show that small unresolved clumps could be part of the non-thermal component of the diffuse halo emission.

5.6 Summary and conclusions

In this chapter, we have explored the possibility of accelerating particles at the bowshocks around clouds existing inside the hot superwind of starburst galaxies. In this scenario, unlike in the large-scale shock studied in Chapter 4, the magnetic field can be amplified reaching values around 85 μG, without producing the incompressibility of the medium. The backward shocks propagating through the wind are adiabatic and strong, and consequently, particles can be accelerated by DSA there.

We ran simulations for two parameter sets in agreement with the chosen in previous works (Cooper et al. 2009; Sparre et al. 2019). Additionally, for the discussion, we presented the results corresponding to a third model based on Marcolini et al. (2005). Our results show that the cooling of the relativistic hadrons is dominated by non-radiative losses. Although the magnetic field is 10 times stronger than typical large-scale values observed in starburst superwinds, the maximum energies achieved by these particles are only 10^{15}-10^{17} eV. Nevertheless, given the low densities observed in starburst superwinds, these particles could propagate and be re-accelerated in other regions. The feasibility of this situation will be studied in a future work.

The electrons, for their part, do not propagate, but cool down locally. The losses are dominated by synchrotron radiation and IC up-scattering of IR photons coming from the central region of the starburst. If the power going to electrons and hadrons is the similar, the emission from bowshocks around large clouds could be measured by the X-ray satellites *XMM-Newton* and *Chandra*. Some of the X-ray point-like sources observed in NGC 253 and M82 could actually be emission produced in such bowshocks and the templates here presented might contribute to distinguish them from other candidate sources, such as X-ray binaries. Large cloud single events could be resolved at gamma energies by long CTA observations in the future. The radiation produced by events of small clouds can only be part of the non-thermal component of the diffuse X-ray emission of superwinds. However, clusters of tens or hundreds of clouds with radii of 5-15 pc could produce radiation large enough to be detected above the diffuse X-ray background. The existence of regions with a large number of small clouds is expected from the fragmentation of bigger clouds. Therefore, the possibility of multiple simultaneous events is plausible.

6

Particle acceleration in the broad-line region of active galactic nuclei[‡]

6.1 Introduction

Active galactic nuclei (AGNs) are basically conformed by a supermassive black hole (BH) surrounded by an accretion disk and a dusty torus (see Section 2.2.2). Some of these objects present intense broad emission lines in their ultraviolet (UV) and optical spectra (e.g., Seyfert 1), which are produced by gas contained in the broad-line region (BLR). This zone is very close to the central supermassive BH and it is thought to be formed by clouds orbiting randomly. The velocity of these clouds ranges from $10^3\,\mathrm{km\,s^{-1}}$ to $10^4\,\mathrm{km\,s^{-1}}$ (Blandford et al. 1990), whereas their typical electron number densities are between $10^9\,\mathrm{cm^{-3}}$ and $10^{13}\,\mathrm{cm^{-3}}$. The photons of the accretion disk ionize the gas of the clouds completely. As a result, about the 10 % of the radiation of the accretion disk is reprocessed by the BLR and re-emitted as line photons with a mean energy of 10 eV. The corresponding photon density is commonly independent of the luminosity and has a value of $\sim 10^9\,\mathrm{cm^{-3}}$ (Abolmasov & Poutanen 2017).

Seyfert 2 galaxies are a subclass of radio-quiet AGNs, which means that they are not specially bright radio objects. These AGNs have non-prominent relativistic jets or no jets at all. The nucleus of Seyfert 2 galaxies is seen edge-on, and consequently, it appears obscured by the dusty torus. The BLR is partially hidden, but it is revealed by spectropolarimetric observations (see e.g., Antonucci 1984; Antonucci & Miller 1985; Ramos Almeida et al. 2016). The situation remains unclear only in low luminosity Seyfert 2 nuclei, where the presence of BLRs has not been detected (Laor 2003; Marinucci et al. 2012). In the last 10 years, *Fermi* has observed gamma emission from at least three Seyfert 2 galaxies: NGC 1068, NGC 4945, and Circinus. Whereas in blazars and radio-loud AGNs most of the models attribute the gamma emission to the relativistic jet, in Seyfert 2 galaxies the origin is not well understood (see e.g., Dermer & Giebels 2016).

In the unified model, the BLR and the accretion disk coexist in the nuclear region close to the supermassive BH (see Fig. 6.1). The Keplerian movement of the clouds around the center and the evidence of infall motion of these objects (Doroshenko et al. 2012; Grier et al. 2013) should result in collisions with the disk. Many authors have investigated similar interactions of accretion disks with stars and BHs, but always

[‡]Contents of this chapter are already published in Müller & Romero (2020) https://www.aanda.org/articles/aa/pdf/2020/04/aa37639-20.pdf

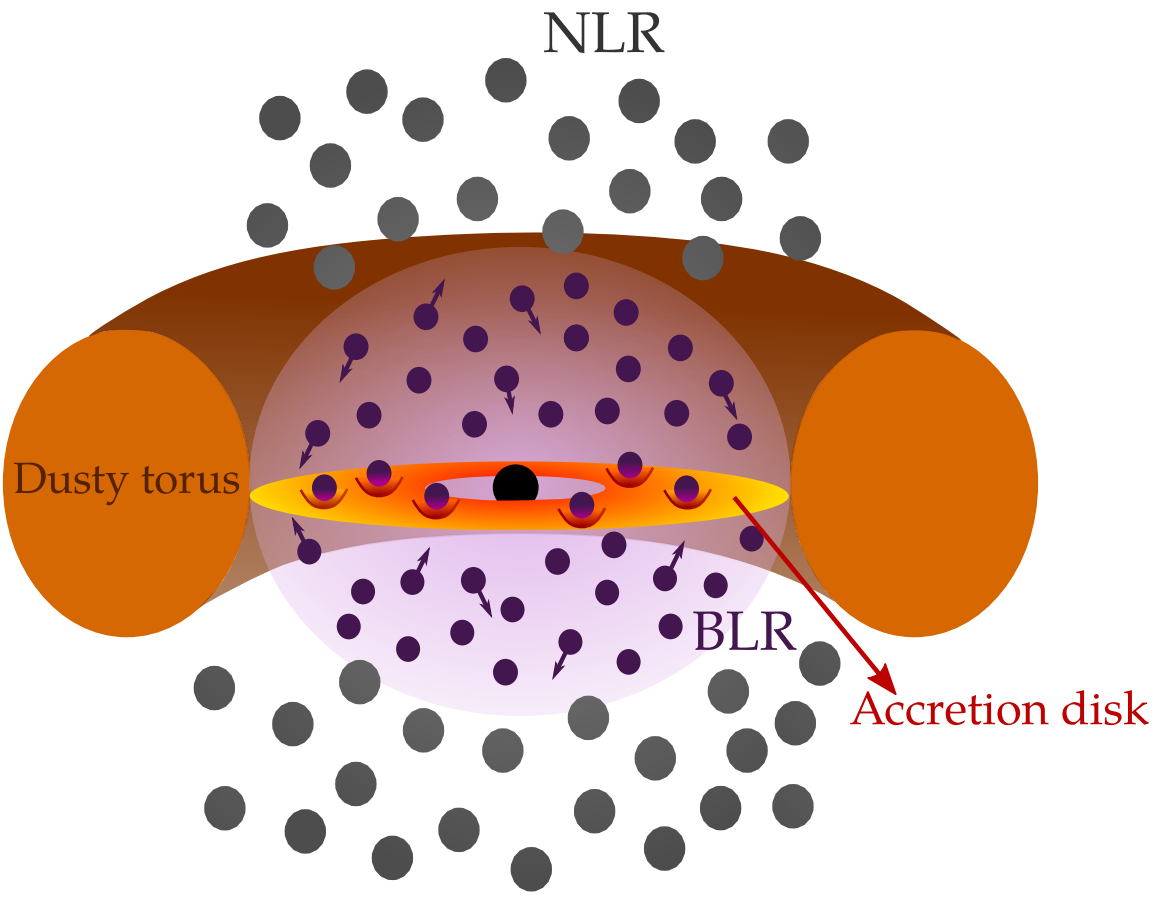

Figure 6.1: Illustrative sketch of the physical situation (not to scale). The supermassive black hole is surrounded by the accretion disk, the narrow-line region (NLR), the broad-line region (BLR), and the dusty torus. The clouds of the BLR collide with the accretion disk and produce shock waves.

putting the focus on the AGN fuelling, the thermal emission and the production of gravitational waves (Zentsova 1983; Syer et al. 1991; Zurek et al. 1994; Armitage et al. 1996; Sillanpaa et al. 1988; Nayakshin et al. 2004; Dönmez 2006; Valtonen et al. 2008).

In this chapter, we propose and investigate the acceleration of particles at shock waves produced by the impact of BLR clouds against the accretion disk. We calculate the non-thermal emission produced by the relativistic particles, in particular for the nearby Seyfert 2 galaxy NGC 1068.

6.2 Model

We start analyzing a standard AGN scenario. The supermassive BH is assumed to be a Schwarzschild BH of $10^8\,M_\odot$; for the accretion disk we adopt a Shakura-Sunayev disk (Shakura & Sunyaev 1973). The extension of the disk covers typically the space between the last stable orbit around the supermassive BH ($R_{ISCO} = 6R_g \sim 3{\times}10^{-5}$ pc) and the inner radius of the dusty torus (~1 pc). The disk model requires to define the accretion efficiency (η_{accre}) and the viscosity parameter (α_{accre}). In order to characterize it, we consider a typical value of 0.1 for both parameters (Frank et al.

2002; Fabian 1999; Xie et al. 2009). The bolometric luminosity of the AGN is set to $\sim 7\times10^{45}$ erg s^{-1}, corresponding to an Eddington ratio $\lambda_{\rm Edd} = L_{\rm bol}/L_{\rm Edd} = 0.7$. The parameters of the disk at each radius value are estimated using the expressions given in Treves et al. (1988) (see Appendix B.3).

The BLR is assumed to be formed by spherical and homogeneous clouds with average radii $R_{\rm c} = 2\times10^{13}$ cm (Shadmehri 2015). Observational works show that these clouds move in Keplerian orbits with velocities ranging from 10^3 to 10^4 km s^{-1} (Blandford et al. 1990; Peterson 1998). For our current analysis, we fix the velocity of the cloud to 5×10^3 km s^{-1}, which corresponds to a circular Keplerian orbit of radius $r = 5.40\times10^{16}$ cm = 0.02 pc. Then, the cloud impacts against the accretion disk at a distance r from the galactic center. We summarize the parameters adopted for the cloud in Table 6.1, and the physical properties of the disk at r in Table 6.2.

Table 6.1: Initial parameter values of a BLR cloud.

Parameter [units]	Value
$R_{\rm c}$ cloud radius [cm]	2.0×10^{13}
$\rho_{\rm c}$ volumetric density [g cm^{-3}]	2.2×10^{-14}
z chemical composition [$z_\odot$]	1.0
$n_{\rm e}$ electron number density [cm^{-3}]	10^{10}
$n_{\rm c}$ number density [cm^{-3}]	1.3×10^{10}
$M_{\rm c}$ cloud mass [$M_\odot$]	3.6×10^{-07}
$v_{\rm c}$ cloud velocity [km s^{-1}]	5000

Table 6.2: Values of the parameters of the central BH and the associated accretion disk in the model.

Parameter [units]	Value
$M_{\rm BH}$ [$M_\odot$]	10^8
$\lambda_{\rm Edd}$ Eddington ratio	0.70
$L_{\rm bol}$ bolometric luminosity [erg s^{-1}]	$\sim 7\times10^{45}$
r impact distance [cm]	5.40×10^{16}
$\eta_{\rm accre}$ accretion efficiency	0.10
$\alpha_{\rm accre}$ viscosity parameter	0.10
$\dot{M}$ accretion rate [$M_\odot$ yr^{-1}]	1.54
$w_{\rm d}$ disk width [cm]	2.44×10^{14}
$\sigma_{\rm d}$ superficial density [g cm^{-2}]	2.60×10^5
$\rho_{\rm d}$ volumetric density [g cm^{-3}]	1.08×10^{-9}
$n_{\rm d}$ number density†[cm^{-3}]	6.45×10^{14}
$L_{\rm disk}$ disk luminosity [erg s^{-1}]	$\sim 1.15\times10^{44}$
$T_{\rm disk}$ temperature [K]	1970.70

† Assuming a disk mainly composed of neutral hydrogen.

Broad-line regions extend typically from 0.01 to 1 pc (Cox 2000). The size can be estimated through reverberation studies (see Kaspi et al. 2007), but actually, the

result can vary up to an order of magnitude using different emission lines (Peterson & Wandel 1999). In order to produce the observed line patterns, the BLR should cover a wide range, e.g., from 10^{-3} to 0.1 pc (Abolmasov & Poutanen 2017). Subsequently, we model the BLR as a thin shell, with an internal radius r and an external one defined by $R_{\rm BLR} = \sqrt{0.1\, L_{\rm disk}/(\pi\, u_{\rm BLR}\, c)}$ (Böttcher & Els 2016), where $u_{\rm BLR}$ is the photon energy density of the BLR, $L_{\rm disk}$ the disk luminosity, and c the speed of light.

6.3 Particle acceleration and losses

6.3.1 Acceleration conditions

Given the assumed cloud velocity, it moves supersonically and its impact on the accretion disk generates two shock waves. The forward shock propagates through the accretion disk, whereas the reverse shock propagates through the cloud. All the expressions needed for the calculation of the shock velocities and the physical properties of the media are presented in Section 3.3.3.1. A similar scenario, where high-velocity clouds collide against the galactic disk were studied beforehand by several authors (see e.g., Tenorio-Tagle 1980; Santillan et al. 2004; del Valle et al. 2018).

In order to estimate the magnetic field in the region, we consider that the kinetic energy of the shocked gas $u_{\rm g}$ and the magnetic energy of the medium $u_{\rm B}$ are proportional (as we actually did in the scenario discussed in Chapter 5). The factor $\beta = u_{\rm B}/u_{\rm g}$, called magnetization parameter, should be less than one. Otherwise, the gas in the acceleration region will be magnetically dominated and strong shocks cannot exist (see e.g., Komissarov & Barkov 2007; Vink & Yamazaki 2014). With the purpose of granting the production of a shock, we adopt a modest value of 0.1 for β and calculate the magnetic field in the cloud from

$$u_{\rm B} = \beta\, u_{\rm g}$$

$$\frac{B^2}{8\pi} = 0.1\, \frac{9}{8} n_{\rm c}\, m_{\rm p}\, v_{\rm sh}^2. \tag{6.1}$$

The derived value of the magnetic field and the physical parameters of the shocked media are shown in Table 6.3.

Table 6.3: Nature of the shock and parameter values of the adiabatic media.

Parameter [units]	Cloud	Disk
$v_{\rm sh}$ [km s^{-1}]	6631	36
R_Λ cooling distance [cm]	2.5×10^{13}	9×10^{1}
Nature of the shock	adiabatic	radiative
T temperature [K]	6×10^{8}	–
B magnetic field [G]	198	–
n number density [cm^{-3}]	5.2×10^{10}	–

The results show that the shock propagating through the accretion disk is radiative. Therefore, the acceleration of particles cannot be warranted there. Consequently, we

investigate the production of cosmic rays (CRs) only in the reverse shock, which moves through the cloud. The end of the collision occurs when the shock finally traverses the total length of the cloud, which happens after $t_{\rm coll} \sim 3.4 \times 10^4$ s. Once that happens, hydrodynamic instabilities may become important and destroy the cloud (Araudo et al. 2010). Nevertheless, clouds can survive up to $\sim 4\, t_{\rm coll}$ or even longer (see Shin et al. 2008, and references therein) if they are magnetized.

6.3.2 Losses and maximum energies

As shown in the previous section, the shock into the cloud is adiabatic and the necessary conditions for the acceleration of particles by first-order Fermi mechanisms are fulfilled (see Section 3.3.3). The acceleration timescale is given by Eq. (5.17). Considering the acceleration occurs in the Bohm regime and using the velocity of the shock found previously for this scenario along with the derived magnetic field, Eq. (5.17) gives

$$t_{\rm acc} \approx 2.4 \times 10^{-10} \left(\frac{E}{\rm GeV} \right) \ {\rm yr}. \tag{6.2}$$

As mentioned in Chapter 3, the Coulomb and ionization losses can inhibit the acceleration of particles in very high-density media (O'C Drury et al. 1996). In the current scenario, it is necessary to evaluate the importance of these losses in the BLR cloud to be sure the acceleration of particles is not being suppressed by these processes. The corresponding timescales for electrons and protons are given in Eq. (3.48) and Eq. (3.49), respectively.

The injected CRs interact with the matter, photon, and magnetic fields of the cloud and lose energy. Particularly, the electrons suffer synchrotron losses due to the interaction with the magnetic field and relativistic Bremsstrahlung losses by the interaction with the ionized hot matter of the cloud. We also consider the inverse Compton (IC) up-scattering of the photons from the BLR, the accretion disk, and the synchrotron radiation (synchrotron self-Compton; SSC). The accretion disk emits locally as a blackbody of temperature $T_{\rm disk} = 1970.70$ K. Moreover, the radiation from the BLR is a monochromatic photon field with $< \epsilon >= 10$ eV and $n_{\rm ph} \sim 6.24{\times}10^{19}\,{\rm erg}^{-1}\,{\rm cm}^{-3}$. The only relevant radiative process for protons are the proton-proton (pp) inelastic collisions. All the expressions we use to calculate the cooling timescales are given in Section 3.4.

The particles can be removed from the acceleration region by diffusion. The associated timescale is presented in Eq. (3.46). In this scenario, we assume the characteristic size of the acceleration region is $X = R_{\rm c}$. Finally, since the particles release energy to expand the shocked cloud matter, we also consider the adiabatic losses (see Section 3.4). The first constraint to the maximum energy is given, as always, by the Hillas criterion $E_{\rm max} = X\, Z\, e\, B$ (see Section 3.1). The value obtained with the model parameters is $\sim 3{\times}10^{18}$ eV for protons and $\sim 8{\times}10^{19}$ eV for iron.

Figure 6.2 shows the result of the calculation of the acceleration, escape and cooling timescales. The maximum energy achieved by the electrons or protons is then inferred looking at the point where the acceleration rate equals the total loss rate. In Fig. 6.2, it can be seen that the cooling of the electrons is dominated at any energy by the synchrotron emission. Conversely, the IC losses are negligible. This result can be understood comparing the magnetic energy density $u_{\rm B} = 1.54{\times}10^3\,{\rm erg\,cm}^{-3}$ with the

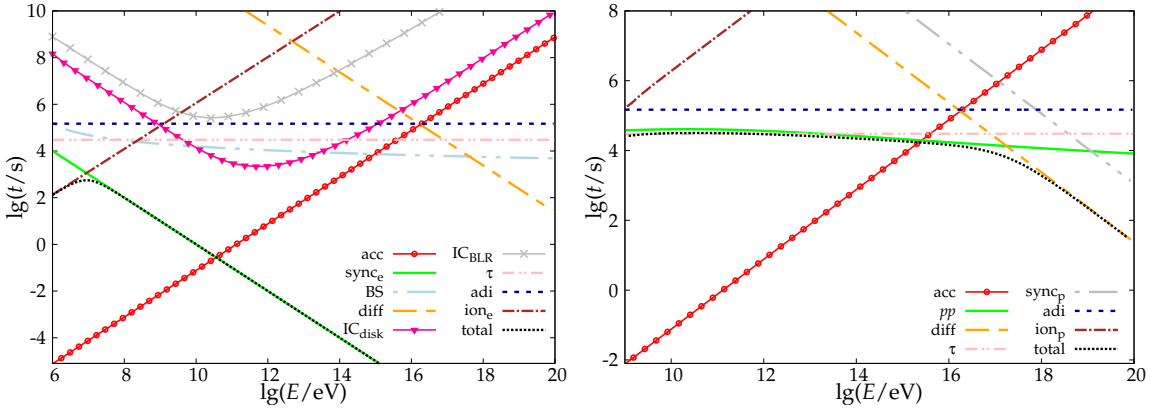

Figure 6.2: Cooling and acceleration timescales for the particles, where $\tau = X/v_{\rm sh}$ is the age of the source. *Left panel:* Electrons. *Right panel:* Protons.

blackbody radiation energy density of the accretion disk $u_{\rm disk} = 1.31{\times}10^{-1}\,{\rm erg\,cm^{-3}}$, and the photon density of the BLR $u_{\rm BLR} = 1.60{\times}10^{-2}\,{\rm erg\,cm^{-3}}$. On the other hand, the right panel of Fig. 6.2 shows that the most significant loss for the protons is the pp inelastic collisions. Consequently, we find a maximum energy $E^{e}_{\rm max} = 3.6{\times}10^{10}\,{\rm eV}$ for electrons and $E^{p}_{\rm max} = 1.5{\times}10^{15}\,{\rm eV}$ for protons. Since these values are smaller than the ones found using the Hillas criterion, they are more accurate estimations of the maximum energies of the relativistic particles.

These plots also reveal the efficiency of the cooling process. The timescales derived for the two particle types indicate that, after the end of the collision, the accelerated particles release all their energy locally before their propagation has relevant effects. Electrons cool down immediately ($\sim 3{\times}10^{2}\,{\rm s}$), whereas protons need $\sim 3{\times}10^{4}\,{\rm s}$. Actually, the timescale corresponding to the pp inelastic collisions has the same order of magnitude than the collision time $t_{\rm coll}$. Therefore, the accelerated hadrons, and the secondary particles created by them, will emit for a longer period of time than the primary leptons.

6.3.3 Particle distributions

Once again, the next step is to solve the transport equation (Eq. (3.3)) and obtain the electron and proton distributions. All the energy losses mentioned above are included in the term $b_{e,p}(E)$, whereas the escape time of the particles in this scenario is just the diffusion. The injection function is assumed to be a power law with an exponential cutoff $Q_{e,p}(E) = Q_0^{e,p}\,E^{-2}\,\exp\left(-E/E^{e,p}_{\rm max}\right)$. The spectral index 2 corresponds to the injection index observed in diffusive shock acceleration (DSA) taking place in strong adiabatic shocks (see Section 3.3.3). From Fig. 6.2 it is possible to determine that the particle distribution of electrons reaches the steady state in less than 1 s, i.e., at once, whereas the distribution of protons does the same in only $\sim 10^{4}\,{\rm s}$. For this reason, we employ the steady state solution of the transport equation given in Eq. (3.4) (see Appendix A.3), which is valid in the time interval $t_{\rm ss} = t_{\rm coll} - 10^{4}\,{\rm s} = 2.4{\times}10^{4}\,{\rm s}$.

The normalization $Q_0^{e,p}$ is found taking into account the power released in one impact, which can be obtained as $L_{\rm s} = \frac{1}{2}M_{\rm c}v_{\rm c}^{2}/t_{\rm coll}$ (del Valle et al. 2018). According to the set of parameters of our model, $L_{\rm s} = 3.9{\times}10^{40}\,{\rm erg\,s^{-1}}$. We assume that 10 % of this

energy is available to accelerate electrons and protons. In consequence, the luminosity that goes into relativistic particles in the cloud is ~3.9×10^{39} erg s^{-1}. How this power is distributed among the electrons (L_e) and protons (L_p) is unknown. Therefore, we study two situations: i) energy equally divided between the two particle types ($L_p/L_e = 1$) and ii) 100 times the energy injected in electrons to protons ($L_p/L_e = 100$). The resulting distributions are displayed in Fig. 6.3.

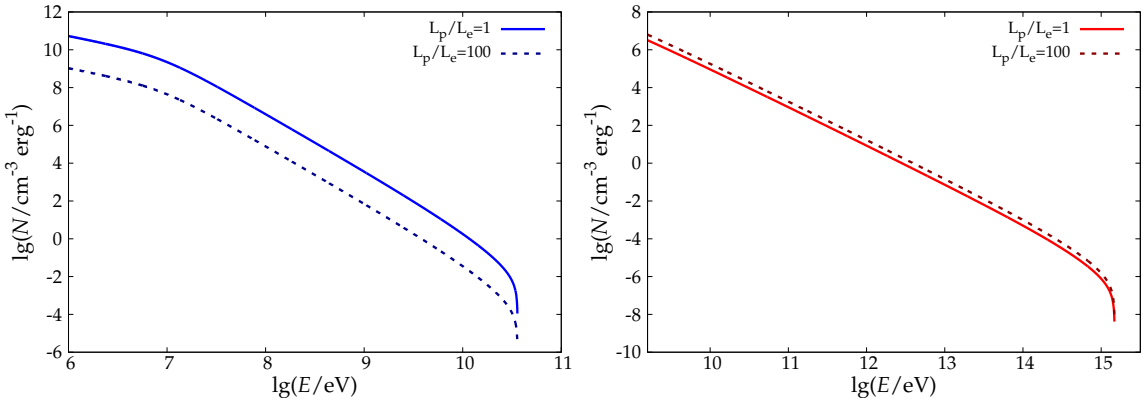

Figure 6.3: Particle distributions obtained for the electrons and protons, with $L_p/L_e = 1$ and $L_p/L_e = 100$. *Left panel:* Electrons. *Right panel:* Protons.

6.4 Results

With the particle distributions of the previous section, we compute the expected spectral energy distributions (SEDs) considering the radiative processes mentioned in Section 6.3.2 and correcting by absorption. In order to do this, the geometry of the emission and acceleration region should be defined. We suppose the emission region is a spherical cap with height X, so its volume is calculated as $V_c = \pi\, X^2\, (3\, R_c - X)/3$.

6.4.1 Radiative processes

The inverse Compton (IC) up-scattering of the BLR, the accretion disk, and the synchrotron photons are calculated using the expression provided in Eq. (3.65), whereas the relativistic Bremsstrahlung is estimated with Eq. (3.70). In the case of the synchrotron emission, we use the result given in Eq. (3.56), but corrected by synchrotron self-absorption (SSA). The effect of this absorption can be introduced by multiplying the latter expression by a coefficient $\kappa_{\rm SSA}(E_\gamma)$

$$\kappa_{\rm SSA}(E_\gamma) = \frac{1 - e^{-\tau_{\rm SSA}(E_\gamma)}}{\tau_{\rm SSA}(E_\gamma)} \tag{6.3}$$

where $\tau_{\rm SSA}$ represents the optical depth, whose form can be found in Rybicki & Lightman (1979).

The inelastic collisions of protons produce gamma luminosity. The contribution of this hadronic process is calculated following the procedure proposed by Kelner

et al. (2006) (see Eq. (3.79)). Since the focus of this work is put on the acceleration of particles up to relativistic energies and their non-thermal signature, the only thermal contribution included in our plots comes from the accretion disk (see Appendix B.3).

6.4.2 Absorption of high-energy photons and secondary particles

The gamma photons created by *pp* inelastic collisions interact with the UV photons from the BLR, and with the optical photons coming from the accretion disk. If the threshold condition $E_\gamma\,\epsilon > (m_\mathrm{e}\,c^2)^2$ is satisfied, secondary electron-positron pairs are injected. Given that the energy of the BLR photons is ϵ=10 eV, gamma rays with E_γ>30 GeV can be absorbed. In the case of the accretion disk photons, the threshold is exceeded by gamma photons with E_γ>1.5 TeV.

The total cross section for this absorption process, denominated pair production, can be found in Gould & Schréder (1967) (see Eq. (3.86)). Considering that $\epsilon \ll m_\mathrm{e}\,c^2 \leq E_\gamma$, the injection function of electron-positrons $Q_\mathrm{e}^\mathrm{sec}(E_\mathrm{e})$ can be calculated with the expressions provided in Section 3.4.3.

These secondary particles are affected by the same processes as the primary electrons. According to Fig. 6.2, the synchrotron radiation dominates essentially the cooling of electrons, whereas the other losses become negligible. Therefore, we only calculate the synchrotron emission of the secondaries.

6.4.3 Spectral energy distributions

The resulting SEDs for $L_p/L_e = 1$ and $L_p/L_e = 100$ are shown in Fig. 6.4. We note that the ratio between the proton and electron luminosities has a significant impact at the lowest frequencies (radio). In this part of the spectrum, the emission from the secondary leptons is negligible with respect to the contribution of the primaries only if the energy injected in protons is significantly less than 100 times the energy that goes to electrons. The radio luminosity we get in the case $L_p/L_e = 1$ is about a factor 10 larger than in the case $L_p/L_e = 100$.

The principal contribution in the optical region of the SED corresponds to the thermal radiation from the accretion disk. Instead, the high-energy part is non-thermal emission produced as a consequence of the acceleration of hadrons. The gamma emission originated in *pp* collisions is mainly absorbed and converted to electron-positron pairs. The large amount of secondary particles interacts with the magnetic field and radiates due to synchrotron. Their emission prevails in the energy range from 1 keV to 10 GeV, having a maximum of $\sim 10^{38}$ erg s^{-1} at around 10 keV.

The radiation originated from the impact of one BLR cloud at hard X-ray and gamma energies lies several orders of magnitude below the values typically measured in AGNs by the *Swift*, INTEGRAL, and *Fermi* satellites. Consequently, a single event is not foreseen to be observed as a flare. The very high-energy gamma-ray tail of a single collision might be detected in nearby sources in the future by the Cherenkov Telescope Array (CTA). However, the propagation of these photons through a dense visible or IR photon field (e.g., from a stellar association or the emission of the dusty torus) might lead to a strong attenuation due to absorption.

Notwithstanding all the previous issues, we note that the slope of the SED at gamma energies agrees very well with the observational data of a few galaxies like

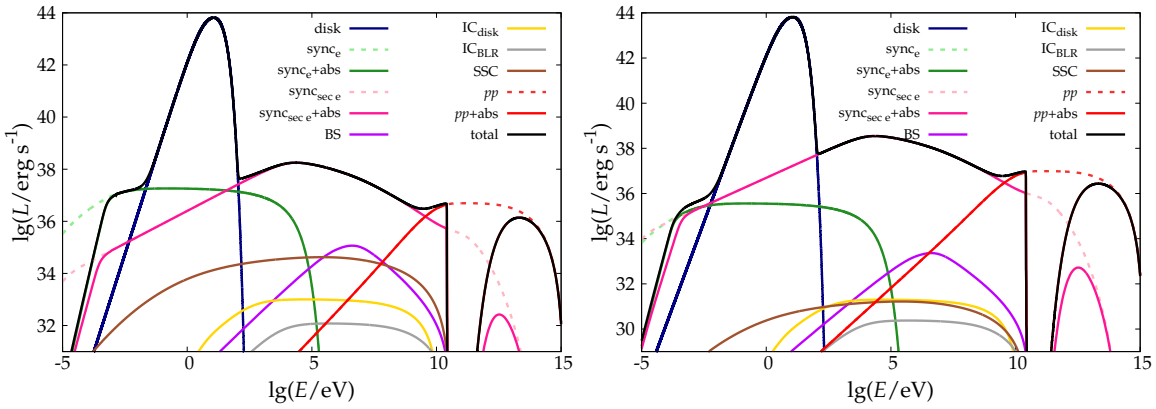

Figure 6.4: Spectral energy distributions obtained for our model. *Left panel:* SED obtained with equal power injected in protons than electrons $L_p/L_e = 1$. *Right panel:* SED obtained when the luminosity injected in protons is 100 times the luminosity that goes to electrons $L_p/L_e = 100$. The dark-blue line labeled "disk" is the thermal emission from the accretion disk.

NGC 1068, NGC 4945, and Circinus (see e.g., Ackermann et al. 2012b; Wojaczyński et al. 2015). As mentioned before, the total number of clouds in a BLR derived from the observations is quite large (~10^8 or more). Therefore, a more realistic situation requires to evaluate the existence of multiple simultaneous collisions, in which case the observable luminosity results from the sum of the luminosity of the individual events. In the next section, we apply our model to NGC 1068 and discuss the possibility of simultaneous impacts.

6.5 Application to NGC 1068

NGC 1068 is a spiral edge-on galaxy located at approximately 14.4 Mpc from the Earth, in the southern constellation Cetus (Tully 1988). In fact, it is the closest and brightest Seyfert 2 galaxy, and consequently, the most studied. In 1985, the discovery of a Seyfert 1 nucleus in the spectrum of the polarized light from NGC 1068 was the cornerstone of the AGN unified model finally proposed in 1993 (Antonucci & Miller 1985; Antonucci 1993). The bolometric luminosity of this galaxy is estimated to be ~8×10^{44} erg s^{-1} (Pier et al. 1994). Its galactic center shows AGN activity as well as very high star-formation activity, but its emission can not be completely understood with a starburst model only (Lamastra et al. 2016).

In order to apply our model to NGC 1068, we adopt the parameters provided by Lodato & Bertin (2003) (see Table 6.4). On the other hand, the cloud of the BLR is characterized with the same values given previously (Table 6.1). We assume that the total emitted luminosity arrives from multiplying the emission produced by a single impact by a number $N_{\rm events}$, which represents the average number of simultaneous events. The value of $N_{\rm events}$ is fixed requiring to match the total gamma emission reported by *Fermi* in the range from 100 MeV to 100 GeV, which is $L_{0.1-100\ \rm GeV} = (1.85\pm0.14)\times10^{41}$ erg s^{-1} (Abdollahi et al. 2020). We evaluate and discuss the validity of this assumption in the next section.

To check and constrain our model, we compare the simulated multiple-event SEDs with radio observations taken with the Very Long Baseline Array (VLBA) (Gallimore et al. 2004) and the Atacama Large Millimeter/submillimeter Array (ALMA) (García-Burillo et al. 2016; Impellizzeri et al. 2019), and the gamma-ray spectra produced with the data of the last *Fermi* catalog (8 yr) (Abdollahi et al. 2020) (see Table 6.5). It is appropriate to clarify that the VLBA and ALMA information constitute upper limits of the present model due to the fact that the reported fluxes are integrated in regions whose sizes are far larger than the region we are modeling. Furthermore, the data at 256 GHz corresponds to a region of 9.1 pc (Impellizzeri et al. 2019), whereas the spatial resolution of the observation at 694 GHz is 4 pc (García-Burillo et al. 2016). The latter implies that the thermal emission from the dusty torus, which is expected to emit around that frequency, is also included.

Based on *NuSTAR* observations, Bauer et al. (2015) suggested that the Compton-thick nature of NGC 1068 obscures even its hard X-ray emission. This scenario was recently reviewed and confirmed by Zaino et al. (2020). In consequence, the measured X-ray emission is only a fraction of the intrinsic, which is transmitted by reflections.

Table 6.4: Parameter values for the BH, accretion disk of NGC 1068, and shock properties.

Parameter [units]	Value
$M_{\rm BH}$ [$M_\odot$]	8×10^6
$\lambda_{\rm Edd}$ Eddington ratio	0.77
$L_{\rm bol}$ bolometric luminosity [erg s^{-1}]	8×10^{45}
$\eta_{\rm accre}$ accretion efficiency	0.06
$\alpha_{\rm accre}$ viscosity parameter	10^{-2}
$\dot{M}$ accretion rate [$M_\odot$ yr^{-1}]	0.235
$n_{\rm d}$ number density [cm^{-3}]	2.64×10^{16}
$L_{\rm disk}$ disk luminosity [erg s^{-1}]	1.70×10^{43}
$T_{\rm disk}$ temperature [K]	4311.82
$R_{\rm BLR}$ characteristic BLR radius [cm]	3.36×10^{16}
$v_{\rm sh}$ velocity of the shock [km s^{-1}]	6661
$t_{\rm coll}$ collision timescale [s]	3.43×10^4
$t_{\rm ss}$ steady state timescale [s]	2.43×10^4
r impact distance [cm]	4.26×10^{15}

Table 6.5: Observational data of NGC 1068.

Freq./Energy	Luminosity	Instrument
5 GHz	$(7.44 \pm 0.62) \times 10^{36}$ erg s^{-1}	VLBA
8.4 GHz	$(1.15 \pm 0.10) \times 10^{37}$ erg s^{-1}	VLBA
256 GHz	$(8.07 \pm 0.63) \times 10^{38}$ erg s^{-1}	ALMA
694 GHz	$(2.38 \pm 0.17) \times 10^{39}$ erg s^{-1}	ALMA
14 – 195 keV	$9.40^{+0.62}_{-0.53} \times 10^{41}$ erg s^{-1}	*Swift*
0.1 – 100 GeV	$(1.85 \pm 0.14) \times 10^{41}$ erg s^{-1}	*Fermi* 8 yr

For any magnetization value, we find that the case $L_p/L_e = 1$ leads to results exceeding the constraints imposed by the ALMA observations extensively whether the gamma luminosity measured by *Fermi* is fitted. Therefore, we continue hereafter our analysis only considering the ratio $L_p/L_e = 100$. Under this assumption along a magnetization of 10 % as adopted in the fiducial model (see Eq. (6.1)), the required number of simultaneous events N_{events} to match the gamma luminosity observed is ~2.8×10^3. Fixing N_{events} to this value, the hard X-ray luminosity in the range of *Swift* becomes 2.42×10^{42} erg s^{-1}, which is more than twice the flux reported in the BAT 105-Month Survey. This outcome implies that the source should be ~ 60 % obscured if there are no significant contributions from other sources in that band. However, the radio emission at 256 GHz is overestimated by about 12 % (see top panel in Fig. 6.5). In order to investigate whether higher magnetic fields improve the results, we calculate the SEDs for $B = 400$ G and $B = 600$ G. Relevant parameters and results such as the corresponding magnetization ratios, maximum energies for the particles, and the luminosity in some bands are summarized in Table 6.6 for the two scenarios. Figure 6.5 displays the associated SEDs.

Table 6.6: Parameters obtained with our model for $B = 400$ G and $B = 600$ G, constraining the number of events with the gamma luminosity.

Parameter	Magnetic field	
	400 G	600 G
β	0.40	0.90
E^e_{max}	2.6×10^{10} eV	2.1×10^{10} eV
E^p_{max}	2.9×10^{15} eV	4.3×10^{15} eV
N_{events}	1.9×10^3	1.5×10^3
$L_{256\,\text{GHz}}$	6.90×10^{38} erg s^{-1}	5.68×10^{38} erg s^{-1}
$L_{694\,\text{GHz}}$	9.55×10^{38} erg s^{-1}	7.39×10^{38} erg s^{-1}
$L_{14-195\,\text{keV}}$	1.64×10^{42} erg s^{-1}	1.25×10^{42} erg s^{-1}
$L_{0.1-100\,\text{GeV}}$	1.86×10^{41} erg s^{-1}	1.79×10^{41} erg s^{-1}

Figure 6.6 shows that in all the cases, the VLBA limit is not exceeded as consequence of the strong attenuation caused by SSA. Assuming a magnetic field $B = 400$ G, the number of events N_{events} required to achieve the total gamma emission measured by *Fermi* is 1.9×10^3, whereas with $B = 600$ G 1.5×10^3 simultaneous impacts are sufficient (see Table 6.6 and Fig. 6.7). The hard X-ray luminosity integrated between 14 keV and 195 keV is 1.64×10^{42} erg s^{-1} for $B = 400$ G, and 1.25×10^{42} erg s^{-1} for $B = 600$ G. In consequence, the source should be obscured at least between 20 % and 40 %. These percentages are actually lower limits that can be increased if other sources emitting hard X-rays exist, e.g., a corona. A corona is a compact region close to the supermassive BH typically included in AGN models. Given the high temperature of this region (~10^9 K), the soft photons from the accretion disk are converted by Comptonization to hard X-rays there (see Vieyro & Romero 2012, and references therein). The expected luminosity emitted by a corona can be similar or even up to a few of orders of magnitude higher than produced by the current scenario, in which case the obscuration percentage raises. In the particular case of NGC 1068, the presence of a corona has been suggested because of the detection of the Fe K-alpha

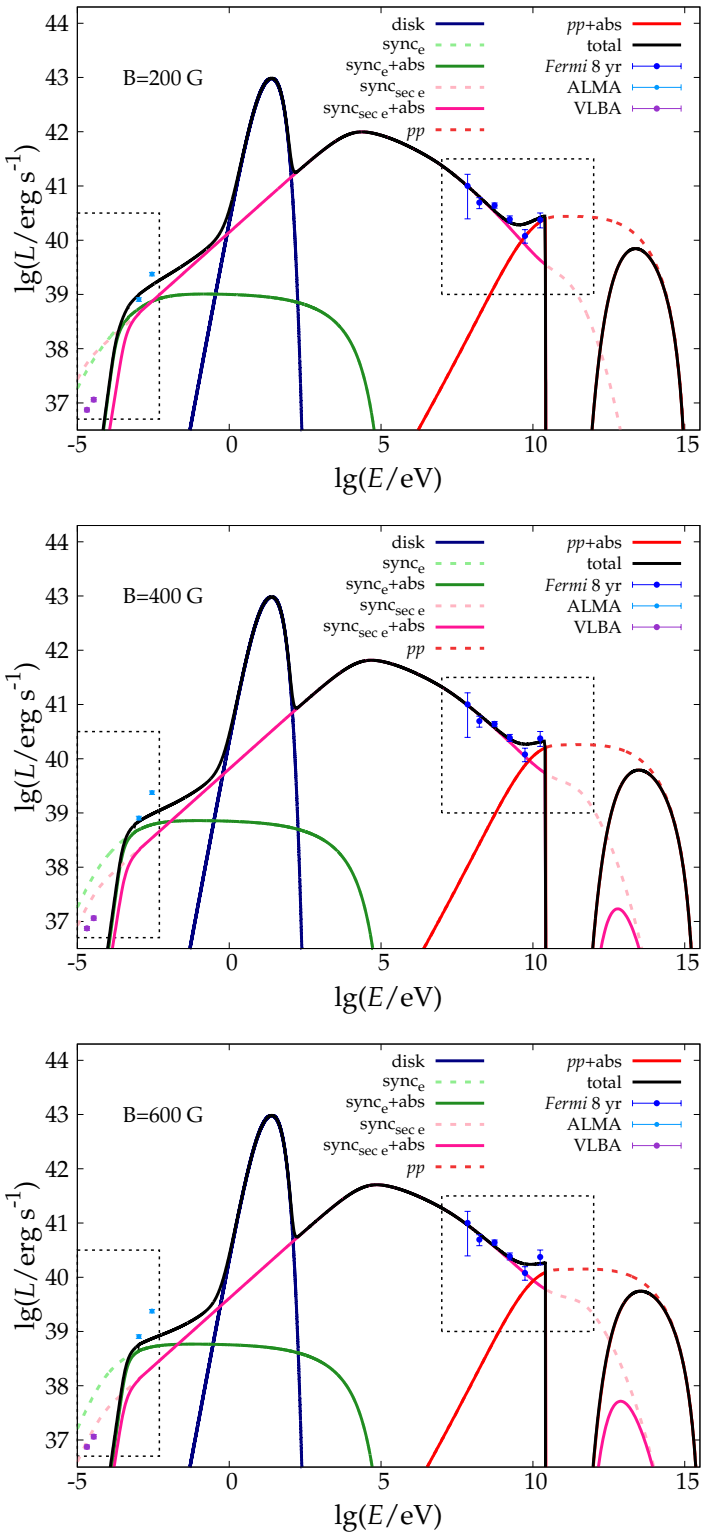

Figure 6.5: SEDs assuming $L_p/L_e = 100$. The number of cloud impacts, N_{events}, is determined by adjusting the model to match the observed total gamma luminosity. The gamma absorption is produced by the UV photons of the BLR and the optical photons from the accretion disk. The regions contained in the dashed rectangles are expanded in Fig. 6.6 and Fig. 6.7. *Top panel:* $B = 200$ G. *Middle panel:* $B = 400$ G. *Bottom panel:* $B = 600$ G.

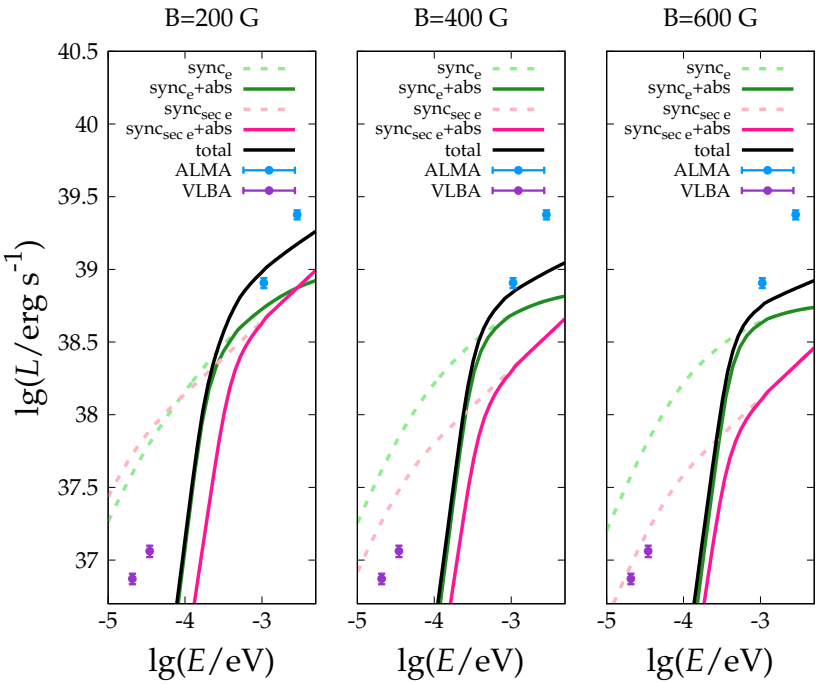

Figure 6.6: SEDs in the radio range for different values of the magnetic field assuming $L_p/L_e = 100$. The number of cloud impacts, N_{events}, is determined by adjusting the model to match the observed total gamma luminosity.

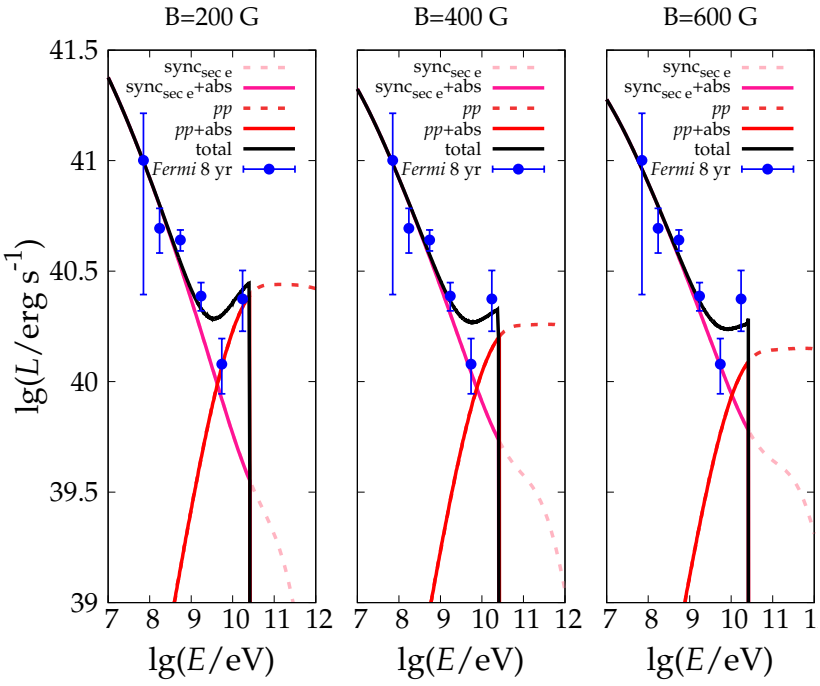

Figure 6.7: Fits of the SEDs in the gamma range for different values of the magnetic field assuming $L_p/L_e = 100$. The number of cloud impacts, N_{events}, is determined by adjusting the model to match the observed total gamma luminosity.

line, but the evidence is still not conclusive (Bauer et al. 2015; Marinucci et al. 2016; Inoue et al. 2020). Considering the magnetic field values of 400 G and 600 G, the

restriction established by the observations with ALMA are not violated (see Fig. 6.6 and Table 6.6).

6.6 Discussion

In the previous section, we suppose the existence of between $1.5{\times}10^3$ and $2.8{\times}10^3$ simultaneous BLR clouds colliding with the accretion disk. These values allow to adjust the total gamma emission observed by *Fermi*, but are they reasonable parameters? Many authors suggested that the number of clouds in a BLR should be $\sim 10^8$ or even larger (Arav et al. 1997; Dietrich et al. 1999). Abolmasov & Poutanen (2017) found that the total number could go up to 10^{18} depending on the value of the filling factor and the optical depth.

Considering the clouds uniformly distributed, the density number of clouds $n_{\rm clouds}$ can be obtained just dividing the total number of clouds $N_{\rm clouds}$ by the volume of the region $V_{\rm BLR}$. Since the BLR is assumed to be a thin spherical shell extending from r to $R_{\rm BLR}$, where $R_{\rm BLR} = \sqrt{0.1\, L_{\rm disk}/(\pi\, u_{\rm BLR}\, c)}$ (Böttcher & Els 2016), its volume can be calculated as $V_{\rm BLR} = 4/3\,\pi\,(R_{\rm BLR}^3 - r^3)$. Using the parameters of NGC 1068, the characteristic radius $R_{\rm BLR}$ is $\sim 3.36{\times}10^{16}$ cm. Then, the value of $V_{\rm BLR}$ becomes $\sim 1.5{\times}10^{50}$ cm^3 (see Table 6.4).

On the other hand, the number of collisions per unit of time is given by

$$\dot{N}_{\rm clouds} = n_{\rm clouds}\, v_{\rm c}\, \pi\, r^2 = \frac{N_{\rm clouds}}{V_{\rm BLR}}\, v_{\rm c}\, \pi\, r^2, \tag{6.4}$$

where $v_{\rm c}$ is the velocity of the impacting cloud, in our model 5000 km s^{-1}. From this rate, the number of simultaneous events $N_{\rm events}$ can be obtained as

$$N_{\rm events} = \dot{N}_{\rm clouds}\, t_{\rm ss}. \tag{6.5}$$

This means,

$$N_{\rm clouds} = \dot{N}_{\rm clouds} \frac{V_{\rm BLR}}{v_{\rm c}\, \pi\, r^2} = \frac{N_{\rm events}}{t_{\rm ss}} \frac{V_{\rm BLR}}{v_{\rm c}\, \pi\, r^2}. \tag{6.6}$$

Requiring that $N_{\rm events} = 1.5{\times}10^3$, we find that the number of clouds in the BLR should be $\sim 3{\times}10^8$. This value results compatible with the number of clouds derived from the observations.

Fluctuations in the number of simultaneous impacts will cause a proportional variation in the luminosity. Considering Poisson statistics, the characteristic fluctuation expected in the luminosity is $\sqrt{N_{\rm events}}/N_{\rm events} \sim 2.6$ %, whereas the timescale associated to this fluctuation is given by $t_{\rm ss}/N_{\rm event} \sim 16$ s (del Palacio et al. 2019). Fixing the number of events to $2.8{\times}10^3$ increases the total number of clouds in the BLR to $\sim 6{\times}10^8$, which also agrees with the observational evidence. The variability expected in this case is 1.8 % in 9 s. Consequently, for any of the magnetic field values adopted, the radiation generated by impacts of BLR clouds will be detected as continuous and our previous analysis becomes valid.

The X-ray luminosity of radio-quiet AGNs presents frequently long-term variations, usually attributed to changes in the size and properties of the AGN corona

(see e.g., Soldi et al. 2014, for a detailed discussion about X-ray variability in AGNs). The current model does not explain by itself that kind of variability, however the existence of a corona is not ruled out, nor incompatible with our scenario. Fluctuations in the measured X-ray flux from the collision of BLR clouds could be produced as a consequence of changes in the absorbers in the line of sight. The X-ray luminosity predicted by our model could vary intrinsically if strong modifications in the AGN environment occur, for instance due to a change in the accretion regime. Nevertheless, since the gamma and X-ray emission have the same origin, the gamma emission should be also affected.

One last outcome to discuss is the production of high-energy neutrinos. The inelastic *pp* collisions create not only neutral pions, but also charged. The decays of the charged pions result in neutrinos, which carry ~5 % of the energy of the relativistic proton (Lamastra et al. 2016). Given the maximum energies attained by the protons (see Table 6.6), the impact of BLR clouds might give rise to neutrinos up to 200 TeV. Consequently, the scenario presented in this chapter might be source of neutrinos in the detection range of IceCube, contributing to the spectrum reported by IceCube Collaboration et al. (2019).

6.7 Summary and conclusions

In this chapter, we suggested that particles can be accelerated in shocks developed by the collision of BLR clouds against the accretion disk in AGNs. We proposed that electrons and protons gain energy by DSA. Depending on the strength of the magnetic field, electrons can reach energies up to 36 GeV, whereas the maximum energy of protons rises to ~4 PeV. These maximum energies are limited by the cooling processes suffered by the particles. Since the magnetic fields deduced are highly strong, the synchrotron radiation dominates the cooling of the electrons, whereas the large density of the clouds causes that the *pp* interactions leads the cooling of the protons. The corresponding timescales are extremely short, hence the charged particles cool down locally before they escape the source. The maximum energies achieved by the protons in this scenario allow the production of neutrinos with energies in the detection range of IceCube.

The luminosity we obtained for a single event cannot be detected as a flare, but the emission resulting of the sum of many simultaneous collisions is consistent with the measured gamma radiation of NGC 1068 if its Compton-thick nature screens at least between 20 % and 40 % of the hard X-ray flux. The photons of the BLR and from the accretion disk interact with the high-energy photons created in *pp* inelastic collisions. Consequently, the gamma photons with the higher energies are absorbed and converted to secondary electrons. These secondary particles interact with the strong magnetic field and emit synchrotron radiation in the detection range of the *Fermi* satellite.

The number of simultaneous events required to account for the observed gamma rays ranges from 1.5×10^3 to 2.8×10^3, depending on the magnetic field considered; weaker magnetic fields need a larger amount of events. Such numbers of impacts are feasible as long as the total number of clouds existing in the BLR is between 3×10^8 and 6×10^8. These quantities result in good agreement with the observational

evidence provided by spectral analyses of BLRs. The number of impacts is expected to fluctuate in time. However, the effect of these fluctuations cause a variability of the luminosity small enough to be detected.

All in all, this chapter presents an interesting alternative to explain the high-energy emission in AGNs deprived of powerful jets. Further observations employing the next generation of X-ray and gamma satellites (e.g., *ATHENA*, the sucessor of *e-ASTROGAM*; Barcons et al. 2017; Rando et al. 2019) might provide valuable information to validating and distinguishing our model from other possible scenarios (e.g., Murase et al. 2019; Lamastra et al. 2019; Inoue et al. 2020).

7

Discussion

The observational evidence has reiteratively pointed to starburst galaxies as the most feasible sources for producing the cosmic rays (CRs) with the highest energies (see Chapter 2). The ideas of accelerating particles up to relativistic energies in these astrophysical environments are not new. Indeed, CRs gain energy due to the star-formation activity occurring inside regular galaxies such as the Milky Way. Therefore, it is expected that the same injection happens to a greater extent in starburst galaxies as a consequence of the larger star formation rates (SFRs). Nevertheless, to reach ultra-high energies is not trivial, because to multiply the number of sources producing particles at most up to 10^{17} eV does not increase the maximum energies.

The mass composition analysis performed by the Pierre Auger Observatory (Auger) shows that the ultra-high energy cosmic rays (UHECRs) seem to be mainly intermediate-mass nuclei, and consequently, the accelerators should be located in metal-rich places such as star-forming regions. Invoking diffusive shock acceleration (DSA), the acceleration timescale results in $t_{\rm acc}^{\rm DSA} \propto Z^{-1}\,(D/D_{\rm B})\,V_{\rm sh}^{-2}\,B^{-1}\,E$, where D is the diffusion coefficient ($D_{\rm B}$ is the coefficient in the Bohm regime), $V_{\rm sh}$ is the shock velocity, and B is the magnetic field strength (see Chapter 3). Then, fast shocks, diffusion close to Bohm, and large magnetic fields are preferred for having a more efficient acceleration, i.e., a shorter acceleration timescale. On the other hand, accelerating nuclei requires also to avoid the more common energy losses: the accelerator should be placed in a region with a low density of matter and photon fields. Additionally, the size of the region should be large enough to ensure that the particles remain there sufficient time to achieve ultra-high energies. All these conditions have been suggested to be satisfied in the superwind powered by the intense formation of stars in starburst galaxies (Anchordoqui et al. 1999). The production of UHECRs in the large-scale superwinds has been one of the most promising models for many years. Nevertheless, the analysis performed in Chapter 4 indicates that, with realistic parameters derived from observations, the particles do not manage to reach energies above the ankle. The observational and theoretical constraints do not leave a large combination of allowed parameter sets to explore. Even considering larger magnetic field values requires to increase simultaneously the density of the medium to guarantee the shock conditions. As a consequence, the energy losses due to the interaction with matter become more efficient reducing the final maximum energies. Either, we proved that stochastic diffusive acceleration (SDA) does not explain the energies of about 10^{20} eV. In Chapter 5, we demonstrated that such energies are also not achieved in regions inside the superwind where the magnetic field can be strongly amplified. The natural question becomes, what happens if the correlation

between the arrival directions of UHECRs and starburst galaxies keeps increasing its significance. In the next sections, we discuss some possible scenarios.

7.1 Starbursts

The results found in Chapters 4–5 indicate that the acceleration of particles up to ultra-high energies is disfavored to occur in the superwind of starburst galaxies. If future analyses show a stronger correlation with these sources, a new opportunity for superwinds can only arise from observations performed with the next generation of telescopes revealing that the parameters derived from the current data were not so realistic. Nevertheless, to find, e.g., twice or thrice faster shocks, magnetic fields 10 times higher, or starbursts with lifetimes largely above 10^8 yr seems to be very unlikely, since the actual observational information is quite robust, and to reach ultra-high energies requires a modification of more than one of these values simultaneously. Therefore, further starburst studies might investigate alternative sources or acceleration mechanisms.

Given the high SFR observed in starburst galaxies, low-luminosity gamma-ray bursts (see e.g., Murase et al. 2008; Zhang et al. 2018), trans-relativistic supernovae (see e.g., Chakraborti et al. 2011; Zhang & Murase 2019), hypernovae (see e.g., Liu & Wang 2012), young pulsars (see e.g., Fang et al. 2012b), and tidal disruption events (see e.g., Farrar & Piran 2014) might occur there frequently. These sources are supposed not only to achieve the energies, but also to explain the observed flux of ultra-high energy particles (Alves Batista et al. 2019). Nevertheless, each of these candidates requires further theoretical and observational studies in order to clarify its rate, the operating mechanisms, or its local properties. In the particular case of low-luminosity gamma-ray bursts, trans-relativistic supernovae, and hypernovae the data provided by neutrino and gravitational wave experiments can be very helpful (van Putten et al. 2019).

Alternatively, UHECRs could be produced in starburst galaxies by re-acceleration mechanisms. To accelerate particles up to ultra-high energies by DSA is somehow challenging. This is a consequence of the efficient diffusion needed to raise the energy of the particles, which enhances at the same time the escape of the CRs before they gain enough energy. As mentioned in Chapter 3, Caprioli (2015) proposed a re-acceleration mechanism capable of producing UHECRs in jetted active galactic nuclei (AGNs). This process cannot be applied directly to starburst galaxies. Nonetheless, some re-acceleration could be generated as a result of the collective effects of the extreme events taken place in the star-forming region. Some less efficient models have already been suggested in the context of OB stellar associations (see e.g., Bykov et al. 2020).

7.2 Starbursts?

Another question that should be addressed is whether the sources classified as starbursts are actually starburst-dominated or not. As mentioned in Chapter 2, there is no full consensus about how to define a galaxy as starburst. Moreover, the discussion is motivated by the fact that some of the sources are simultaneously cataloged as another type of galaxies, as in the case of NGC 1068 and NGC 4945. In Chapter 6

we showed that the gamma emission from NGC 1068 can be completely described by a process related with its AGN activity. The ambiguity of the properties of these objects has been also noted by other authors. Lenain et al. (2010) mentioned that the gamma emission from NGC 1068 is larger than the predicted by the starburst models, suggesting that an AGN component should be included. Indeed, all the models that explain the radiation from this galaxy account for the AGN component (Yoast-Hull et al. 2014; Eichmann & Becker Tjus 2016; Lamastra et al. 2016). Wojaczyński et al. (2015) found that the gamma radiation from NGC 1068, NGC 4945, and Circinus correlates with the properties of the respective AGN. Additionally, some of the same authors reported a few years later a correlation between the X-ray emission and the gamma luminosity of NGC 4945, which can be interpreted as the AGN component dominating over the starburst at gamma energies (Wojaczyński & Niedźwiecki 2017).

Variability in the GeV gamma emission from NGC 3424 and UGC 11041, two starburst galaxies, has been recently reported. Consequently, the emission was suggested to have its origin in the AGN of these objects (Peng et al. 2019). A pair of galaxies exceeding the starburst predictions was also found by Ajello et al. (2020), who revisited the far-infrared-gamma relation established by Ackermann et al. (2012b) for star-forming galaxies. In the new analysis, NGC 3424, reported by *Fermi* as a starburst galaxy, and NGC 2403, reported as a candidate, are outliers of the empirical correlation (see Fig. 7.1). If the origin of the far-infrared and the gamma radiation is the star-formation activity, both energy bands are expected to correlate with each other because of their intrinsic dependency on the SFR. However, determining the SFR from the infrared luminosity assumes that the ultraviolet (UV) radiation generated by the stars is totally absorbed and re-emitted as infrared emission (Kennicutt 1998b; Ackermann et al. 2012b), which is not true for systems with an incomplete obscuration (Kennicutt & Evans 2012). After studying the biases of using the far-infrared emission as SFR indicator, Kornecki et al. (2020) found that NGC 4945 and NGC 3424 become outliers of the gamma ray-SFR relation.

The correlation analysis of arrival directions performed by Auger takes into account different sets of sources emitting at different wavelengths. The particular case of non-jetted AGNs is studied, but weighting the expected production of CRs with their hard X-ray emission. In Chapter 6 we discussed that actually, the radiation from NGC 1068 seems to be obscured because of its Compton-thick nature even at hard X-ray energies. The observational evidence suggests that the situation with NGC 4945 is similar, but with a strong X-rays absorption only below 10 keV. At hard X-ray frequencies, the source has been reported to be variable, meaning that the estimation of its power through such luminosity is perhaps inaccurate (Caballero-Garcia et al. 2012). The problem of the unknown absorption in these sources could affect the interpretation of the gamma radiation (Ackermann et al. 2012a). Given the many observational similarities between Seyfert 2 galaxies and starburst galaxies, the lack of variability in gamma rays has been adopted as an indicator of GeV emission from star-forming origin. Nevertheless, a mechanism similar to the one proposed in Chapter 6 can produce a non-variable gamma-ray flux, which can be compatible with hard X-ray variability if a corona contribution exists and is larger than the broad-line region clouds component.

Further analyses are necessary to clarify the phenomenons taking place in starburst galaxies and AGNs. Observational information provided by the forthcoming

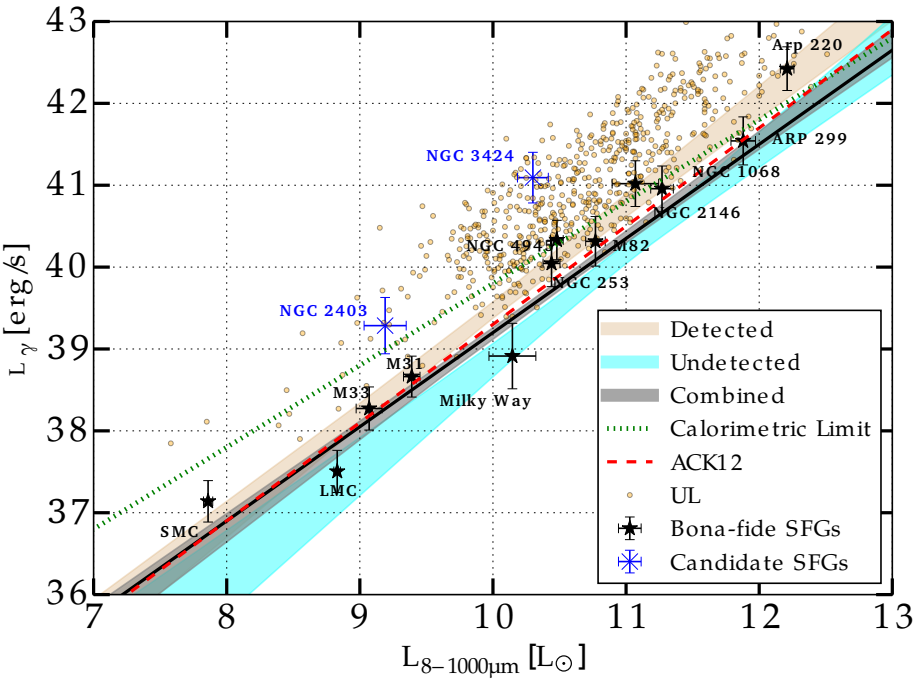

Figure 7.1: The plot shows the best fit for the far-infrared-gamma emission found by Ajello et al. (2020), using 10 yr of *Fermi* data. The red dashed line indicates the previous best fit found by Ackermann et al. (2012b) using 3 yr of data, whereas the black solid line is the new best fit, only based on the bona-fide objects. The open symbols are the upper limits for the non-detected objects. Taken from Ajello et al. (2020).

TeV and MeV experiments can help to constrain the models (see e.g., Lamastra et al. 2019; Wang & Fields 2018). The results of this thesis indicate that the non-thermal emission of the sources can be understood even in absence of UHECRs. Therefore, theoretical studies are needed to understand whether the bulk of lower energy CRs, responsible for the observed gamma and radio emission, and the UHECRs are accelerated at the same places or not. If the highest energies are a consequence of a re-acceleration process, an alternative weighting strategy for the expected UHECR contribution should be thought of. Rieger (2019) has also suggested that the evolution of the source could be important to explain the UHECR flux from Centaurus A. Therefore, the possible connections between starbursts and AGNs should be explored (see e.g., Alexander & Hickox 2012) to understand whether the high-energy particles originate from one of the two processes or from the combined effect. Another condition important to note is that several candidates within the hot spot of Auger are gravitationally bounded, forming a galaxy group (Fouque et al. 1992). This issue could induce the large-scale medium to have peculiar properties, which could be a relevant ingredient for the acceleration of the particles. Along with the rise of the collected events, the upgrade of Auger plans to improve the knowledge regarding the mass composition of UHECRs. These data will contribute in the forthcoming years to constrain the relevance of the magnetic fields in the arrival direction analysis, as well as the properties of the sources required to explain the detected fluxes.

8

Summary and conclusions

This thesis focuses on three different scenarios, two in starburst galaxies and one in active galactic nuclei (AGNs), where particles can be accelerated up to relativistic energies. These particular objects are promising candidates as ultra-high energy cosmic ray (UHECR) sources because of the large amount of energy released by extreme processes occurring in their environments. Furthermore, these places are expected to contain abundant heavy nuclei, which are compatible with the reported composition of the particles at the highest energies.

First, we revisited the model proposed by Anchordoqui et al. (1999) where particles are accelerated by diffusive shock acceleration (DSA) in the large-scale shocks created by the superwinds in starburst galaxies. Besides, we included the possibility of acceleration via stochastic diffusive acceleration (SDA) in the very turbulent plasma of the galactic outflow, whose relevance was not previously studied. We applied the model to the nearby starburst NGC 253, characterizing the superwind region with the parameters derived from the observational data collected by the radio, X-ray, and gamma-ray telescopes over the last 20 years. We found that the conditions yield maximum achievable energies of about 10^{18} eV, which are more modest results than the ones originally claimed. Reaching higher energies in a superwind with such properties seems to be very unlikely. The small magnetic field, along with the large mass carried by the wind, drops the acceleration efficiency. Simultaneously, the SDA is disfavored by the slow velocities of the Alfvén turbulence in the plasma. Nevertheless, the calculated gamma emission accounts for the total radiation measured by the *Fermi* satellite and High Energy Stereoscopic System (H.E.S.S.).

Motivated by the idea of examining regions where the magnetic field can be amplified, we investigated the bow shocks developed around denser regions inside the superwind. These clouds are formed by matter of the disk swept-up by the galactic outflow. Bow shocks are formed as a consequence of the impact of the supersonic wind against the inhomogeneities. The magnetic field might be amplified locally because of the large difference of densities between the cloud and the wind. For our analysis, we chosen two sets of parameters according to hydrodynamical simulations performed by other authors. This election ensures that the bow shock-cloud system survives enough time to allow the particles to gain significant energy. We found that the convection removes the protons of the acceleration region quickly, preventing those particles to reach energies higher than 10^{17} eV. Contrarily, the electrons cool down before they can escape the bow shock. If the size of the cloud is large enough and the energy injected in protons does not exceed largely the energy going to electrons, the emission produced by the electrons agrees with some of the X-ray

sources detected by *Chandra* and *XMM-Newton* in the halos of the starburst galaxies M 82 and NGC 253. The gamma radiation from the bow shock around big clouds might be observed in the future by Cherenkov Telescope Array (CTA). The photon flux generated by the interaction of the wind with a single small cloud is not large enough to be resolved. Therefore, such emission only contributes to the non-thermal diffuse X-ray radiation of the superwind. The integrated radiation of a bunch of tens or hundreds of small clouds, created by the fragmentation of larger clouds, could be also distinguished above the background of non-resolved sources.

Finally, we investigated the acceleration of particles in an AGN. We proposed that the acceleration takes place in the shock produced by the collision of a broad-line region cloud with the accretion disk. Broad-line region clouds orbit in a region very close to the supermassive black hole. The high velocity of these objects and the large density of the disk leads to the creation of strong fast shocks where particles can be accelerated by DSA. Additionally, the properties of the system permit magnetic fields with large values without falling into a magnetically dominated regime, in which the shocks are prevented from existing. We applied the model to the nearby Seyfert galaxy NGC 1068. Our results showed that protons can be accelerated up to $4{\times}10^{15}$ eV, as a consequence of the severe conditions of the medium. Moreover, the particles cannot escape from the acceleration region and cool down locally. Protons lose all their energy by proton-proton inelastic collisions, creating neutral and charged pions. The charged pions might produce neutrinos in the working range of IceCube. The gamma photons generated by the decay of neutral pions are highly absorbed by the ultraviolet radiation of the broad-line region. As result, electron-position pairs are injected. Those secondary particles emit most of their energy as synchrotron radiation. The photon flux produced by a single collision is not large enough to be detected by any current instrument. Nevertheless, the impact rate predicts multiple simultaneous events, whose integrated luminosity is consistent with the total emission observed by the *Fermi* satellite. Our model also suggests that the Compton-thick nucleus of NGC 1068 might be between 20 % and 40 % obscured.

According to the outcomes of the analyses performed, we conclude that the production of UHECRs in the superwind of starburst galaxies is disfavored. If ultra-high energy particles are accelerated there, other sources such as hypernovae, gamma-ray bursts, or young pulsars are more likely. On the other hand, the AGN model points out that the gamma emission of NGC 1068 can be explained in terms of its AGN activity without predicting any large variability in the flux. This result suggests that variability can be an ambiguous discriminator between star-forming and AGN emission. To identify the sources of UHECRs requires not only to improve the statistic by collecting more events, along with a better characterization of their mass-composition, but also deeper theoretical and multi-messenger works concerning the candidate sources. The disentanglement or the proof of a solid connection between starbursts and AGNs might help to find how and where particles are accelerated up to the highest energies. To resolve gamma-emitting regions in the nearby starbursts will clarify the cosmic ray production sites, along with the detection or not of more TeV galaxies. Some of these questions are expected to be answered by the next generation of electromagnetic telescopes such as CTA, *eASTROGAM*, *AMEGO*, *ATHENA*, SKA, E-ELT, among others, together with the upgraded Pierre Auger Observatory, Telescope Array Project, and IceCube.

List of Figures

List of Tables

A

Coding notes

This appendix includes explanations and remarks that can be useful to code the expressions presented in Chapter 3. Its content is the result of discussions with colleagues, students, and my own debugging/coding experience. Therefore, the reader should take these notes as an starting point to deal with common problems, but always appeal to qualified texts in the matter.

A.1 Numerical integration

The study of astrophysical situations mainly requires to solve integrals. The complexity of the integrands makes the numerical methods the preferred ones to address these problems. Nevertheless, numerical solutions should also consider that the characteristic length of the intervals of integration tend to be of several orders of magnitude; see e.g., Eq. (3.56) where $E^e_{\rm min}$ and $E^e_{\rm max}$ adopt typical values like 10^6 eV and 10^{12} eV, respectively. This situation, along with the natural power-law or exponential description of many physical phenomena, leads to the fact that working in the logarithmic scale becomes a more accurate approach.

Let us assume that we are interested in solving the following integral

$$S = \int_A^B f(x)\, dx. \tag{A.1}$$

The most simple numerical solution is obtained dividing the function in a number N of intervals and approximating the result of the integral with the sum of the areas of the rectangles defined by the widths of the intervals and the value of the function at the left-end interval points, as illustrated in Fig. A.1. This method is known as left Riemann sum[1] and its solution can be written as

$$S = \int_A^B f(x)\, dx \approx \sum_{i=1}^{N} f(x_i)\, \Delta x, \tag{A.2}$$

where the accuracy of the result depends essentially of the choice of Δx [2]. In the most standard case, $h = (B - A)/N$, $x_{i+1} = A + i\, h = x_i + h$, and $\Delta x = x_{i+1} - x_i = h$. Nonetheless, choosing a constant step in the linear scale for power-law-like integrands is not recommended.

[1] Right Riemann sum and Midpoint sum are analogously defined.
[2] Smaller Δx improve the result but rise the computing time.

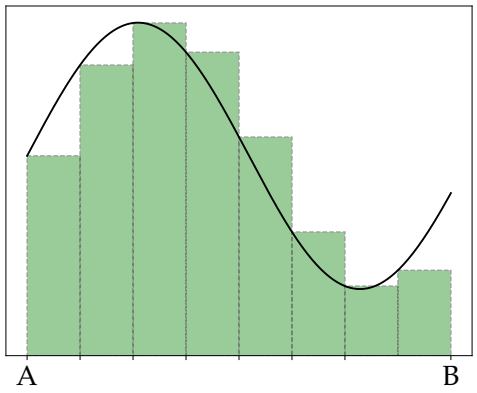

Figure A.1: Scheme of the left Riemann sum of an arbitrary function. The green rectangles represent the approximated value adopted in each interval, considering N intervals with a width $\Delta x = h = (B - A)/(N - 1)$ each.

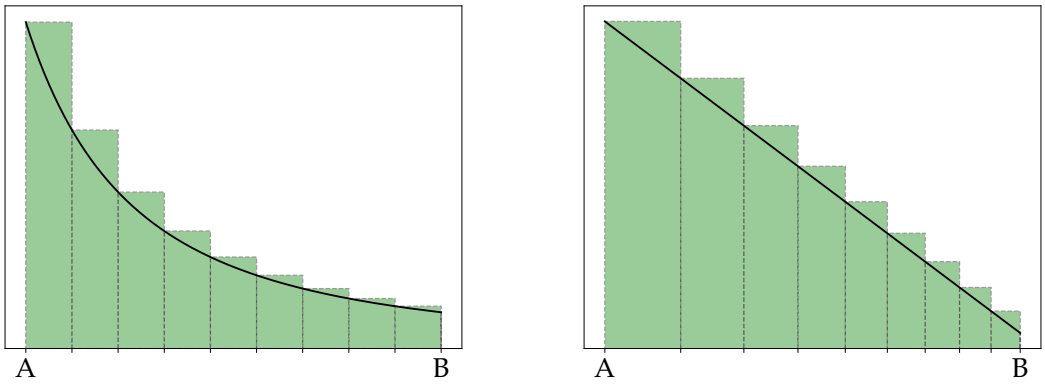

Figure A.2: Scheme of the integral of the function $f(x) = x^{-2}$ between A and B using the left Riemann sum. The green rectangles represent the approximated value adopted in each interval, considering N intervals with a width $\Delta x = h = (B - A)/(N - 1)$ each. *Left panel:* Linear scale. *Right panel:* Logarithmic scale.

Let us suppose $f(x) = x^{-2}$. Fixing $\Delta x = h = (B - A)/(N - 1)$ we find that the value of the integral becomes largely overestimated. Overestimation is expected if the function is monotonically decreasing, but the numerical estimation in this particularly case is difficult to improve as a consequence of the form of $f(x)$. The left panel of Fig. A.2 shows that the larger errors occur on the firsts intervals, whose contributions to the integral are important. This situation is even more evident in the right panel of Fig. A.2 which displays the same plot but in logarithmic scale. Adopting greater values of N will produce a better sampling at values closer to B, but no significant change at values close to A. The use of large N values can be avoided defining Δx as constant in logarithmic scale, which results in a variable step in linear scale.

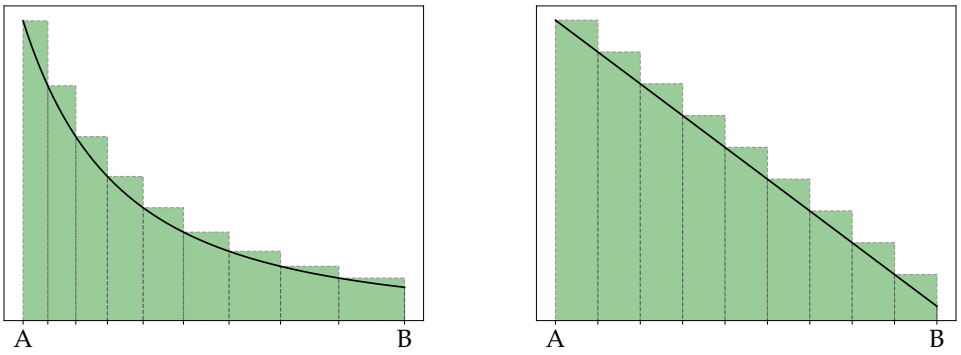

Figure A.3: Scheme of the integral of the function $f(x) = x^{-2}$ between A and B using the left Riemann sum. The green rectangles represent the approximated value adopted in each interval, considering N intervals with a width $\Delta x = x_i(h-1)$ each. *Left panel:* Linear scale. *Right panel:* Logarithmic scale.

One way to set a constant step h in logarithmic scale is

$$\log(h) = \frac{\log(B) - \log(A)}{(N-1)}. \tag{A.3}$$

Using the properties of logarithms

$$\log(h) = \log\left[\frac{B}{A}\right]^{1/(N-1)}, \tag{A.4}$$

and $h = [B/A]^{1/(N-1)}$. Then, $\log(h) = \log(x_{i+1}) - \log(x_i)$, and $x_{i+1} = h\, x_i$. Therefore,

$$\Delta x = x_{i+1} - x_i = x_i\,(h-1). \tag{A.5}$$

The improvement of the result using this step proposal is illustrated in Fig. A.3.

The result of the approximated value can be simply refined in monotonically functions replacing the left Riemann sum by the trapezoidal rule. The main idea of this estimation is the same as in the left Riemann sum, but calculating the integral value on each interval as the area of a trapezoid instead of a rectangle. The trapezoidal solution can be then written as

$$S = \int_A^B f(x)\,dx \approx \sum_{i=1}^{N-1} \frac{f(x_{i+1}) + f(x_i)}{2}\,\Delta x, \tag{A.6}$$

where the recommended choice for Δx is again the given by Eq. (A.5). A coding example of both methods is presented below.

A.1.1 Left Riemann sum with a constant logarithmic step. Fortran.

```
1  h = (B/A)**(1.d0/(N-1))
2  x = A
```

```
integral = 0.d0

DO i = 1,N
    arg = f(E)
    dx = x*(h-1.d0)
    integral = integral + arg*dx
    x = x*h
END DO
```

A.1.2 Trapezoidal rule with a constant logarithmic step. Fortran.

```
h = (B/A)**(1.d0/N)
x = A
integral = 0.d0

arg1 = f(x)
DO i = 1,N
    arg2 = f(x*h)
    arg = (arg1 + arg2)/2.
    dx = x*(h-1.d0)
    integral = integral + arg*dx
    x = x*h
    arg1 = arg2
END DO
```

A.1.3 Python comments

The same routines can be adapted and used in Python.

```
h = (B/A)**(1./(N-1))
x = A
integral = float()

for i in range(0,N):
    arg = f(x)
    dx = x*(h-1.)
    integral += arg*dx
    x = x*h
```

Alternatively, Python contains some intrinsic tools, such as the Gaussian quadrature method, included in the *scipy* package, and some integration methods, such as the trapezoidal rule, included in *numpy*. Here a few lines of example code

```
import scipy.integrate as integrate

integral = integrate.quad(f, A, B)
```

```
import numpy as np

# the next line produces a grid in the logarithmic space
x = np.logspace(np.log10(A), np.log10(B), N)

h = x[1]/x[0]

y = f(x)

integral = np.trapz(y, x, dx = h)
```

In the first case, the input is the function f, whereas the second case integrates based on arrays of values.

A.2 Tests and bugs

When we are trying to produce a code capable of solving equations, it is very common to forget that we are facing a physical problem and not a mathematical one. Therefore, it is always important to check that we are only running on values with a physical meaning. For instance, the cross sections of the processes described in Chapter 3 have implicitly associated a Heaviside function, which allows them to have a value different from zero only above some energy threshold. Nonetheless, these cross sections appear typically inside integrals whose lower limit can be a number smaller than the energy limit. The same situation happens with the integrals containing the particle distribution $N(E)$, which is different from zero only for values between $E_{\rm min}$ and $E_{\rm max}$ (see e.g., Eq. (3.70)). Consequently, if the programmer forgets to indicate that the integrand is zero for energies below all the thresholds, the code will provide a wrong result.

Another common problem arises from evaluating functions in values too close to a non-allowed one. This issue can occur using expressions such as Eq. (3.67) or Eq. (3.80). In the first case, if E and E_γ adopt similar values, the calculation of $\ln(E - E_\gamma)$ diverges. Equation (3.80) presents the same complication in $F_\gamma(E_\gamma/E_p, E_p)$ if $E_\gamma \sim E_p$ (see Eq. (B.2)). In these situations it is always recommended to impose that $|E - E_\gamma| > \epsilon$, where ϵ is set to prevent numerical conflicts.

Codes should also control the restrictions and check the conservation of certain physical quantities, such as the energy. For example, if the power injected in particles is $L_{\rm inj}$, the total luminosity radiated by the same particles must be equal or less than that value. In this sense, it is also important to test our simulations using simple problems with known solutions, as well as to evaluate the coherence of the outputs in the astrophysical context.

A.3 Numerical solutions for the transport equation

As mentioned in Section 3.2, the Fokker-Planck equation can be easily solved with numerical methods under many circumstances. Park & Petrosian (1996) analyze six finite difference methods to solve an equation of the form

$$\frac{\partial u(x,t)}{\partial t} = \frac{1}{A(x)}\frac{\partial}{\partial x}\left[C(x)\frac{\partial u(x,t)}{\partial x} + B(x)\,u(x,t)\right] - \frac{u(x,t)}{T(x)} + Q(x). \tag{A.7}$$

The discretization employed in their analysis bases on the one proposed by Chang & Cooper (1970)

$$\frac{u_m^{n+1} - u_m^n}{\Delta t} = \frac{1}{A_m}\frac{F_{m+1/2}^{n+1} - F_{m-1/2}^{n+1}}{\Delta x_m} - \frac{u_m^{n+1}}{T_m} + Q_m, \tag{A.8}$$

where $F(x,t) = C(x)\,\frac{\partial u(x,t)}{\partial x} + B(x)\,u(x,t)$, the time has been discretized in t_n values, with $n = 0, \ldots, N$, and x in x_m, with $m = 0, \ldots, M$. Additionally, $u_m^n = u(x_m, t_n)$, $\Delta x_m = (x_{m+1} - x_{m-1})/2$, and $\Delta t = t_{n+1} - t_n = \tau/N$, with τ the timescale of interest. In particular, the mesh of values for x_m is defined using a logarithmic increment $r = (x_M/x_0)^{(1/M)}$, which corresponds to $\Delta x_m = x_m\,(r-1)$ (see discussion in Appendix A.1). For minimizing errors, $\Delta x_m/x_m = r - 1 \lesssim 1$ is required.

Once that an expression for F_m^{n+1} is chosen, substituting it into Eq. (A.8) reduces the problem to a tridiagonal system of linear equations

$$\begin{cases} -a_m\,u_{m-1}^{n+1} + b_m\,u_m^{n+1} - c_m\,u_{m+1}^{n+1} = r_m, \\ a_0 = c_M = 0, \end{cases} \tag{A.9}$$

where the last condition is the result of imposing the conservation of the number of particles in absence of sinks and sources ($F_{M+1}^{n+1} = F_{-1/2}^{n+1} = 0$). These tridiagonal systems can be solved using a Gaussian elimination with back substitution routine, such as (adapted from Press et al. 1996)

```
!A*u(*)=r(*), where A is a matrix
!b vector with the diagonal coefficients: b_m
!a vector with the inferior diagonal coefficients: -a_m
!c vector with the superior diagonal coefficients: -c_m

SUBROUTINE tridag(a,b,c,r,u,n)
IMPLICT NONE
REAL(8), DIMENSION(:), INTENT(IN) :: a,b,c,r
REAL(8), DIMENSION(:), INTENT(OUT) :: u
REAL(8), DIMENSION(size(b)) :: gam
REAL(8) :: bet

bet = b(1)

u(1) = r(1)/bet
DO j = 2,n !Decomposition and forward substitution
```

```
        gam(j) = c(j-1)/bet
        bet = b(j) - a(j)*gam(j)
        u(j) = (r(j) - a(j)*u(j-1))/bet
END DO

!Back substitution
DO j = n-1,1,-1
    u(j) = u(j)-gam(j+1)*u(j+1)
END DO

END SUBROUTINE tridag
```

Comparing Eq. (A.7) with the equation that describes the particle distribution of a system with an energy diffusion coefficient $K(E)$, energy losses $b_{e,p}(E)$, characteristic escape timescale of the particles $\tau_{\rm esc}(E)$, and a particle injection $Q_{e,p}(E)$

$$\frac{\partial N_{e,p}(E,t)}{\partial t} = \frac{\partial}{\partial E}\left[K(E)\,\frac{\partial N_{e,p}(E,t)}{\partial E}\right] + \frac{\partial}{\partial E}\left[\left(b_{e,p}(E) - \frac{2\,K(E)}{E}\right) N_{e,p}(E,t)\right] + - \frac{N_{e,p}(E,t)}{\tau_{\rm esc}(E)} + Q_{e,p}(E), \tag{A.10}$$

it is possible to assign $x = E$, $u(E,t) = N_{e,p}(E,t)$, $A(E) = 1$[3], $C(E) = K(E)$, $B(E) = b_{e,p}(E) - 2\,K(E)/E$, $T(E) = \tau_{\rm esc}(E)$, and $Q(E) = Q_{e,p}(E)$. According to Park & Petrosian (1996), the best performance is carried out with the F_m^{n+1} proposed by Chang & Cooper (1970), which sets the coefficients of Eq. (A.9) as

$$a_m = \frac{\Delta t}{A_m\,\Delta x_m}\,\frac{C_{m-1/2}}{\Delta x_{m-1/2}}\,W^-_{m-1/2}, \tag{A.11}$$

$$c_m = \frac{\Delta t}{A_m\,\Delta x_m}\,\frac{C_{m+1/2}}{\Delta x_{m+1/2}}\,W^+_{m+1/2}, \tag{A.12}$$

$$b_m = 1 + \frac{\Delta t}{A_m\,\Delta x_m}\left[\frac{C_{m-1/2}}{\Delta x_{m-1/2}}\,W^+_{m-1/2} + \frac{C_{m+1/2}}{\Delta x_{m+1/2}}\,W^-_{m+1/2}\right] + \frac{\Delta t}{T_m}, \tag{A.13}$$

$$r_m = \Delta t\,Q_m + u^n_m, \tag{A.14}$$

$$a_0 = c_M = 0, \tag{A.15}$$

where

$$W^\pm_m = \frac{w_m}{2}\,\frac{\exp(\pm\, w_m/2)}{\sinh(w_m/2)}, \tag{A.16}$$

$$w_m = \frac{B_m}{C_m}\,\Delta x_m. \tag{A.17}$$

This solution develops some numerical instabilities in the end-point values of x. Therefore, it is recommended to obtain the outcome in a range slightly larger than the one needed and then to apply a cut to the values.

[3] If we prefer to use the momentum p of the particles instead of the energy, note that $A(p) = 4\,\pi\,p^2$.

Analogously, it is possible to find the solution of the time independent equation of a particle distribution of form

$$Q_{e,p}(E) = \frac{N_{e,p}(E)}{\tau_{\rm esc}(E)} - \frac{\partial[b_{e,p}(E)\, N_{e,p}(E)]}{\partial E}. \tag{A.18}$$

In this case, $x = E$, $A(E) = 1$, $B(E) = b_{e,p}(E)$, $C(E) = 0$, $T(E) = \tau_{esc}(E)$, and $Q(E) = Q_{e,p}(E)$. The coefficients of Eq. (A.9) are

$$a_m = \frac{B_{m-1/2}}{\Delta x_m}, \tag{A.19}$$

$$c_m = \frac{2\, B_{m+1/2}}{\Delta x_m}, \tag{A.20}$$

$$b_m = \frac{B_{m+1/2} + 2\, B_{m-1/2}}{\Delta x_m} + \frac{1}{T_m}, \tag{A.21}$$

$$r_m = Q_m, \tag{A.22}$$

$$a_0 = c_M = 0. \tag{A.23}$$

This numerical solution achieves the same precision as the semi-analytical solution given by Eq. (3.28), but the computing time is rather shorter, as well as time-dependent escape timescales are enabled.

Commonly, the particle distributions are not explicitly shown in academic publications. Nevertheless, to check the coherence of these outcomes is important. One way to do this is looking at the slopes of the particle distribution in a logarithmic scale plot. From Eq. (A.18), it can be easily seen that

$$\begin{aligned} N_{e,p}(E) &\sim \tau_{\rm esc}(E)\, Q_{e,p}(E) && \text{if } \tau_{\rm esc}(E) \ll E/b_{e,p}(E), \\ N_{e,p}(E) &\sim [b_{e,p}(E)]^{-1} \int_E^{E^{e,p}_{\rm max}} Q_{e,p}(E)\, dE && \text{if } \tau_{\rm esc}(E) \gg E/b_{e,p}(E). \end{aligned} \tag{A.24}$$

Consequently, if $Q_{e,p}(E) \propto E^{-p}$, $\tau_{\rm esc}(E) \propto E^{-\alpha}$, and $b_{e,p}(E) \propto E^{\beta}$, these asymptotic solutions are

$$\begin{aligned} N_{e,p}(E) &\propto E^{-(p+\alpha)} && \text{if } \tau_{\rm esc}(E) \ll E/b_{e,p}(E), \\ N_{e,p}(E) &\propto E^{-(p+\beta)+1} && \text{if } \tau_{\rm esc}(E) \gg E/b_{e,p}(E), \end{aligned} \tag{A.25}$$

respectively.

A.4 Fermi-LAT Catalog

This section provides a little help for readers trying to handle the Fermi-LAT Source Catalog for the first time[4]. The Fermi Collaboration offers for their Source Catalogs a very simple and intuitive browser version. Nevertheless, this browser version is not immediately completed after the release of a new catalog and it is very inconvenient if the user requires to extract several information. Consequently, downloading and extracting the data from the FITS file is a better option. The Flexible Image Transport

[4]The author of this thesis is not an expert in the topic, so please take this information just as assistance from a non-expert to another.

System (FITS) is the most used digital format in astronomy. In the LAT Source Catalog, the Fermi Collaboration provides an script to convert files from FITS to XML. However, working directly with the FITS file is possible using, for example, the package *astropy* of Python. For instance, the following lines of code assign the data of the FITS file to the variable `catalog`.

```
from astropy.io import fits

hdu_list = fits.open("file.fit")

catalog = hdu_list[1].data
```

Let us now assume that we want to extract only the data of NGC 253. The corresponding information contained in the FITS file is clarified in the catalog papers (see e.g., Table 12 in Abdollahi et al. 2020). Since the standard name of the source is written in the column named "ASSOC1", the data of an specific source can be collected with

```
source_data = catalog[catalog["ASSOC1"] == "NGC 253"]
```

The spectral information of a power-law fitted source is contained in the columns

```
s_index=source_data["PL_Index"] #spectral index
E0=source_data["Pivot_Energy"] #MeV
K=source_data["PL_Flux_Density"] #ph cm^-2 s^-1 MeV^-1

ph_band=source_data["Flux_Band"]
err_ph_band=source_data["Unc_Flux_Band"]

ener_fluxes=source_data["nuFnu_Band"]
```

The differential flux of the source is given by

$$\frac{dN}{dE} = K \left(\frac{E}{E_0}\right)^{-\Gamma}, \tag{A.26}$$

where Γ is the spectral index (`s_index`). The photon flux in each energy band of the catalog is contained in the column "Flux_Band" (`ph_band`). The energy flux in each energy band is given in "nuFnu_Band", which are obtained in each energy bin i as

$$\texttt{energy\_flux[i]} = \left(\int_A^B \frac{dN}{dE}\, dE\right)^{-1} \frac{\texttt{ph\_band[0][i]}}{\ln(B/A)} \int_A^B \frac{dN}{dE}\, E\, dE \tag{A.27}$$

where A and B are the end-points of the energy interval. The relative errors of these values are the same as that on the corresponding fluxes ("Unc_Flux_Band") (Acero et al. 2015). The energy bands, the name of the columns, as well as the format of data can differ for different catalogs. Therefore, it is essential to check the description of the data in the corresponding catalog papers.

B

Miscellany

This appendix contains extra formulas used to estimate certain radiative processes or model parameters.

B.1 Thermal Bremsstrahlung

The luminosity produced by thermal bremsstrahlung[1] from a plasma composed by nuclei of charge $Z\,e$ can be computed as (Rybicki & Lightman 1979)

$$L_{\rm ff}(\epsilon) = \frac{2^5\,\pi\,e^6}{3\,m_e\,c^3\,h}\left(\frac{2\,\pi}{3\,k_{\rm B}\,m_e}\right)^{1/2} Z^2\,\epsilon\int_V T^{-1/2}\,n_e\,n_i\,e^{-\epsilon/k_{\rm B}T}\,\bar{g_{\rm ff}}\,dV \tag{B.1}$$

where dV is the differential of volume, T the temperature, $\bar{g_{\rm ff}}$ is a velocity averaged Gaunt factor, and n_e, n_i are the electron and ion number densities, respectively. The value of $\bar{g_{\rm ff}}(T)$ is close to the unity for $\epsilon \sim k_{\rm B}T$, and it is not relevant for $\epsilon \gg k_{\rm B}T$, because the spectrum drops at such energies. Therefore, it is usually assumed to be 1.2, providing an accuracy of about 20% (see e.g., Rybicki & Lightman 1979, and references therein).

The physical process is the same described for relativistic electrons, but in this case, the particles are non-relativistic and follow a Maxwellian velocity distribution. The X-ray emission observed in galaxy clusters is produced by this mechanism. In the shock scenarios, this radiative process can be relevant in the shocked matter if the thermal equilibrium is reached (see e.g., Draine & McKee 1993; Somov 2012, for more detailed discussions).

B.2 Proton-proton inelastic collisions: $E_p > 100\,\mathrm{GeV}$

As mentioned in Section 3.4.2.6, the gamma emissivity produced by protons with energies above 100 GeV in inelastic collisions can be computed employing the analytical expression Eq. (3.80) provided by Kelner et al. (2006). Defining $x = E_\gamma/E_p$, the $F_\gamma(E_\gamma/E_p, E_p)$ can be written as

$$F_\gamma(x, E_p) = B_\gamma\frac{\ln(x)}{x}\left(\frac{1-x^{\beta_\gamma}}{1+k_\gamma x^{\beta_\gamma}(1-x^{\beta_\gamma})}\right)^4\left[\frac{1}{\ln(x)} - \frac{4\beta_\gamma x^{\beta_\gamma}}{1-x^{\beta_\gamma}} - \frac{4k_\gamma\beta_\gamma x^{\beta_\gamma}(1-2x^{\beta_\gamma})}{1+k_\gamma x^{\beta_\gamma}(1-x^{\beta_\gamma})}\right]. \tag{B.2}$$

[1] Also known as free-free emission.

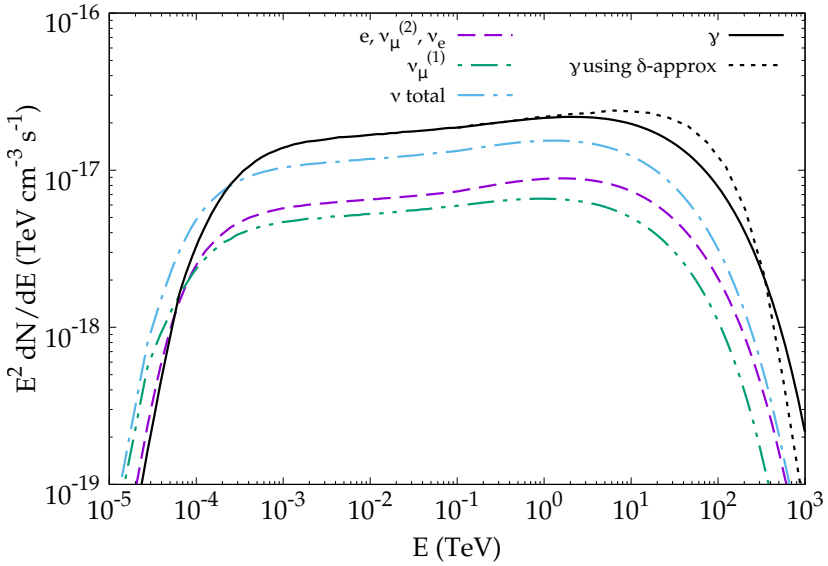

Figure B.1: Spectral energy distribution of all the particles created in pp interactions calculated with the expressions provided by Kelner et al. (2006). The interactions of the secondary particles with the medium are assumed to be negligible, i.e., the particles decay before they interact.

This function is set to match the numerical results of the SYBILL code[2] taking into account not only the contribution from the decay of π^0, but also from the decay of η-mesons, which becomes about of 25 % for $x \sim 0.1$. The best fit parameters B_γ, β_γ, and k_γ in the range $0.1\,\mathrm{TeV} \leq E_p \leq 10^5\,\mathrm{TeV}$ are found to be

$$B_\gamma = 1.30 + 0.14\,L + 0.011\,L^2, \tag{B.3}$$

$$\beta_\gamma = \frac{1}{1.79 + 0.11\,L + 0.008\,L^2}, \tag{B.4}$$

$$k_\gamma = \frac{1}{0.801 + 0.049\,L + 0.014\,L^2}, \tag{B.5}$$

where $L = \ln(E_p/\mathrm{TeV})$.

This analytical estimation agrees with the simulations within a few percent for $x \gtrsim 10^{-3}$ and $E_\gamma \gtrsim 1\,\mathrm{GeV}$, but it does not have a good performance at lower energies. Therefore, it should be combined with another solution such as the δ-functional approximation (Aharonian & Atoyan 2000). In the same way, the latter analytical form produces an overestimation at high energies (see Fig. B.1). Additionally, Kelner et al. (2006) provide analytical expressions for the calculation of neutrinos and electrons. Figure B.1 is a reproduction of figure 12 from Kelner et al. (2006), which displays the spectral energy distribution of all the particles created in pp interactions of protons following a distribution $N_p(E_p) = Q_0 E_p^{-2} e^{-E_p/\mathrm{PeV}}$, with Q_0 obtained from $\int_{\mathrm{TeV}}^{\infty} E_p\, N_p(E_p)\, dE_p = 1\,\mathrm{erg\,cm^{-3}}$. In all the cases, building the complete spectrum requires to demand the continuity between the low-energy and high-energy approximations, i.e., setting the value of $\tilde{n}$ in Eq. (3.83). Some $\tilde{n}$ values are given by Kelner et al. (2006) for different spectral indices of the proton distribution. Nevertheless, if

[2] Fletcher et al. 1994

we are working with evolved particle distributions or we want to run our simulations changing the spectral index, it is convenient to set $\tilde{n}$ directly in our code. One way to do this is calculating the spectral energy distributions for $E_p < 100\,\mathrm{GeV}$ and $E_p \geq 100\,\mathrm{GeV}$, and then multiplying the results for proton energies below 100 GeV by

$$\tilde{n} = \frac{q_{\geq 100\,\mathrm{GeV}}(100\,\mathrm{GeV})}{q_{<100\,\mathrm{GeV}}(100\,\mathrm{GeV})}. \tag{B.6}$$

If we want to avoid to run twice over a data set, a better option is to compute the distribution from the higher to the lower energies. In this way, $\tilde{n}$ can be found after the calculation of just one value in the $E_p < 100\,\mathrm{GeV}$ part of the solution. Regardless of the $\tilde{n}$ estimation, the reader should not forget to check the ranges in which each of the expressions is valid and include them into the code (see Appendix A for a few general coding recommendations).

B.3 Accretion disks

The accretion of matter allows to explain phenomena observed in many astrophysical sources, from young stellar objects and planetary systems to active galactic nuclei (AGNs). The angular momentum of the accreting matter is typically non-zero, and consequently, the matter forms a disk. The bases of standard disk accretion were first established by Shakura & Sunyaev (1973). In their work, they propose that the accretion process is lead by turbulent viscosity, which produces the loss of angular momentum and the dissipation of energy. The disk model of Shakura & Sunyaev (1973) is also known as thin or steady α-disk model, as a consequence of the properties they assumed. First, the disk is axisymmetric. The vertical half-thickness H at a given point is much smaller than the radial distance of the point R, which is measured from the center. Second, the azimuthal rotation corresponds to the circular Keplerian motion and the disk is in hydrostatic equilibrium in the vertical direction. Third, the horizontal pressure gradient and heat flux are also negligible, as well as its self-gravitation. The averaged kinematic viscosity is defined as $\nu = \alpha\, c_\mathrm{s}\, H$, where c_s is the speed of the sound and α is the viscosity coefficient.

From the hydrodynamic equations for mass, energy, and momentum conservation, the disk parameters can be found in terms of the mass of the central object M, the accretion rate $\dot{M}$, the radial distance R, and the viscosity coefficient α. Using the

previous assumptions and scaling the equations to typical AGN parameters gives (Shakura & Sunyaev 1973; Treves et al. 1988; Frank et al. 2002)

$$\Sigma = 5.2\times10^{6}\alpha^{-4/5}\dot{M}_{26}^{7/10}M_{8}^{1/4}R_{14}^{-3/4}f^{14/5}\ \ \mathrm{g\,cm^{-2}} \tag{B.7}$$

$$H = 1.7\times10^{11}\alpha^{-1/10}\dot{M}_{26}^{3/10}M_{8}^{-3/8}R_{14}^{9/8}f^{3/5}\ \ \mathrm{cm} \tag{B.8}$$

$$\rho = 3.1\times10^{-5}\alpha^{-7/10}\dot{M}_{26}^{11/20}M_{8}^{5/8}R_{14}^{-15/8}f^{11/5}\ \ \mathrm{g\,cm^{-3}} \tag{B.9}$$

$$T_{\mathrm{c}} = 1.4\times10^{6}\alpha^{-1/5}\dot{M}_{26}^{3/10}M_{8}^{1/4}R_{14}^{-3/4}f^{6/5}\ \ \mathrm{K} \tag{B.10}$$

$$T_{\mathrm{eff}} = 2.2\times10^{5}\dot{M}_{26}^{1/4}M_{8}^{1/4}R_{14}^{-3/4}\ \ \mathrm{K} \tag{B.11}$$

$$\tau = 1.9\times10^{4}\alpha^{-4/5}\dot{M}_{26}^{1/5}f^{4/5} \tag{B.12}$$

$$\nu = 1.8\times10^{18}\alpha^{4/5}\dot{M}_{26}^{3/10}M_{8}^{-1/4}R_{14}^{3/4}f^{6/5}\ \ \mathrm{cm^{2}\,s^{-1}} \tag{B.13}$$

$$v_{\mathrm{R}} = 2.7\times10^{4}\alpha^{4/5}\dot{M}_{26}^{3/10}M_{8}^{-1/4}R_{14}^{-1/4}f^{-14/5}\ \ \mathrm{cm\,s^{-1}}, \tag{B.14}$$

where $M_8 = M/(10^8\,\mathrm{M_\odot})$, $\dot{M}_{26} = \dot{M}/(10^{26}\,\mathrm{g\,s^{-1}})$, $R_{14} = R/(10^{14}\,\mathrm{cm})$, and $f = 1 - \sqrt{R_{\mathrm{in}}/R}$, with R_{in} the inner radius of the disc. In the particular case in which the inner radius is the last stable orbit for a Schwarzschild black hole, $R_{\mathrm{in}} = 6GM/c^2$. Here Σ is the surface density, ρ is the volumetric density, T_{c} is the central temperature, T_{eff} is the effective temperature of the disk at the surface, τ is the optical depth, ν the kinematic viscosity, and v_{R} the radial velocity.

Accretion disks can be typically divided in three regions: i) an outer region where the gas pressure dominates over the radiation pressure and the opacity is due to free-free absorption, ii) a middle region in which the gas pressure is still dominating, but the opacity is due to Thomson scattering of electrons, and iii) an inner region in which radiation pressure dominates and the opacity is also due to scattering. The existence of region ii) and iii) depends on the accretion rate. The solution previously presented is valid only if the gas pressure is larger than the radiative pressure. This condition is satisfied if

$$R \gtrsim 5.2\times10^{14}\alpha^{8/30}\dot{M}_{26}^{14/15}M_{8}^{1/3}f^{56/15}\ \ \mathrm{cm}, \tag{B.15}$$

otherwise other accretion disk models should be considered (see e.g., Frank et al. 2002, for more details). Particularly, along the region of the disk in which the absorption dominates the opacity, the spectrum of the accretion disk can be approximated as the superposition of rings emitting as blackbodies of temperature T_{eff} each (Romero & Vila 2014a)

$$L_{\mathrm{disk}}(\epsilon) = \frac{4\pi^2}{h^3\,c^2}\,\epsilon^4\int_{R_{\mathrm{in}}}^{R_{\mathrm{out}}}\frac{r}{\left[e^{\epsilon/[k_{\mathrm{B}}T_{\mathrm{eff}}(r)]}-1\right]}dr. \tag{B.16}$$

Bibliography

Aab, A., Abreu, P., Aglietta, M., et al. 2014, Phys. Rev. D, 90, 122006

Aab, A., Abreu, P., Aglietta, M., et al. 2018, ApJ, 853, L29

Aab, A., Abreu, P., Aglietta, M., et al. 2017, ArXiv 1708.06592 [arXiv:1708.06592]

Aab, A., Abreu, P., Aglietta, M., et al. 2020a, Phys. Rev. D, 102, 062005

Aab, A., Abreu, P., Aglietta, M., et al. 2020b, Phys. Rev. Lett., 125, 121106

Aartsen, M. G., Ackermann, M., Adams, J., et al. 2018, Phys. Rev. D, 98, 062003

Aartsen, M. G., Ackermann, M., Adams, J., et al. 2020, Phys. Rev. Lett., 124, 051103

Aartsen, M. G., Ackermann, M., Adams, J., et al. 2014, Physical Review Letters, 113, 101101

Abbasi, R., Bellido, J., Belz, J., et al. 2016, in Proceedings of International Symposium for Ultra-High Energy Cosmic Rays (UHECR2014, 010016

Abbott, B. P., Abbott, R., Abbott, T. D., et al. 2019, Physical Review X, 9, 031040

Abbott, B. P., Abbott, R., Abbott, T. D., et al. 2017, ApJ, 848, L12

Abdo, A. A., Ackermann, M., Ajello, M., et al. 2010, ApJ, 709, L152

Abdollahi, S., Acero, F., Ackermann, M., et al. 2020, ApJS, 247, 33

Abolmasov, P. & Poutanen, J. 2017, MNRAS, 464, 152

Abramowski, A., Acero, F., Aharonian, F., et al. 2012, ApJ, 757, 158

Abu-Zayyad, T., Aida, R., Allen, M., et al. 2012, Astroparticle Physics, 39, 109

Acciari, V. A., Aliu, E., Arlen, T., et al. 2009, Nature, 462, 770

Acero, F., Ackermann, M., Ajello, M., et al. 2015, ApJS, 218, 23

Acero, F., Aharonian, F., Akhperjanian, A. G., et al. 2009, Science, 326, 1080

Ackermann, M., Ajello, M., Albert, A., et al. 2015, ApJ, 799, 86

Ackermann, M., Ajello, M., Allafort, A., et al. 2012a, ApJ, 747, 104

Ackermann, M., Ajello, M., Allafort, A., et al. 2012b, ApJ, 755, 164

Adamo, A., Smith, L. J., Gallagher, J. S., et al. 2012, MNRAS, 426, 1185

Agaronyan, F. A., Atoyan, A. M., & Nagapetyan, A. M. 1983, Astrophysics, 19, 187

Aharonian, F. A. & Atoyan, A. M. 1981, Ap&SS, 79, 321

Aharonian, F. A. & Atoyan, A. M. 1996, A&A, 309, 917

Aharonian, F. A. & Atoyan, A. M. 2000, A&A, 362, 937

Ahlers, M. & Halzen, F. 2018, Progress in Particle and Nuclear Physics, 102, 73

Ajello, M., Di Mauro, M., Paliya, V. S., & Garrappa, S. 2020, arXiv e-prints, arXiv:2003.05493

Aleksić, J., Ansoldi, S., Antonelli, L. A., et al. 2016, Astroparticle Physics, 72, 61

Alexander, D. M. & Hickox, R. C. 2012, New A Rev., 56, 93

Allard, D. 2012, Astroparticle Physics, 39, 33

Alonso-Herrero, A., Roche, P. F., Esquej, P., et al. 2013, ApJ, 779, L14

Alves Batista, R., Biteau, J., Bustamante, M., et al. 2019, Frontiers in Astronomy and Space Sciences, 6, 23

Anchordoqui, L. A. 2018, Phys. Rev. D, 97, 063010

Anchordoqui, L. A., Paul, T. C., da Silva, L. H. M., Torres, D. F., & Vlcek, B. J. 2014, Phys. Rev. D, 89, 127304

Anchordoqui, L. A., Romero, G. E., & Combi, J. A. 1999, Phys. Rev. D, 60, 103001

Anchordoqui, L. A. & Torres, D. F. 2020, Phys. Rev. D, 102, 023034

Antoni, T., Apel, W. D., Badea, A. F., et al. 2005, Astroparticle Physics, 24, 1

Antonucci, R. 1993, ARA&A, 31, 473

Antonucci, R. R. J. 1984, ApJ, 278, 499

Antonucci, R. R. J. & Miller, J. S. 1985, ApJ, 297, 621

Apel, W. D., Arteaga-Velázquez, J. C., Bekk, K., et al. 2011, Phys. Rev. Lett., 107, 171104

Araudo, A. T., Bosch-Ramon, V., & Romero, G. E. 2009, A&A, 503, 673

Araudo, A. T., Bosch-Ramon, V., & Romero, G. E. 2010, A&A, 522, A97

Arav, N., Barlow, T. A., Laor, A., & Bland ford, R. D. 1997, MNRAS, 288, 1015

Armitage, P. J., Zurek, W. H., & Davies, M. B. 1996, ApJ, 470, 237

Asano, K. & Mészáros, P. 2016, Phys. Rev. D, 94, 023005

Atwood, W. B., Abdo, A. A., Ackermann, M., et al. 2009, ApJ, 697, 1071

Axford, W. I., Leer, E., & Skadron, G. 1977, in International Cosmic Ray Conference, Vol. 11, International Cosmic Ray Conference, 132

Baade, W. & Minkowski, R. 1954, ApJ, 119, 206

Ballet, J., Burnett, T. H., Digel, S. W., & Lott, B. 2020, arXiv e-prints, arXiv:2005.11208

Bamba, A., Yamazaki, R., Ueno, M., & Koyama, K. 2003, ApJ, 589, 827

Barcons, X., Barret, D., Decourchelle, A., et al. 2017, Astronomische Nachrichten, 338, 153

Batista, R. A., Dundovic, A., Erdmann, M., et al. 2016, Journal of Cosmology and Astroparticle Physics, 2016, 038

Bauer, F. E., Arévalo, P., Walton, D. J., et al. 2015, ApJ, 812, 116

Bauer, M., Pietsch, W., Trinchieri, G., et al. 2008, A&A, 489, 1029

Bechtol, K., Ahlers, M., Di Mauro, M., Ajello, M., & Vandenbroucke, J. 2017, ApJ, 836, 47

Becker, W. 2009, Neutron Stars and Pulsars, Vol. 357

Beckmann, V. & Shrader, C. R. 2012, Active Galactic Nuclei

Bell, A. R. 1978, MNRAS, 182, 147

Bell, A. R. 2004, MNRAS, 353, 550

Beresnyak, A., Jones, T. W., & Lazarian, A. 2009, ApJ, 707, 1541

Beresnyak, A. & Lazarian, A. 2019, Turbulence in Magnetohydrodynamics

Berezhko, E. G., Ksenofontov, L. T., & Völk, H. J. 2003, A&A, 412, L11

Berezinskii, V. S., Bulanov, S. V., Dogiel, V. A., & Ptuskin, V. S. 1990, Astrophysics of cosmic rays

Berezinsky, V. 2007, arXiv e-prints, arXiv:0710.2750

Bernard-Salas, J., Spoon, H. W. W., Charmandaris, V., et al. 2009, ApJS, 184, 230

Bionta, R. M., Blewitt, G., Bratton, C. B., et al. 1987, Phys. Rev. Lett., 58, 1494

Blandford, R. D., Netzer, H., Woltjer, L., Courvoisier, T. J.-L., & Mayor, M., eds. 1990, Active Galactic Nuclei, 97

Blandford, R. D. & Ostriker, J. P. 1978, ApJ, 221, L29

Blumenthal, G. R. & Gould, R. J. 1970, Rev. Mod. Phys., 42, 237

Boettcher, M. & Schlickeiser, R. 1997, A&A, 325, 866

Bolatto, A. D., Warren, S. R., Leroy, A. K., et al. 2013, Nature, 499, 450

Boldt, E. & Ghosh, P. 1999, MNRAS, 307, 491

Böttcher, M. & Els, P. 2016, ApJ, 821, 102

Burbidge, G. R. 1956, ApJ, 124, 416

Bustard, C., Zweibel, E. G., & Cotter, C. 2017, ApJ, 835, 72

Bykov, A. M. 2001, Space Sci. Rev., 99, 317

Bykov, A. M. 2014, A&A Rev., 22, 77

Bykov, A. M., Brandenburg, A., Malkov, M. A., & Osipov, S. M. 2013, Space Sci. Rev., 178, 201

Bykov, A. M., Ellison, D. C., Marcowith, A., & Osipov, S. M. 2018, Space Sci. Rev., 214, 41

Bykov, A. M., Marcowith, A., Amato, E., et al. 2020, Space Sci. Rev., 216, 42

Caballero-Garcia, M. D., Papadakis, I. E., Nicastro, F., & Ajello, M. 2012, A&A, 537, A87

Caprioli, D. 2015, ApJ, 811, L38

Chakraborti, S., Ray, A., Soderberg, A. M., Loeb, A., & Chandra, P. 2011, Nature Communications, 2, 175

Chang, J. S. & Cooper, G. 1970, Journal of Computational Physics, 6, 1

Chang, X.-C., Liu, R.-Y., & Wang, X.-Y. 2015, ApJ, 805, 95

Chang, X.-C. & Wang, X.-Y. 2014, ApJ, 793, 131

Chevalier, R. A. & Clegg, A. W. 1985, Nature, 317, 44

Clarke, C. & Carswell, B. 2007, Principles of Astrophysical Fluid Dynamics

Conti, P. S., Crowther, P. A., & Leitherer, C. 2008, From Luminous Hot Stars to Starburst Galaxies

Cooper, J. L., Bicknell, G. V., Sutherland, R. S., & Bland-Hawthorn, J. 2008, ApJ, 674, 157

Cooper, J. L., Bicknell, G. V., Sutherland, R. S., & Bland-Hawthorn, J. 2009, ApJ, 703, 330

Cox, A. N. 2000, Allen's astrophysical quantities

CTA Consortium & Ong, R. A. 2019, in European Physical Journal Web of Conferences, Vol. 209, European Physical Journal Web of Conferences, 01038

Dalcanton, J. J., Williams, B. F., Seth, A. C., et al. 2009, ApJS, 183, 67

Davidge, T. J. 2010, ApJ, 725, 1342

Davidge, T. J. & Pritchet, C. J. 1990, AJ, 100, 102

de Angelis, A., Tatischeff, V., Grenier, I. A., et al. 2018, Journal of High Energy Astrophysics, 19, 1

De Naurois, M. 2019, in International Cosmic Ray Conference, Vol. 36, 36th International Cosmic Ray Conference (ICRC2019), 656

De Souza, V., Pierre Auger Collaboration, & Telescope Array Collaboration. 2017, in International Cosmic Ray Conference, Vol. 301, 35th International Cosmic Ray Conference (ICRC2017), 522

del Palacio, S., Bosch-Ramon, V., Müller, A. L., & Romero, G. E. 2018, A&A, 617, A13

del Palacio, S., Bosch-Ramon, V., & Romero, G. E. 2019, A&A, 623, A101

del Valle, M. V., Lazarian, A., & Santos-Lima, R. 2016, MNRAS, 458, 1645

del Valle, M. V., Müller, A. L., & Romero, G. E. 2018, MNRAS, 475, 4298

del Valle, M. V. & Pohl, M. 2018, ApJ, 864, 19

del Valle, M. V. & Romero, G. E. 2012, A&A, 543, A56

Dermer, C. D. & Giebels, B. 2016, Comptes Rendus Physique, 17, 594

Dietrich, M., Wagner, S. J., Courvoisier, T. J. L., Bock, H., & North, P. 1999, A&A, 351, 31

Domingo-Santamaría, E. & Torres, D. F. 2005, A&A, 444, 403

Dönmez, O. 2006, Ap&SS, 305, 187

Doroshenko, V. T., Sergeev, S. G., Klimanov, S. A., Pronik, V. I., & Efimov, Y. S. 2012, MNRAS, 426, 416

Draine, B. T. & McKee, C. F. 1993, ARA&A, 31, 373

Drury, L. O. 1983, Reports on Progress in Physics, 46, 973

Eichler, D., Livio, M., Piran, T., & Schramm, D. N. 1989, Nature, 340, 126

Eichmann, B. & Becker Tjus, J. 2016, ApJ, 821, 87

Erdmann, M., Müller, G., Urban, M., & Wirtz, M. 2016, Astropart. Phys., 85, 54

Fabian, A. C. 1999, Proceedings of the National Academy of Science, 96, 4749

Fang, K., Kotera, K., & Olinto, A. V. 2012a, ApJ, 750, 118

Fang, K., Kotera, K., & Olinto, A. V. 2012b, ApJ, 750, 118

Farrar, G. R. & Piran, T. 2014, arXiv e-prints, arXiv:1411.0704

Farrar, G. R., Unger, M., & Anchordoqui, L. A. 2015, arXiv e-prints, arXiv:1512.00484

Fermi, E. 1949, Physical Review, 75, 1169

Fernández-Ontiveros, J. A., Prieto, M. A., & Acosta-Pulido, J. A. 2009, MNRAS, 392, L16

Fletcher, R. S., Gaisser, T. K., Lipari, P., & Stanev, T. 1994, Phys. Rev. D, 50, 5710

Fouque, P., Gourgoulhon, E., Chamaraux, P., & Paturel, G. 1992, A&AS, 93, 211

Frank, J., King, A., & Raine, D. J. 2002, Accretion Power in Astrophysics: Third Edition

Gabici, S., Evoli, C., Gaggero, D., et al. 2019, International Journal of Modern Physics D, 28, 1930022

Gaisser, T. 2017, in European Physical Journal Web of Conferences, Vol. 145, European Physical Journal Web of Conferences, 18003

Gaisser, T. K. 1990, Cosmic rays and particle physics

Gaisser, T. K., Engel, R., & Resconi, E. 2016, Cosmic Rays and Particle Physics

Gallimore, J. F., Baum, S. A., & O'Dea, C. P. 2004, ApJ, 613, 794

García-Burillo, S., Combes, F., Ramos Almeida, C., et al. 2016, ApJ, 823, L12

Gavazzi, G., Savorgnan, G., & Fumagalli, M. 2011, A&A, 534, A31

Ghisellini, G. 2013, Radiative Processes in High Energy Astrophysics, Vol. 873

Ginzburg, V. L. & Syrovatskii, S. I. 1964, The Origin of Cosmic Rays (Macmillan)

Gould, R. J. & Schréder, G. P. 1967, Physical Review, 155, 1404

Gregori, G., Miniati, F., Ryu, D., & Jones, T. W. 2000, ApJ, 543, 775

Greisen, K. 1966, Phys. Rev. Lett., 16, 748

Grier, C. J., Peterson, B. M., Horne, K., et al. 2013, ApJ, 764, 47

Günthardt, G. I., Agüero, M. P., Camperi, J. A., et al. 2015, AJ, 150, 139

Gutiérrez, E. M., Romero, G. E., & Vieyro, F. L. 2020, MNRAS, 494, 2109

H. E. S. S. Collaboration, Abdalla, H., Aharonian, F., et al. 2018, A&A, 617, A73

Halzen, F. & Klein, S. R. 2010, Review of Scientific Instruments, 81, 081101

Hardcastle, M. J., Cheung, C. C., Feain, I. J., & Stawarz, Ł. 2009, MNRAS, 393, 1041

Haungs, A., Rebel, H., & Roth, M. 2003, Reports on Progress in Physics, 66, 1145

Heckman, T. M., Armus, L., & Miley, G. K. 1990, ApJS, 74, 833

Heesen, V., Beck, R., Krause, M., & Dettmar, R.-J. 2009a, A&A, 494, 563

Heesen, V., Krause, M., Beck, R., & Dettmar, R.-J. 2009b, A&A, 506, 1123

Hess, V. F. 1912, Phys. Z., 13, 1084

Hillas, A. M. 1984, ARA&A, 22, 425–444

Hirata, K., Kajita, T., Koshiba, M., et al. 1987, Phys. Rev. Lett., 58, 1490

IceCube Collaboration, Aartsen, M. G., Ackermann, M., et al. 2018a, Science, 361, eaat1378

IceCube Collaboration, Aartsen, M. G., Ackermann, M., et al. 2019, arXiv e-prints, arXiv:1910.08488

IceCube Collaboration, Aartsen, M. G., Ackermann, M., et al. 2018b, Science, 361, 147

Impellizzeri, C. M. V., Gallimore, J. F., Baum, S. A., et al. 2019, ApJ, 884, L28

Inoue, Y., Khangulyan, D., & Doi, A. 2020, ApJ, 891, L33

Jansson, R. & Farrar, G. R. 2012a, Astrophys. J., 757, 14

Jansson, R. & Farrar, G. R. 2012b, The Astrophysical Journal Letters, 761, L11

Jennison, R. C. & Das Gupta, M. K. 1953, Nature, 172, 996

Jokipii, J. R. & Morfill, G. E. 1985, ApJ, 290, L1

Kampert, K.-H., Kulbartz, J., Maccione, L., et al. 2013, Astroparticle Physics, 42, 41

Karachentsev, I. D., Grebel, E. K., Sharina, M. E., et al. 2003, A&A, 404, 93

Karle, A. 2013, in IAU Symposium, Vol. 288, Astrophysics from Antarctica, ed. M. G. Burton, X. Cui, & N. F. H. Tothill, 98–104

Karlsson, N. 2009, arXiv e-prints, arXiv:0912.3807

Kaspi, S., Brandt, W. N., Maoz, D., et al. 2007, ApJ, 659, 997

Kawata, K., di Matteo, A., Fujii, T., et al. 2019, in International Cosmic Ray Conference, Vol. 36, 36th International Cosmic Ray Conference (ICRC2019), 310

Kelner, S. R., Aharonian, F. A., & Bugayov, V. V. 2006, Phys. Rev. D, 74, 034018

Kennicutt, Robert C., J. 1998a, ARA&A, 36, 189

Kennicutt, Robert C., J. 1998b, ApJ, 498, 541

Kennicutt, R. C. & Evans, N. J. 2012, ARA&A, 50, 531

Klein, R. I., McKee, C. F., & Colella, P. 1994, ApJ, 420, 213

Komissarov, S. S. & Barkov, M. V. 2007, MNRAS, 382, 1029

Kornecki, P., Pellizza, L. J., del Palacio, S., et al. 2020, A&A, 641, A147

Kouchner, A. 2019, in European Physical Journal Web of Conferences, Vol. 207, European Physical Journal Web of Conferences, 01001

Kowal, G. & Lazarian, A. 2010, ApJ, 720, 742

Kreckel, K., Armus, L., Groves, B., et al. 2014, ApJ, 790, 26

Krymskii, G. F. 1977, Akademiia Nauk SSSR Doklady, 234, 1306

Lacki, B. C. 2014, MNRAS, 444, L39

Lacki, B. C. & Thompson, T. A. 2013, ApJ, 762, 29

Lamastra, A., Fiore, F., Guetta, D., et al. 2016, A&A, 596, A68

Lamastra, A., Tavecchio, F., Romano, P., Landoni, M., & Vercellone, S. 2019, Astroparticle Physics, 112, 16

Landau, L. D. & Lifshitz, E. M. 1987, Fluid Mechanics

Laor, A. 2003, ApJ, 590, 86

Larson, R. B. & Tinsley, B. M. 1978, ApJ, 219, 46

Lazarian, A. & Vishniac, E. T. 1999, ApJ, 517, 700

Lee, H. M., Kang, H., & Ryu, D. 1996, ApJ, 464, 131

Lehnert, M. D., Heckman, T. M., & Weaver, K. A. 1999, ApJ, 523, 575

Lenain, J. P., Ricci, C., Türler, M., Dorner, D., & Walter, R. 2010, A&A, 524, A72

Levinson, A. 2000, Physical Review Letters, 85, 912

Levinson, A. & Boldt, E. 2002, Astroparticle Physics, 16, 265

Liu, R.-Y. & Wang, X.-Y. 2012, ApJ, 746, 40

Lodato, G. & Bertin, G. 2003, A&A, 398, 517

Longair, M. S. 2011, High Energy Astrophysics

Marandon, V., Jardin-Blicq, A., & Schoorlemmer, H. 2019, in International Cosmic Ray Conference, Vol. 36, 36th International Cosmic Ray Conference (ICRC2019), 736

Marcolini, A., Strickland, D. K., D'Ercole, A., Heckman, T. M., & Hoopes, C. G. 2005, MNRAS, 362, 626

Marcowith, A., Ferrand, G., Grech, M., et al. 2020, Living Reviews in Computational Astrophysics, 6, 1

Marinucci, A., Bianchi, S., Matt, G., et al. 2016, MNRAS, 456, L94

Marinucci, A., Bianchi, S., Nicastro, F., Matt, G., & Goulding, A. D. 2012, ApJ, 748, 130

Matthews, T. A. & Sandage, A. R. 1963, ApJ, 138, 30

McCourt, M., O'Leary, R. M., Madigan, A.-M., & Quataert, E. 2015, MNRAS, 449, 2

McCray, R. & Snow, Jr., T. P. 1979, ARA&A, 17, 213

McEnery, J., van der Horst, A., Dominguez, A., et al. 2019, in BAAS, Vol. 51, 245

Miller, M. C. & Yunes, N. 2019, Nature, 568, 469

Mould, J. & Sakai, S. 2008, ApJ, 686, L75

Müller, A. L. & Romero, G. E. 2020, A&A, 636, A92

Müller, A. L., Romero, G. E., & Roth, M. 2020, MNRAS, 496, 2474

Müller-Sánchez, F., González-Martín, O., Fernández-Ontiveros, J. A., Acosta-Pulido, J. A., & Prieto, M. A. 2010, ApJ, 716, 1166

Murase, K., Ioka, K., Nagataki, S., & Nakamura, T. 2008, Phys. Rev. D, 78, 023005

Murase, K., Kimura, S. S., & Meszaros, P. 2019, arXiv e-prints, arXiv:1904.04226

Myasnikov, A. V., Zhekov, S. A., & Belov, N. A. 1998, MNRAS, 298, 1021

Nayakshin, S., Cuadra, J., & Sunyaev, R. 2004, A&A, 413, 173

O'C Drury, L., Duffy, P., & Kirk, J. G. 1996, A&A, 309, 1002

Ohm, S. 2016, Comptes Rendus Physique, 17, 585

O'Sullivan, S., Reville, B., & Taylor, A. M. 2009, MNRAS, 400, 248

P. Abreu *et al.* (Pierre Auger Collab.). 2012, Astropart. Phys., 35, 354

Padmanabhan, T. 2002, Theoretical Astrophysics - Volume 3, Galaxies and Cosmology, 638

Paglione, T. A. D., Marscher, A. P., Jackson, J. M., & Bertsch, D. L. 1996, ApJ, 460, 295

Park, B. T. & Petrosian, V. 1996, ApJS, 103, 255

Parker, E. N. 1957, J. Geophys. Res., 62, 509

Peng, F.-K., Zhang, H.-M., Wang, X.-Y., Wang, J.-F., & Zhi, Q.-J. 2019, ApJ, 884, 91

Peretti, E., Blasi, P., Aharonian, F., & Morlino, G. 2019, MNRAS, 487, 168

Peterson, B. M. 1998, Advances in Space Research, 21, 57

Peterson, B. M. & Wandel, A. 1999, ApJ, 521, L95

Petrosian, V. 2012, Space Sci. Rev., 173, 535

Petrosian, V. & Liu, S. 2004, ApJ, 610, 550

Pier, E. A., Antonucci, R., Hurt, T., Kriss, G., & Krolik, J. 1994, ApJ, 428, 124

Pierre Auger Collaboration, Aab, A., Abreu, P., et al. 2017, Science, 357, 1266

Press, W. H., Teukolsky, S. A., Vetterling, W. T., & Flannery, B. P. 1996, Numerical Recipes in Fortran 90 (2nd Ed.): The Art of Parallel Scientific Computing (USA: Cambridge University Press)

Protheroe, R. J. 1999, in Topics in Cosmic-Ray Astrophysics, ed. M. A. Duvernois, Vol. 230, 247

Pshirkov, M. S., Tinyakov, P. G., Kronberg, P. P., & Newton-McGee, K. J. 2011, The Astrophysical Journal, 738, 192

Puche, D. & Carignan, C. 1988, AJ, 95, 1025

Quinn, J. 2019, in European Physical Journal Web of Conferences, Vol. 209, European Physical Journal Web of Conferences, 01028

Radovich, M., Kahanpää, J., & Lemke, D. 2001, A&A, 377, 73

Ramos Almeida, C., Martínez González, M. J., Asensio Ramos, A., et al. 2016, MNRAS, 461, 1387

Rando, R., De Angelis, A., Mallamaci, M., & e-ASTROGAM collaboration. 2019, in Journal of Physics Conference Series, Vol. 1181, Journal of Physics Conference Series, 012044

Raymond, J. C., Cox, D. P., & Smith, B. W. 1976, ApJ, 204, 290

Rekola, R., Richer, M. G., McCall, M. L., et al. 2005, MNRAS, 361, 330

Rephaeli, Y., Arieli, Y., & Persic, M. 2010, MNRAS, 401, 473

Rieger, F. 2019, in High Energy Phenomena in Relativistic Outflows VII, 19

Romanowsky, A. J., Martínez-Delgado, D., Martin, N. F., et al. 2016, MNRAS, 457, L103

Romero, G. E., Müller, A. L., & Roth, M. 2018, A&A, 616, A57

Romero, G. E. & Paredes, J. M. 2011, Introducción a la Astrofísica Relativista (Publicacions i Edicions de la Universitat de Barcelona)

Romero, G. E., Vieyro, F. L., & Vila, G. S. 2010, A&A, 519, A109

Romero, G. E. & Vila, G. S. 2014a, Introduction to Black Hole Astrophysics, Vol. 876

Romero, G. E. & Vila, G. S., eds. 2014b, Lecture Notes in Physics, Berlin Springer Verlag, Vol. 876, Introduction to Black Hole Astrophysics

Ruderman, M. A. & Sutherland, P. G. 1975, ApJ, 196, 51

Rybicki, G. B. & Lightman, A. P. 1979, Radiative processes in astrophysics (Wiley-Interscience)

Sandage, A., Véron, P., & Wyndham, J. D. 1965, ApJ, 142, 1307

Santillan, A., Franco, J., & Kim, J. 2004, Journal of Korean Astronomical Society, 37, 233

Schlickeiser, R. 2002, Cosmic Ray Astrophysics

Schmidt, M. 1959, ApJ, 129, 243

Searle, L., Sargent, W. L. W., & Bagnuolo, W. G. 1973, ApJ, 179, 427

Semikoz, D., Tinyakov, P., & Zotov, M. 2016, Phys. Rev. D, 93, 103005

Shadmehri, M. 2015, MNRAS, 451, 3671 –3678

Shakura, N. I. & Sunyaev, R. A. 1973, A&A, 24, 337

Sharma, M., Theuns, T., Frenk, C., et al. 2016, MNRAS, 458, L94

Shin, M.-S., Stone, J. M., & Snyder, G. F. 2008, ApJ, 680, 336

Shu, F. H. & Hughes, P. A. 1992, Nature, 357, 122

Sillanpaa, A., Haarala, S., Valtonen, M. J., Sundelius, B., & Byrd, G. G. 1988, ApJ, 325, 628

Simkovic, F. 2019, in International Cosmic Ray Conference, Vol. 36, 36th International Cosmic Ray Conference (ICRC2019), 1011

Soldi, S., Beckmann, V., Baumgartner, W. H., et al. 2014, A&A, 563, A57

Somov, B. V. 2012, Plasma Astrophysics, Part I, Vol. 391

Sparre, M., Pfrommer, C., & Vogelsberger, M. 2019, MNRAS, 482, 5401

Stawarz, Ł. & Petrosian, V. 2008, ApJ, 681, 1725

Stecker, F. W. & Salamon, M. H. 1999, ApJ, 512, 521

Stein, R., van Velzen, S., Kowalski, M., et al. 2020, arXiv e-prints, arXiv:2005.05340

Strickland, D. K. & Heckman, T. M. 2009, ApJ, 697, 2030

Strickland, D. K., Heckman, T. M., Weaver, K. A., & Dahlem, M. 2000, AJ, 120, 2965

Strickland, D. K., Heckman, T. M., Weaver, K. A., Hoopes, C. G., & Dahlem, M. 2002, ApJ, 568, 689

Su, M., Slatyer, T. R., & Finkbeiner, D. P. 2010, ApJ, 724, 1044

Suchkov, A. A., Balsara, D. S., Heckman, T. M., & Leitherer, C. 1994, ApJ, 430, 511

Sweet, P. A. 1958, Il Nuovo Cimento, 8, 188

Syer, D., Clarke, C. J., & Rees, M. J. 1991, MNRAS, 250, 505

Tanner, R., Cecil, G., & Heitsch, F. 2017, ApJ, 843, 137

Tenorio-Tagle, G. 1980, A&A, 94, 338–344

Tenorio-Tagle, G. 1981, A&A, 94, 338

Terlevich, R. 1997, in Revista Mexicana de Astronomia y Astrofisica Conference Series, Vol. 6, Revista Mexicana de Astronomia y Astrofisica Conference Series, ed. J. Franco, R. Terlevich, & A. Serrano, 1

The Pierre Auger Collaboration. 2015, arXiv e-prints, arXiv:1502.01323

The Pierre Auger Collaboration, Aab, A., Abreu, P., et al. 2019, arXiv e-prints, arXiv:1909.09073

The Pierre Auger Collaboration, Aab, A., Abreu, P., et al. 2017, arXiv e-prints, arXiv:1708.06592

Theureau, G., Hanski, M. O., Coudreau, N., Hallet, N., & Martin, J. M. 2007, A&A, 465, 71

Treves, A., Maraschi, L., & Abramowicz, M. 1988, PASP, 100, 427

Tully, R. B. 1988, Nearby galaxies catalog

Turner, J. L. & Ho, P. T. P. 1985, ApJ, 299, L77

Unger, M. & Farrar, G. R. 2017

Urry, C. M. & Padovani, P. 1995, PASP, 107, 803

Vacca, W. D., Hamilton, R. T., Savage, M., et al. 2015, ApJ, 804, 66

Valtonen, M. J., Lehto, H. J., Nilsson, K., et al. 2008, Nature, 452, 851

van Dyke, M. D. & Gordon, H. D. 1959, Supersonic Flow past a Family of Blunt Axisymmetric Bodies, Technical report, NASA Ames Research Center

van Putten, M. H. P. M., Levinson, A., Frontera, F., et al. 2019, European Physical Journal Plus, 134, 537

Veilleux, S., Cecil, G., & Bland-Hawthorn, J. 2005, ARA&A, 43, 769

Venters, T. M. 2010, ApJ, 710, 1530

Vieyro, F. L. & Romero, G. E. 2012, A&A, 542, A7

Vila, G. S. & Aharonian, F. 2009, Compact Objects and their Emission, ed. G. E. Romero & P. Benaglia (Paideia)

Vink, J. & Laming, J. M. 2003, ApJ, 584, 758

Vink, J. & Yamazaki, R. 2014, ApJ, 780, 125

Wang, X. & Fields, B. D. 2018, MNRAS, 474, 4073

Waxman, E. & Bahcall, J. 1999, Phys. Rev. D, 59, 023002

Weaver, K. A., Heckman, T. M., Strickland, D. K., & Dahlem, M. 2002, ApJ, 576, L19

Weisberg, J. M. & Taylor, J. H. 2005, in Astronomical Society of the Pacific Conference Series, Vol. 328, Binary Radio Pulsars, ed. F. A. Rasio & I. H. Stairs, 25

Wik, D. R., Lehmer, B. D., Hornschemeier, A. E., et al. 2014, ApJ, 797, 79

Wojaczyński, R. & Niedźwiecki, A. 2017, ApJ, 849, 97

Wojaczyński, R., Niedźwiecki, A., Xie, F.-G., & Szanecki, M. 2015, A&A, 584, A20

Wolfire, M. G., McKee, C. F., Hollenbach, D., & Tielens, A. G. G. M. 2003, ApJ, 587, 278

Xie, Z. H., Ma, L., Zhang, X., et al. 2009, ApJ, 707, 866

Xu, J. & Stone, J. M. 1995, ApJ, 454, 172

Yoast-Hull, T. M., Gallagher, J. S., I., Zweibel, E. G., & Everett, J. E. 2014, ApJ, 780, 137

Yoast-Hull, T. M., Gallagher, John S., I., Aalto, S., & Varenius, E. 2017, MNRAS, 469, L89

Zaino, A., Bianchi, S., Marinucci, A., et al. 2020, MNRAS, 104

Zatsepin, G. T. & Kuz'min, V. A. 1966, Soviet Journal of Experimental and Theoretical Physics Letters, 4, 78

Zentsova, A. S. 1983, Ap&SS, 95, 11

Zhang, B. T. & Murase, K. 2019, Phys. Rev. D, 100, 103004

Zhang, B. T., Murase, K., Kimura, S. S., Horiuchi, S., & Mészáros, P. 2018, Phys. Rev. D, 97, 083010

Zhang, D. 2018, Galaxies, 6, 114

Znajek, R. L. 1978, MNRAS, 185, 833

Zurek, W. H., Siemiginowska, A., & Colgate, S. A. 1994, ApJ, 434, 46

Erklärung

La Plata, den 28.10.2020

Erklärung der selbständigen Anfertigung meiner Dissertationsschrift

Hiermit versichere ich, dass ich die Dissertationsschrift mit dem Titel

Acceleration and propagation of cosmic rays
in high-metallicity astrophysical environments

selbständig und ohne unerlaubte fremde Hilfe verfasst habe. Dabei habe ich keine anderen, als die von mir angegebenen Hilfsmittel benutzt.

_____

Ana Laura Müller